

ENCLOSURE 6

**TENNESSEE VALLEY AUTHORITY
BROWNS FERRY NUCLEAR PLANT (BFN)
UNITS 1, 2, AND 3**

**TECHNICAL SPECIFICATIONS (TS) CHANGES TS-431 AND TS-418
EXTENDED POWER UPRATE (EPU)**

CALCULATION PACKAGE 0006982.01

(NON-PROPRIETARY VERSION)

Attached is Calculation Package 0006982.01, "Shell and Solid Sub-Model Finite Element Stress Comparison."



Structural Integrity Associates, Inc.

File No.: 0006982.301

CALCULATION PACKAGE

Project No.: 0006982.00

PROJECT NAME:

Extended Power Uprate Main Steam Line Strain Gage Vibration Monitoring

CONTRACT NO.:

CWA P4463

CLIENT:

Tennessee Valley Authority (TVA)

PLANT: Browns Ferry Units 1, 2 & 3

CALCULATION TITLE:

Shell and Solid Sub-Model Finite Element Stress Comparison

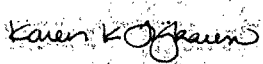
Document Revision	Affected Pages	Revision Description	Project Manager Approval Signature & Date	Preparer(s) & Checker(s) Signatures & Date
0	1-31, A1, Computer Files	Initial Issue	M. L. Herrera for K. K. Fujikawa 06/04/08	S. B. Kok 06/04/08 R. Gnagne 06/04/08 S. S. Tang 06/04/08
1	All	Incorporate client comment.	 K. K. Fujikawa 06/16/08	 S. B. Kok 06/16/08  S. S. Tang 06/16/08

Table of Contents

1.0 INTRODUCTION 4

2.0 METHODOLOGY AND ASSUMPTIONS..... 5

3.0 MATERIAL PROPERTIES 6

4.0 STIFFENER ANALYSIS..... 7

 4.1 Key Dimensions..... 7

 4.2 Boundary Conditions and Applied Load 8

 4.3 Shell Finite Element Model 9

 4.4 Solid Finite Element Model..... 10

 4.5 Solid Model Stress Paths 12

 4.6 Shell Model Results..... 13

 4.7 Solid Model Results..... 14

 4.8 Stress Comparison 16

5.0 DRAIN CHANNEL ANALYSIS..... 17

 5.1 Key Dimensions..... 17

 5.2 Boundary Conditions and Applied Load 18

 5.3 Shell Finite Element Model..... 20

 5.4 Solid Finite Element Model..... 21

 5.5 Solid Model Stress Paths 23

 5.6 Shell Model Results..... 25

 5.7 Solid Model Results..... 26

 5.8 Stress Comparison 29

6.0 CONCLUSIONS 30

7.0 REFERENCES 31

Appendix A - Computer Files..... A1

List of Tables

Table 4-1 Stiffener Model Key Dimensions.....	7
Table 4-2 Stiffener Solid Model Maximum Stress Intensity.....	15
Table 4-3 Stiffener Solid Model / Shell Model Stress Ratio.....	16
Table 5-1 Drain Channel Model Key Dimensions.....	17
Table 5-2 Stress Profile Comparison.....	19
Table 5-3 Drain Channel Solid Model Maximum Stress Intensity.....	28
Table 5-4 Drain Channel Solid Model / Shell Model Stress Ratio.....	29

List of Figures

Figure 4-1 Stiffener Model Boundary Conditions and Applied Load.....	8
Figure 4-2 Stiffener Shell Finite Element Model Mesh.....	9
Figure 4-3 Stiffener Solid Finite Element Model Mesh (Isometric View).....	10
Figure 4-4 Stiffener Solid Finite Element Model Mesh (Bottom View).....	11
Figure 4-5 Stiffener Solid Model Stress Paths.....	12
Figure 4-6 Stiffener Shell Model Stress Intensity at High Stress Location.....	13
Figure 4-7 Stiffener Solid Model Stress Intensity at High Stress Region.....	14
Figure 5-1 Drain Channel Model Boundary Conditions and Applied Load.....	18
Figure 5-2 Drain Channel Shell Finite Element Model Mesh.....	20
Figure 5-3 Drain Channel Solid Finite Element Model Mesh (Inside Weld Region).....	21
Figure 5-4 Drain Channel Solid Finite Element Model Mesh (Outside Weld Region).....	22
Figure 5-5 Drain Channel Solid Finite Element Stress Paths (End View).....	23
Figure 5-6 Drain Channel Solid Finite Element Stress Paths (Side View).....	24
Figure 5-7 Drain Channel Shell Finite Element $P_m + P_b$ Stress Intensity at the Bottom of the Drain Channel.....	25
Figure 5-8 Drain Channel Solid Finite Element Stress Intensity at the Bottom of the Drain Channel (Inside Weld Region).....	26
Figure 5-9 Drain Channel Solid Finite Element Stress Intensity at the Bottom of the Drain Channel (Outside Weld Region).....	27



1.0 INTRODUCTION

Background

The Browns Ferry steam dryer has been analyzed using a shell finite element model, which does not specifically model the weld. The results show that there are localized high stresses at some of the welded connections. Based on past experience, it has been established that if the connections are modeled using solid elements to represent the weld, the weld can better distribute the stresses in the region of high stress concentration. Coupled with the use of stress linearization approach, the maximum stress intensity computed using the solid model (with the weld modeled) generally gives a better prediction of stresses compared with shell elements in region of high stress concentration.

Objective

This calculation documents the comparison of the stress intensity computed using a shell finite element model and a solid finite element model with linearization stress paths in the region of interest. In the shell finite element model, the details of the connecting welds are not modeled, while the welds are modeled in detail in the solid finite element model. In order to make a direct comparison between the shell and the solid finite element models, these models must have the same dimensions, same material properties, and subject to the same boundary conditions and loading.

Two steam dryer components are being analyzed in this calculation:

1. The stiffener plate, which is welded between the van bank hood.
2. The drain channel, which is welded to the skirt.

Stress profiles from the full model analysis (Reference 3) are provided for each of the two components. Appropriate loading conditions that closely match the original stress profiles will be used. This ensures that the loading that causes the localized high stress is captured.

The finite element analyses in this calculation are performed using ANSYS Version 11.0 (Reference 5).

Revision 1

Remove all statements that indicate the information contained in this calculation is of vendor proprietary nature.



2.0 METHODOLOGY AND ASSUMPTIONS

Stiffener

The full model analysis shows that the maximum stress is essentially membrane stress (P_m) with little bending stresses (P_b). When the linearized stresses are obtained for the different locations in the solid model, both the membrane stress (P_m) and the membrane plus bending stress ($P_m + P_b$) are computed.

The evaluation only compares the membrane plus bending stress ($P_m + P_b$) of the solid model with the membrane plus bending stress ($P_m + P_b$) of the shell model. The computed stress ratio will be used to adjust the stresses in the full model.

The stress profile for the full model shows that the highest stress is localized at the bottom most node. Beyond that, the nodal stresses fall below 500 psi, a threshold used in the stress profile. A unit load of 1,000 lb is applied to the bottom 1.75" section of the stiffener.

Drain Channel

The full model analysis shows that the governing stress is the membrane plus bending stress ($P_m + P_b$). The membrane stress (P_m) is small, and does not govern. When the linearized stresses are obtained for the different locations in the solid model, only the membrane plus bending stress ($P_m + P_b$) are compared with the corresponding maximum membrane plus bending stress ($P_m + P_b$) from the shell model. The computed stress ratio will be used to adjust the stresses in the full model.

In order to capture the loading condition that is reflective of the full model analysis, an iterative approach was used to establish the desirable loading for the sub-model. The stress profile from the sub-model along the drain channel / skirt interface is compared with the stress profile for the full model. Since the highest stress is located at the bottom of the channel, stresses further away from the bottom are less significant. Therefore, the comparison of the stresses from the profile is confined to the four-inch section at the bottom of the drain channel.

Key Assumptions

1. A sub-model is used for comparing the maximum stress intensity between the shell and the solid models. In the model, appropriate boundary conditions are assumed.
2. The material properties for A-240, Type 304 stainless steel (Reference 2) at 550°F are used for the analysis. Similar material properties are assumed for the weld.

3.0 MATERIAL PROPERTIES

The material properties used are as follows:

Modulus of Elasticity = 25.55E6 psi (Reference 4, Page 12)
Poisson's Ratio = 0.30 (Reference 4, Page 12)

4.0 STIFFENER ANALYSIS

The stiffener sub-model consists of three key parts: the stiffener, the hood, and the base plate. For the solid sub-model, the weld is also included.

4.1 Key Dimensions

The key dimensions of the sub-model are as follows:

**Table 4-1
Stiffener Model Key Dimensions**

Component	Thickness / Size (in)	Modeled Dimensions (in x in)
Stiffener	1/4"	10" (width) x 34" (height)
Hood	1/2"	56" (depth) x 34" (height)
Base Plate	1/2"	56" (depth) x 7" (width)
Weld ⁽¹⁾	3/16"	Along the entire connection:

Notes: (1) The fillet weld is modeled in the solid sub-model, on both sides.

(2) The dimensions are taken from the drawings (Reference 1).

4.2 Boundary Conditions and Applied Load

The boundary conditions and applied load are identified in the following Figure 4-1.

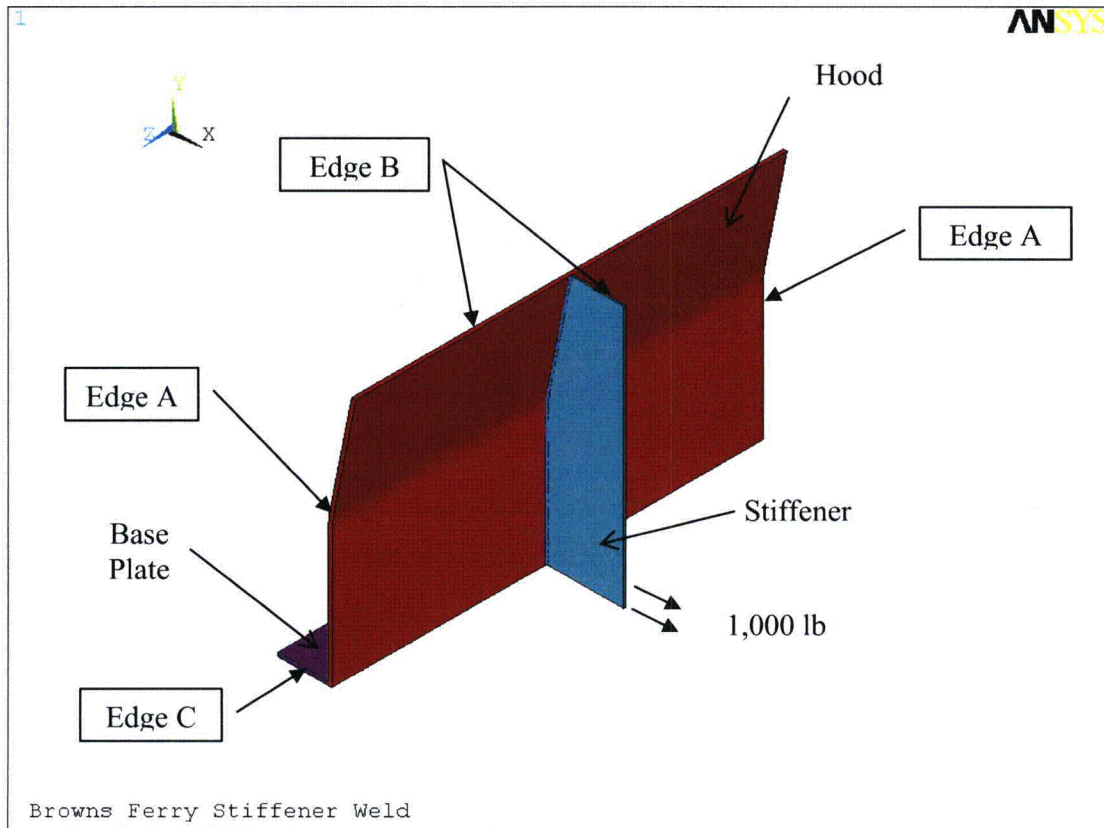


Figure 4-1
Stiffener Model Boundary Conditions and Applied Load

Boundary Conditions

Edge A: Plane of symmetry.

Edge B: Restrained in Y translation, and rotation about X and Z.

Edge C: Plane of symmetry, and restrained from translation in X.

Applied Load

Load: 1,000 lb is evenly applied at the bottom 1.75" section of the stiffener.

4.3 Shell Finite Element Model

The shell finite element model is modeled using SHELL63 elements. A regular mesh size of 0.25" is used for the entire model. The entire model consists of approximately 42,000 nodes and 42,000 shell elements. The finite element mesh is shown in the following Figure 4-2.

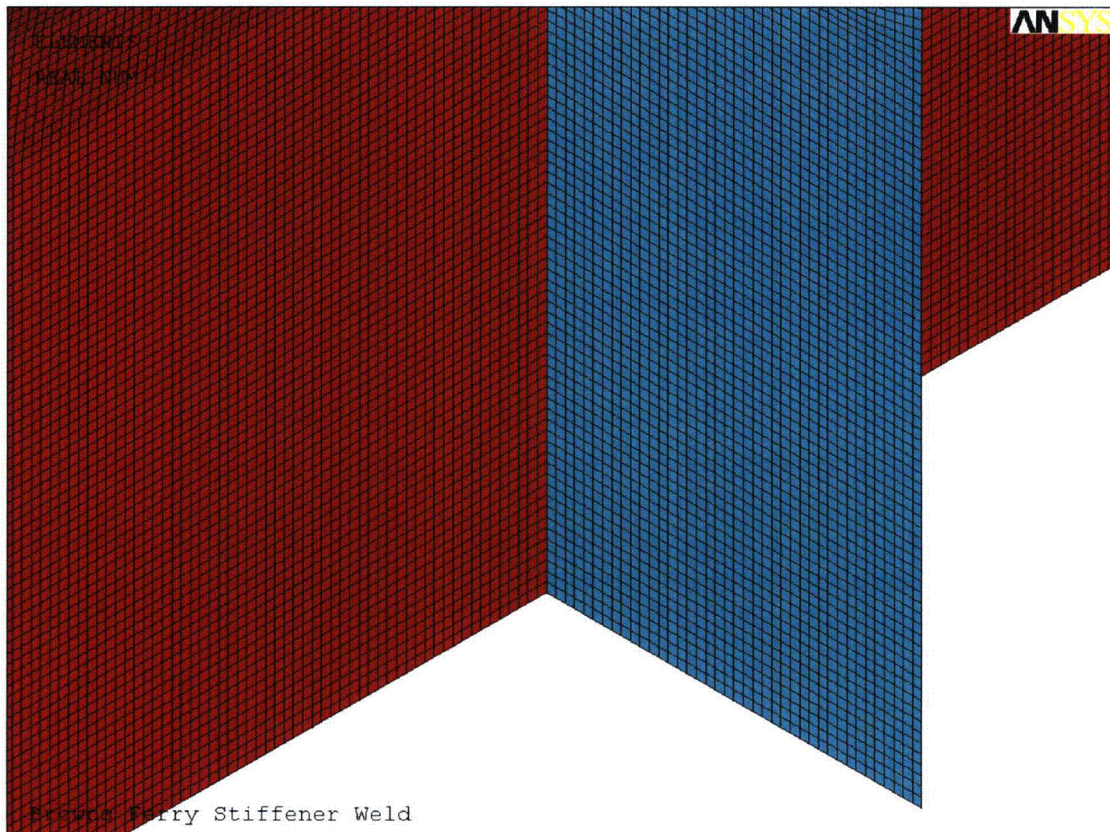


Figure 4-2
Stiffener Shell Finite Element Model Mesh

4.4 Solid Finite Element Model

The solid finite element model is modeled using SOLID45 elements. Variable mesh sizes, with finer mesh around the region of high stress concentration and coarser mesh away from the high stress concentration region, are used. Six layers of element are modeled across the plate thickness, therefore, providing adequate discretization through the plate thickness to capture the stress variations across the thickness. The entire model consists of approximately 323,000 nodes and 276,000 solid elements. The finite element mesh is shown in the following Figure 4-3 and Figure 4-4.

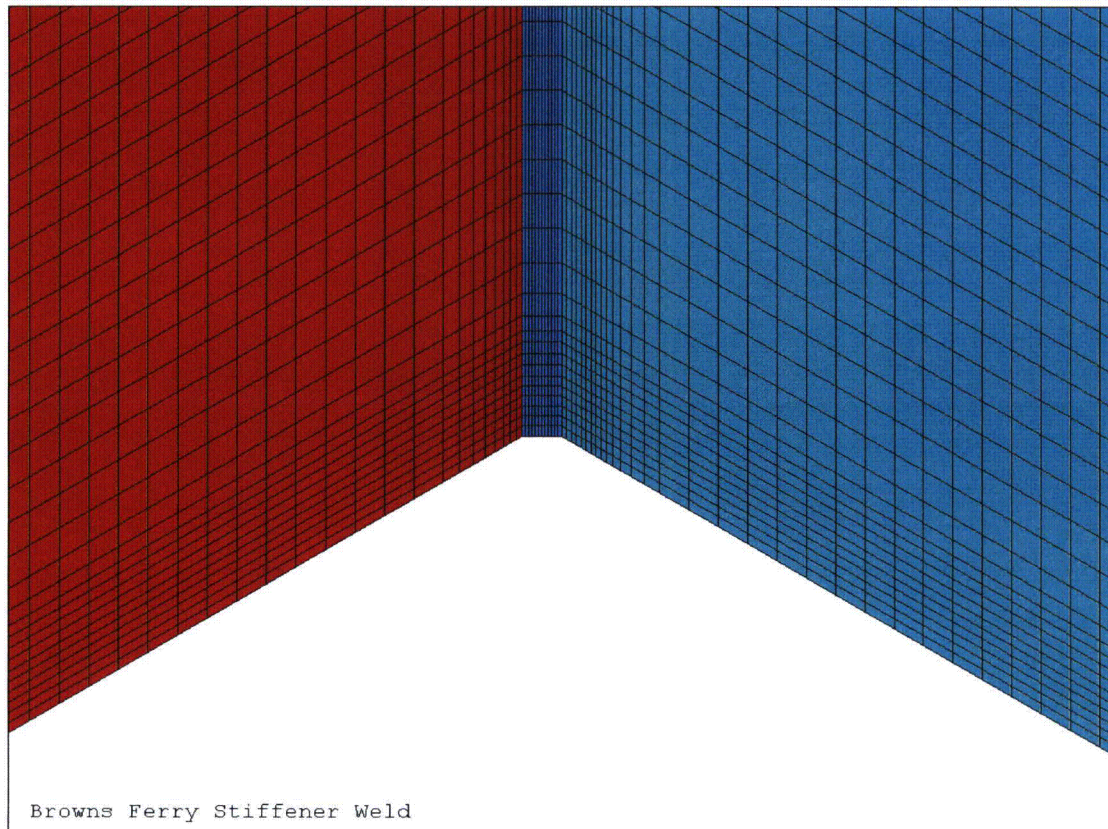


Figure 4-3
Stiffener Solid Finite Element Model Mesh
(Isometric View)

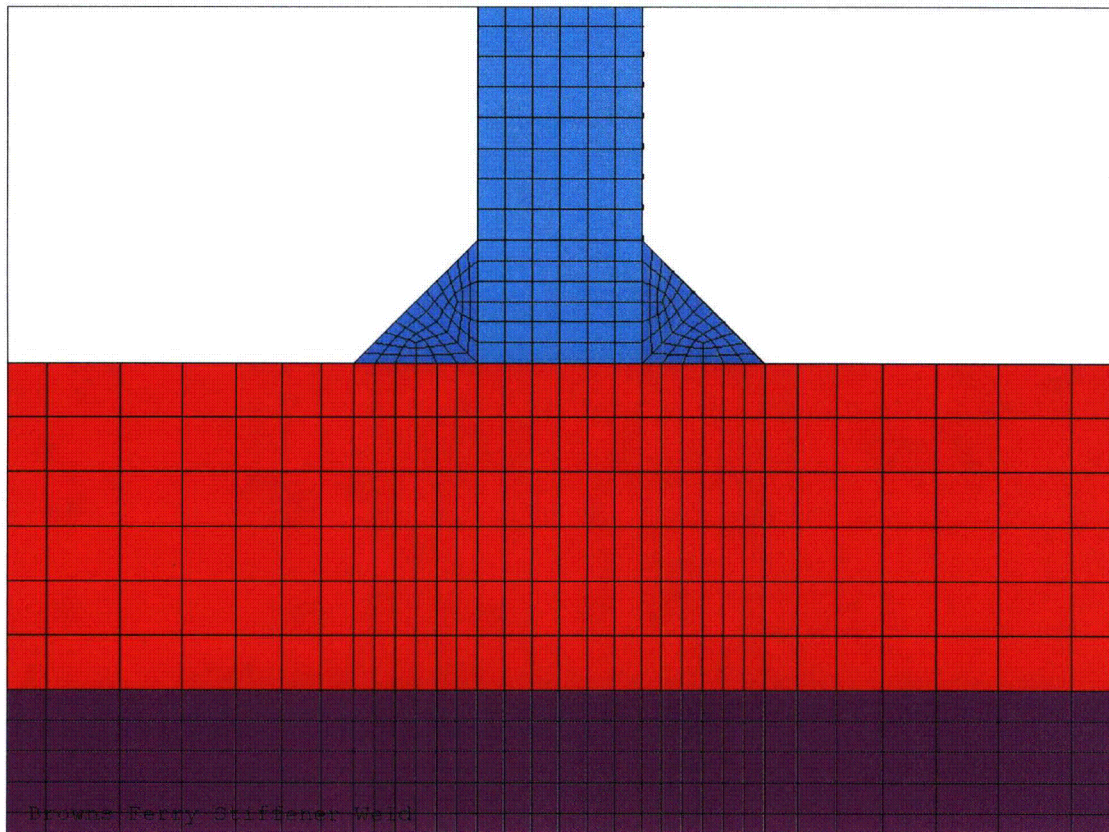


Figure 4-4
Stiffener Solid Finite Element Model Mesh
(Bottom View)

4.5 Solid Model Stress Paths

Linearization stress paths are taken from the weld root to the component surface in the vicinity of the high stress region. In addition, linearization stress paths are also taken from the weld toe to the opposite surface of the connected parts. The stress paths used for the stiffener solid model are shown in the following Figure 4-5.

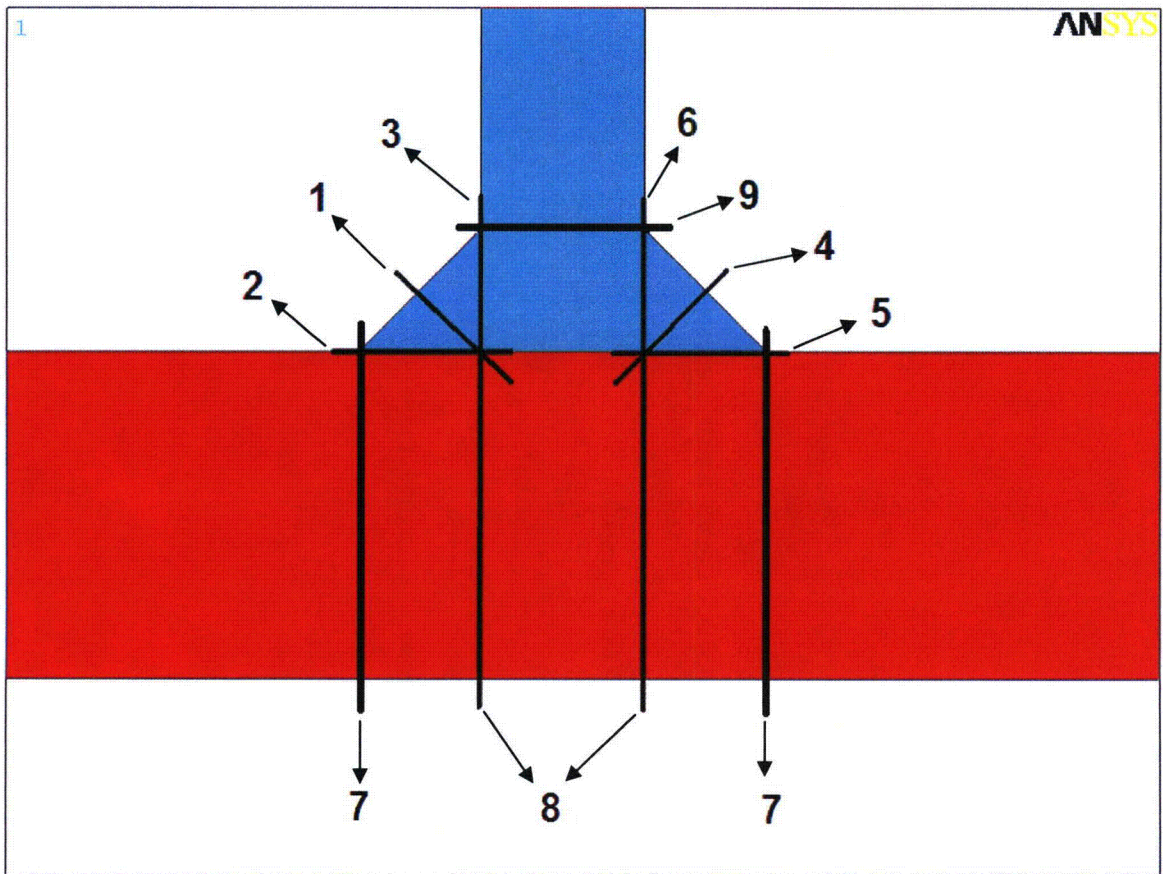


Figure 4-5
Stiffener Solid Model Stress Paths

4.6 Shell Model Results

The stress intensity plots for the shell model are provided in the following Figure 4-6.

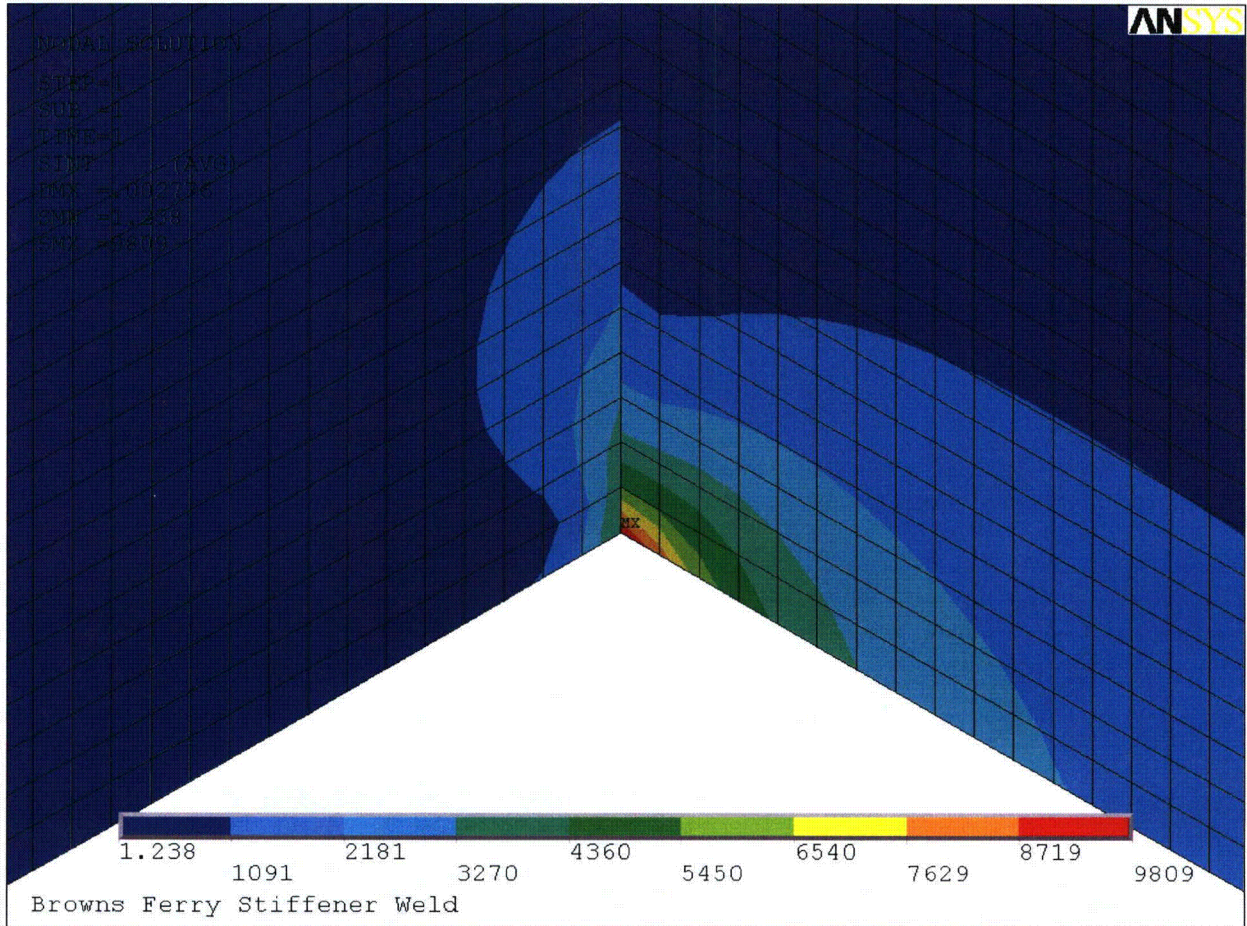


Figure 4-6
Stiffener Shell Model Stress Intensity
at High Stress Location

Summary

The maximum stress intensity is 9,809 psi, which is the same for both the membrane stress (P_m) and membrane plus bending stress ($P_m + P_b$) in this case.

4.7 Solid Model Results

The stress intensity plots for the solid model are provided in the following Figure 4-7.

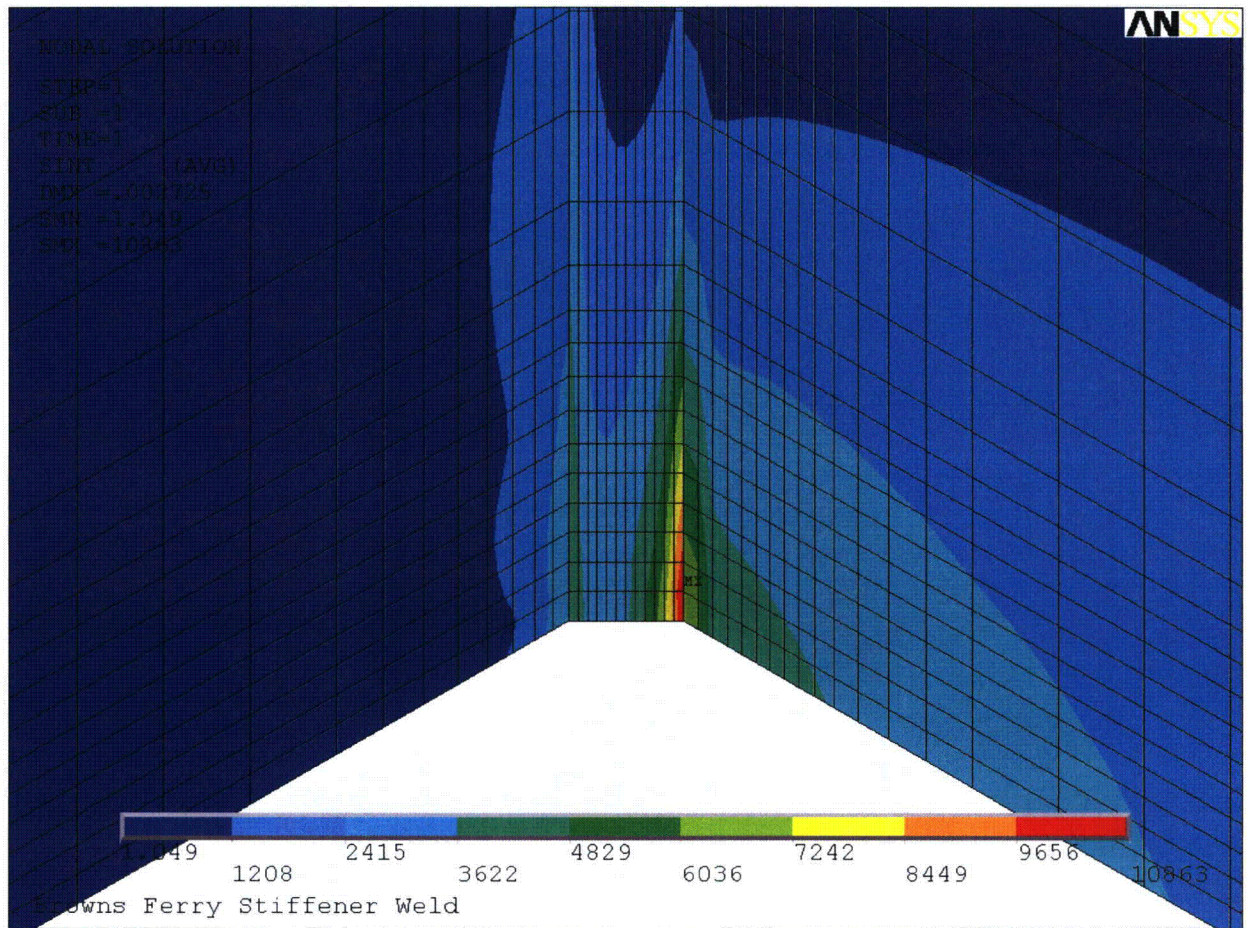


Figure 4-7
Stiffener Solid Model Stress Intensity
at High Stress Region

Maximum Stress Intensity

The stress intensity is computed for the different stress paths. There are multiple locations for each of the paths, and the largest magnitude is identified as the maximum stress intensity for that path. The maximum stress intensity for the different paths are summarized in the following Table 4-2.

**Table 4-2
Stiffener Solid Model Maximum Stress Intensity**

Path #	$P_m + P_b$ (psi)
1	6,377
2	5,383
3	7,784
4	6,377
5	5,383
6	7,784
7	2,185
8	2,260
9	5,536

4.8 Stress Comparison

The stress comparison between the shell and the solid finite element models is summarized in the following Table 4-3.

**Table 4-3
Stiffener Solid Model / Shell Model Stress Ratio**

Path #	$P_m + P_b$		
	Solid (psi)	Shell (psi)	Ratio
1	6,377	9,809	0.65
2	5,383		0.55
3	7,784		0.79
4	6,377		0.65
5	5,383		0.55
6	7,784		0.79
7	2,185		0.22
8	2,260		0.23
9	5,536		0.56
		Maximum =	0.79

Summary

The maximum stress ratio for the solid model stress intensity / shell model stress intensity is 0.79.



5.0 DRAIN CHANNEL ANALYSIS

The drain channel sub-model consists of three key parts: the drain channel, the skirt, and the lower support ring. For the solid sub-model, the weld is also included.

5.1 Key Dimensions

The key dimensions of the sub-model are as follows:

**Table 5-1
Drain Channel Model Key Dimensions**

Component	Thickness / Size (in)	Modeled Dimensions
Drain Channel ⁽¹⁾	1/8"	27" (height), 122.5" (mid radius), and spanning a 22.2° arc
Skirt	1/4"	30" (height), 119" (mid radius), and spanning a 27.7° arc
Lower Support Ring	1"	4" (height), 119-3/8" (mid radius), and spanning a 27.7° arc
Outside Weld ⁽²⁾	1/4"	Along the entire modeled drain channel / skirt connection.
Inside Weld ⁽²⁾	1/4"	1" long
End Weld ⁽²⁾	1/4"	Rounded transition from the outside and the inside to the bottom of the drain channel.

- Notes:
- (1) The drain channel is rounded with 3.5" radius as it connects with the skirt.
 - (2) The fillet welds are modeled in the solid sub-model only.
 - (3) The dimensions are taken from the drawings (Reference 1).

5.2 Boundary Conditions and Applied Load

The boundary conditions and applied load are identified in the following Figure 5-1.

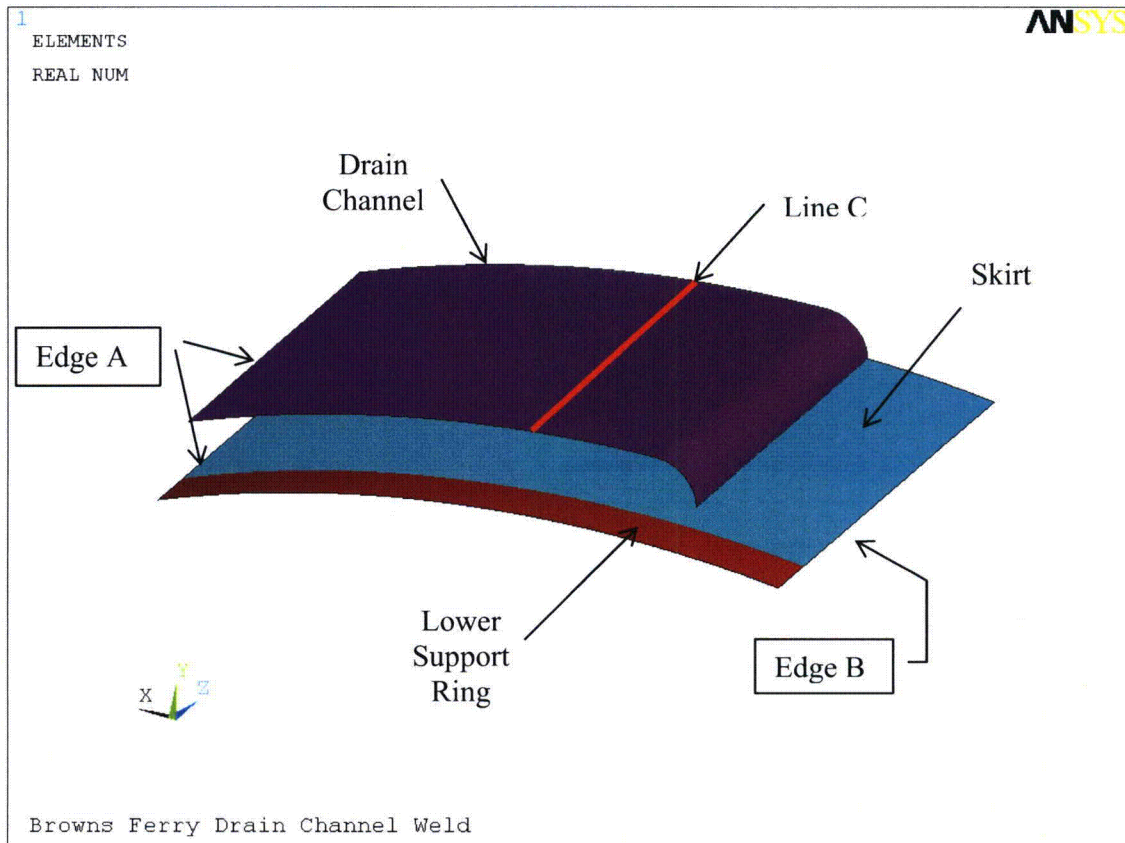


Figure 5-1
Drain Channel Model Boundary Conditions and Applied Load

Boundary Conditions

Edge A: Plane of symmetry.

Edge B: Plane of symmetry.

Applied Load

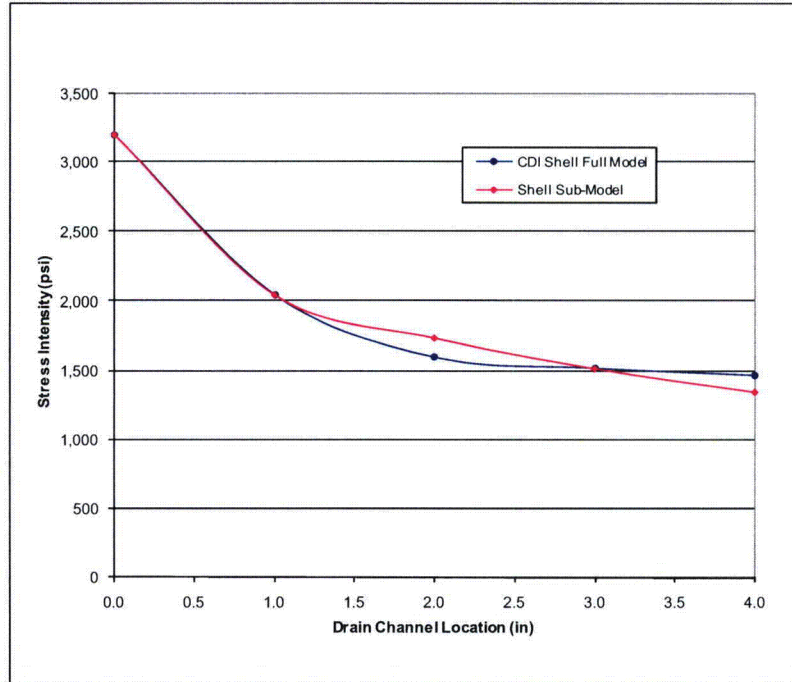
Line C: Imposed displacements along the line at 1" regular interval.

The following iterative approach is used to establish the desirable displacements:

1. Impose a set of prescribed displacements, at 1" regular interval, along a vertical line in the drain channel.
2. Compute the stress intensity along the drain channel / skirt interface.
3. Compare the sub-model stress profile and the full model shell stress profile for the first 5 points (i.e., up to 4 inches away from the drain channel bottom location).
4. Repeat steps 1 to 3, by changing the position of the vertical line or prescribed displacements, until a satisfactory match is obtained between the sub-model stress profile and the full model stress profile.
5. Apply the same set of imposed displacements on both the shell and the solid models.

The comparison of the stress profiles between the sub-model and the full model is provided in the following Table 5-2.

Table 5-2
Stress Profile Comparison



5.3 Shell Finite Element Model

The shell finite element model is modeled using SHELL63 elements. A regular mesh size of 0.25" is used for the entire model. The entire model consists of approximately 53,000 nodes and 53,000 shell elements. The finite element mesh is shown in the following Figure 5-2.

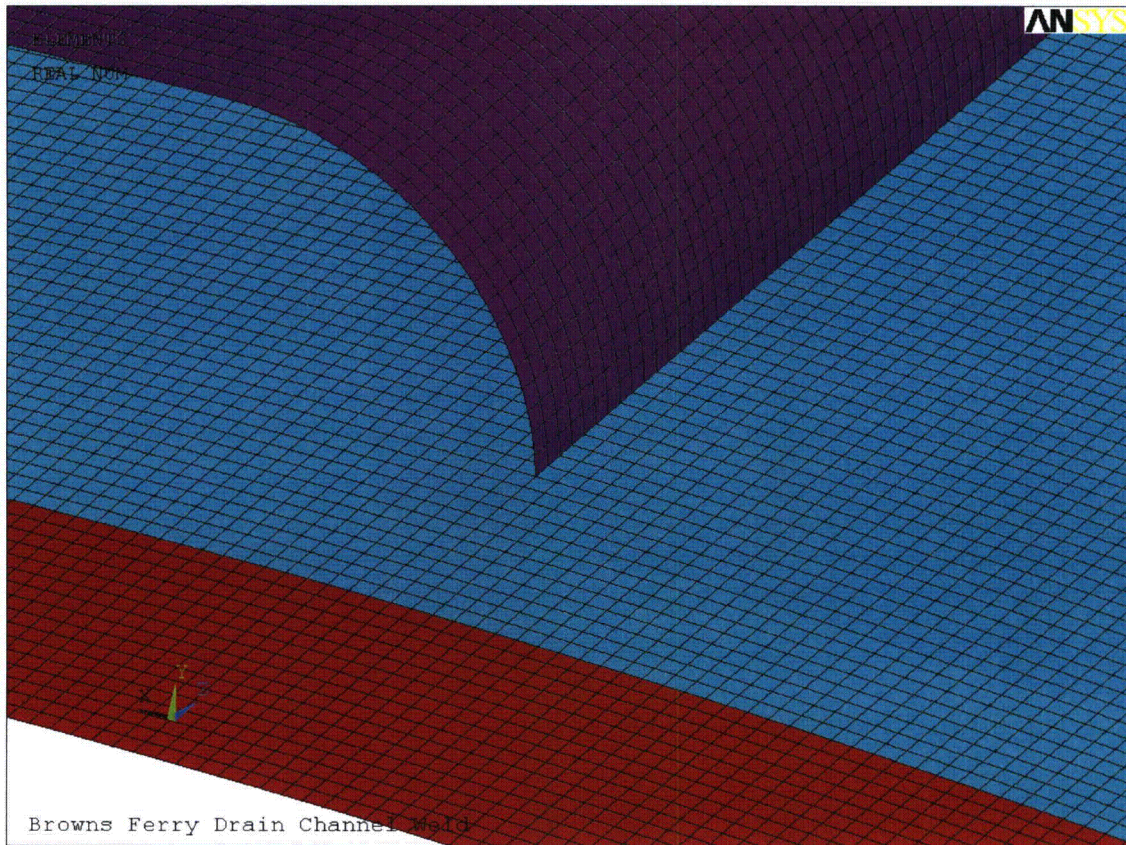


Figure 5-2
Drain Channel Shell Finite Element Model Mesh

5.4 Solid Finite Element Model

The solid finite element model is modeled using SOLID45 elements. Variable mesh sizes; with finer mesh around the region of high stress concentration and coarser mesh away from the high stress concentration region, are used. Six layers of element are modeled across the plate thickness, therefore, providing adequate discretization through the plate thickness to capture the plate bending behavior. The entire model consists of approximately 511,000 nodes and 442,000 solid elements. The finite element mesh is shown in the following Figure 5-3 and Figure 5-4.



Figure 5-3
Drain Channel Solid Finite Element Model Mesh
(Inside Weld Region)

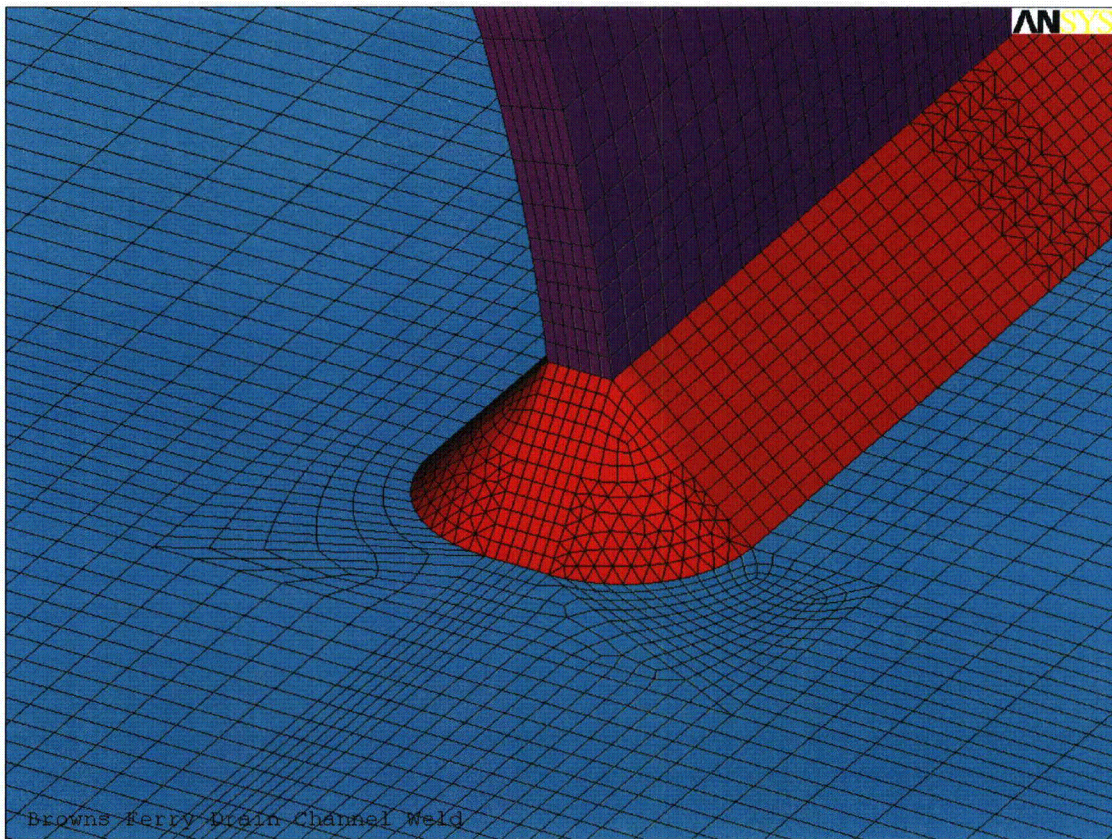


Figure 5-4
Drain Channel Solid Finite Element Model Mesh
(Outside Weld Region)

5.5 Solid Model Stress Paths

Linearization stress paths are taken from the weld root to the component surface in the vicinity of the high stress region. In addition, linearization stress paths are also taken from the weld toe to the opposite surface of the connected parts. The stress paths used for the stiffener solid model are shown in the following Figure 5-5 and Figure 5-6.

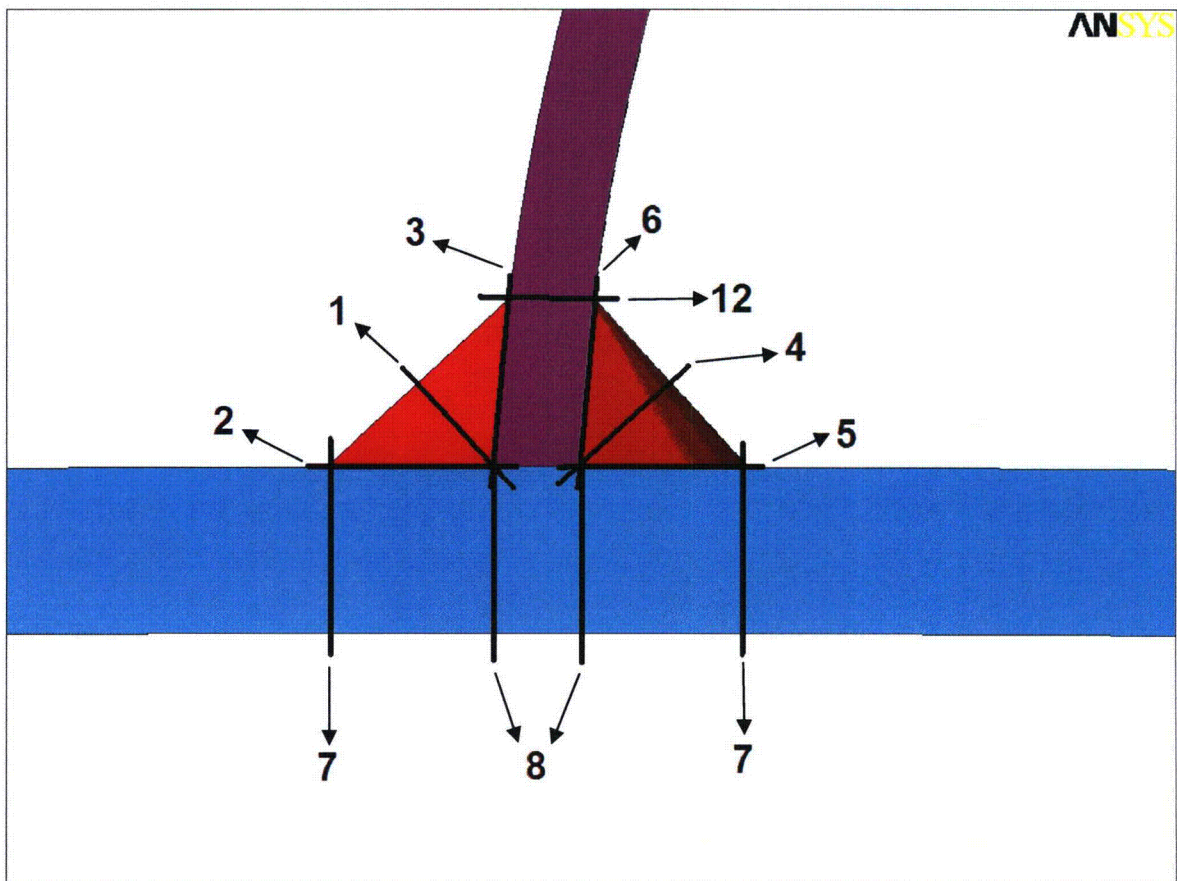


Figure 5-5
Drain Channel Solid Finite Element Stress Paths
(End View)

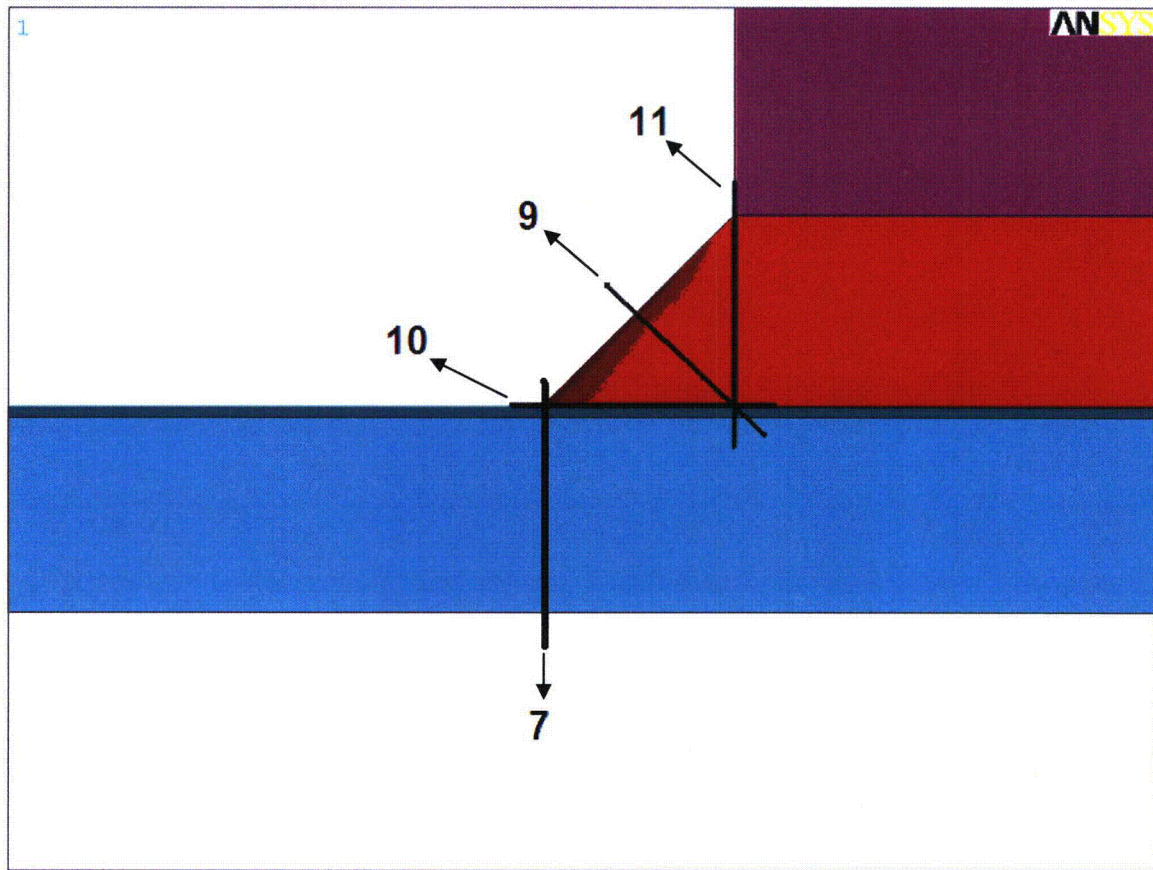
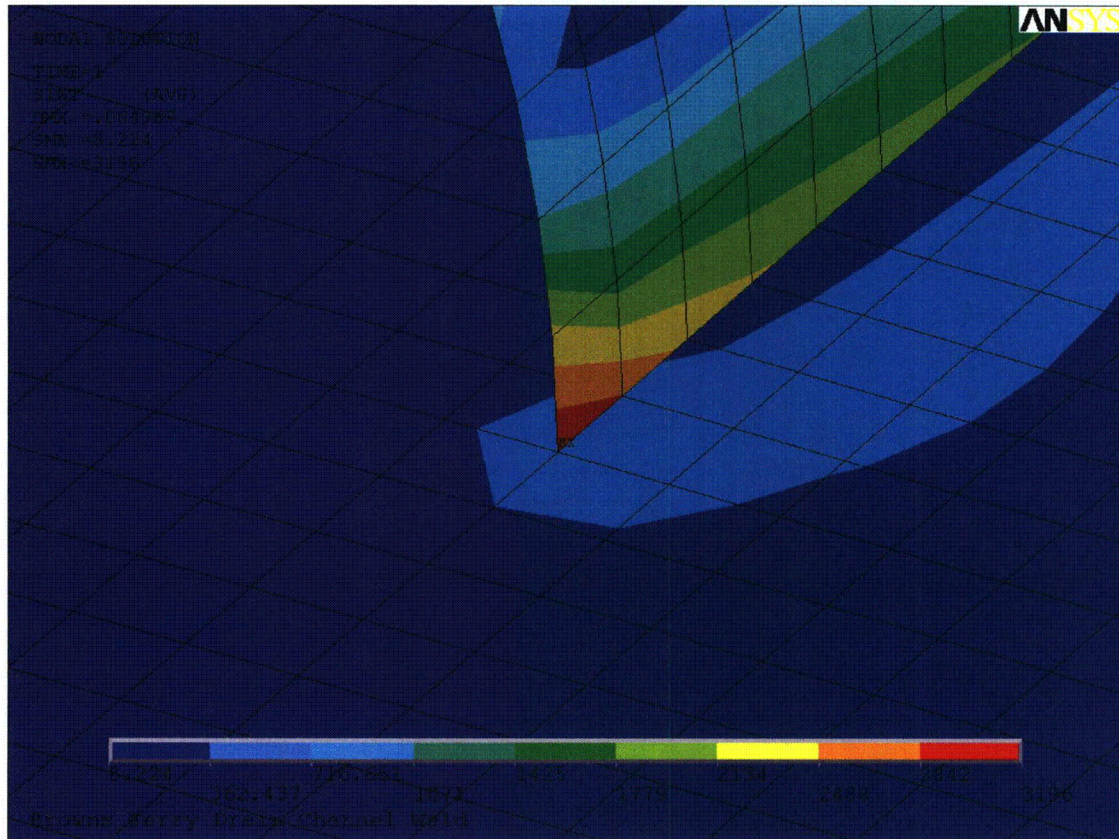


Figure 5-6
Drain Channel Solid Finite Element Stress Paths
(Side View)

5.6 Shell Model Results

The stress intensity plots for the shell model at the bottom of the drain channel, which is the location of interest, is provided in the following Figure 5-7.



5.7 Solid Model Results

The stress intensity plots for the solid model are provided in the following Figure 5-8.

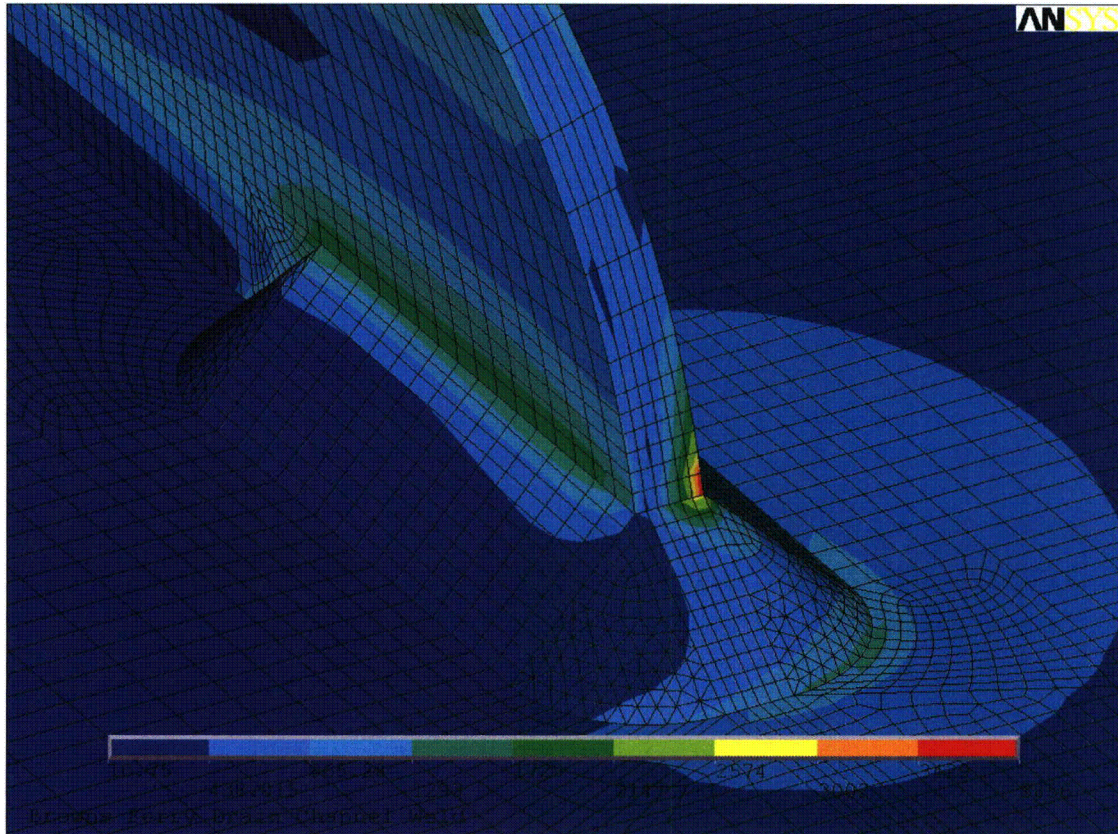


Figure 5-8
Drain Channel Solid Finite Element Stress Intensity
at the Bottom of the Drain Channel
(Inside Weld Region)

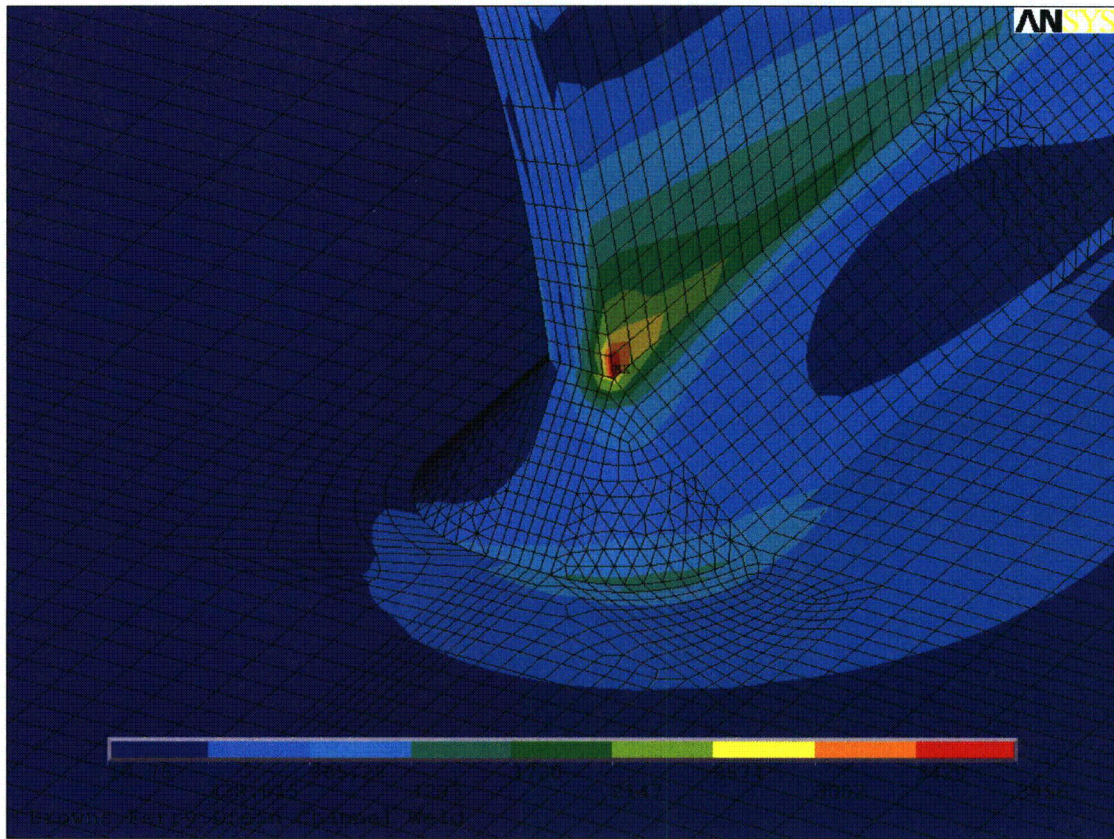


Figure 5-9
Drain Channel Solid Finite Element Stress Intensity
at the Bottom of the Drain Channel
(Outside Weld Region)

Maximum Stress Intensity

The stress intensity is computed for the different stress paths. There are multiple locations for each of the paths, and the largest magnitude is identified as the maximum stress intensity for that path. The maximum stress intensity for the different paths are summarized in the following Table 5-3.

**Table 5-3
Drain Channel Solid Model Maximum Stress Intensity**

Path #	$P_m + P_b$ (psi)
1	765
2	837
3	1,859
4	339
5	227
6	1,029
7	812
8	549
9	791
10	1,022
11	1,859
12	2,586

5.8 Stress Comparison

The stress comparison between the shell and the solid finite element models is summarized in the following Table 5-4.

**Table 5-4
Drain Channel Solid Model / Shell Model Stress Ratio**

Path #	$P_m + P_b$		
	Solid (psi)	Shell (psi)	Ratio
1	765	3,196	0.24
2	837		0.26
3	1,859		0.58
4	339		0.11
5	227		0.07
6	1,029		0.32
7	812		0.25
8	549		0.17
9	791		0.25
10	1,022		0.32
11	1,859		0.58
12 ⁽¹⁾	2,586		0.57
		Maximum =	0.58

Note: (1) The linearization stress path is subject to shell model stress attenuation distance of 0.25".

See "DrainChannelSummary.xls" (Appendix A) for detailed calculation.

Summary

The maximum stress ratio for the solid model stress intensity / shell model stress intensity is 0.58.



6.0 CONCLUSIONS

The stress intensity comparison shows that the stress intensities computed using the stress linearization approach for the solid elements (with the weld modeled) are lower than the stress intensities computed using the shell elements (without the weld modeled).

Stiffener

The solid model / shell model stress ratio for the stiffener is 0.79. This ratio is applicable to the stiffener shell stress intensity at the bottom of the welded connection between the stiffener and the hood.

Drain Channel

The solid model / shell model stress ratio for the drain channel is 0.58. This ratio is applicable to the drain channel shell stress intensity at the bottom of the welded connection between the drain channel and the skirt.

7.0 REFERENCES

1. Email with attachments from George Nelson (TVA) to Marcos Herrera (SI) on 04/21/08 at 10:54 am, "Re:," SI File No. BFN-15-225.
2. Email with attachments from George Nelson (TVA) to Marcos Herrera (SI) on 04/22/08 at 9:02 am, "Steam Dryer - Drain Channel," SI File No. BFN-15-224.
3. Email with attachment from Alexander Boschitsch (CDI) to Rick Cutsinger (TVA) on 05/08/08 at 10:27 am, "Weld Stresses," SI File No. BFN-15-223.
4. Email with attachment from Rick Cutsinger (TVA) to Soo Bee Kok (SI) on May 20, 2008 @9:02 am, "RE: Weld Structure Evaluation," SI File No. BFN-15-227.
5. ANSYS Mechanical, Release 11.0 (w/ Service Pack 1), ANSYS, Inc., August 2007.

Appendix A - Computer Files



Filename	Description
StiffSH5.inp	Stiffener Shell Model analysis input.
StiffSM5.inp	Stiffener Solid Model analysis input.
StiffSM5PP.inp	Stiffener Solid Model post-processing input.
DCSH42.inp	Drain Channel Shell Model analysis input.
DCSM42.inp	Drain Channel Solid Model analysis input.
DCSM42PP.inp	Drain Channel Solid Model post-processing input.
StiffenerSummary.xls	Stiffener result summary spreadsheet.
DrainChannelSummary.xls	Drain Channel result summary spreadsheet.

ENCLOSURE 7

**TENNESSEE VALLEY AUTHORITY
BROWNS FERRY NUCLEAR PLANT (BFN)
UNITS 1, 2, AND 3**

**TECHNICAL SPECIFICATIONS (TS) CHANGES TS-431 AND TS-418
EXTENDED POWER UPRATE (EPU)**

**RESPONSE TO ROUND 15 GROUP 4 AND ROUND 17 REQUEST FOR ADDITIONAL
INFORMATION (RAI)**

Attached is the non-proprietary version of the responses to Round 15 Group 4 and Round 17 RAI.

NON-PROPRIETARY INFORMATION

NRC RAI EMCB.129/96 (Revised Response)

The 218 herz (Hz) tones in the Browns Ferry Nuclear (BFN) plants caused by the blind flanges were predicted prior to main steam line (MSL) measurements in Table 1 on page 23 of GENE-0000-0052-3661-01, *Test Report #1, Browns Ferry Nuclear Plant, Unit 1, Scale Model Test of Enclosure 1* to a letter dated April 13, 2006. The table also shows that main steam relief valve (MSRV) tones may occur near 120 Hz in Unit 1, and the report states that the MSRV tones will be strongest just below extended power uprate conditions. Strong safety relief valve (SRV) tones have been shown to be detrimental to steam dryers in nuclear power plants based on the experiences at Quad Cities.

...

- (b) Discuss how Tennessee Valley Authority (TVA) will address the appearance of any strong MSRV tones in any of the BFN Units that challenge dryer stress limits. This discussion should include any plant data which shows that the tones, if they appear, will not be strong enough to drive dryer stresses above the American Society of Mechanical Engineers Code fatigue limit.

...

TVA Response to EMCB.129/96

- (b) A response to this RAI was previously provided in the January 31, 2008 submittal, "Response to Round 15 Request for Additional Information (RAI) Regarding Steam Dryer Analyses," (ML080380560). As discussed in the previous response, TVA planned to determine bump up factors based on 1/8 scale model testing to help predict increases in dryer stresses associated with any safety relief valve (SRV) resonances.

Subsequently, TVA has decided to install acoustic side branches (ASB) on the MSLs to preclude SRV resonance at increased power levels. This decision was discussed with the NRC staff during the April 17, 2008 meeting.

Prior to operating at EPU conditions, TVA plans on installing ASBs on the SRVs in the main steam flow stream as a plant modification evaluated under 10 CFR 50.59. The design of the BFN ASBs will be based on the proven ASB design that was utilized at Quad Cities to absorb the energy of the acoustic standing wave associated with the SRV standpipes. Design of the ASBs for Unit 1 is currently being performed and will include lessons learned from the experience at Quad Cities. Scale model testing will be utilized to facilitate the design characteristics of the ASBs.

Installation of ASBs will preclude the need to determine bump up factors to help predict increases in dryer stress that will be seen during power ascension associated with SRV resonances. Power ascension limit curves and published dryer stress margins will continue to be based on actual plant data and will be used to monitor dryer stresses during power ascension from current licensed thermal power (CLTP) to EPU power levels.

NRC RAI EMCB.130/97

During the upcoming Unit 3 Spring 2008 refueling outage, the eight unused standpipes in MSLs A and D, which are believed to cause strong 218 Hz tones in the plant on Unit 3, will be

NON-PROPRIETARY INFORMATION

plugged. Additionally, the Unit 3 MSLs will be instrumented and the acoustic pressures will be measured. Provide the following information:

- (a) analyses or test reports that explain the nature of the 218 Hz tones, along with the proposed changes to the standpipes and a demonstration that the changes will eliminate the tones;
- (b) a revised stress analysis for Unit 3 based on the Unit 3 MSL strain gage measurements; and
- (c) limit curves for Unit 3 based on the stress results in item (b).

TVA Response to EMC.B.130/97

A response to this RAI was initially provided in the January 31, 2008 submittal. In the previous response, TVA discussed the plans to install acoustic vibration suppressors (AVS) and MSL strain gages on Unit 3 during the Spring 2008 outage. These activities are discussed below.

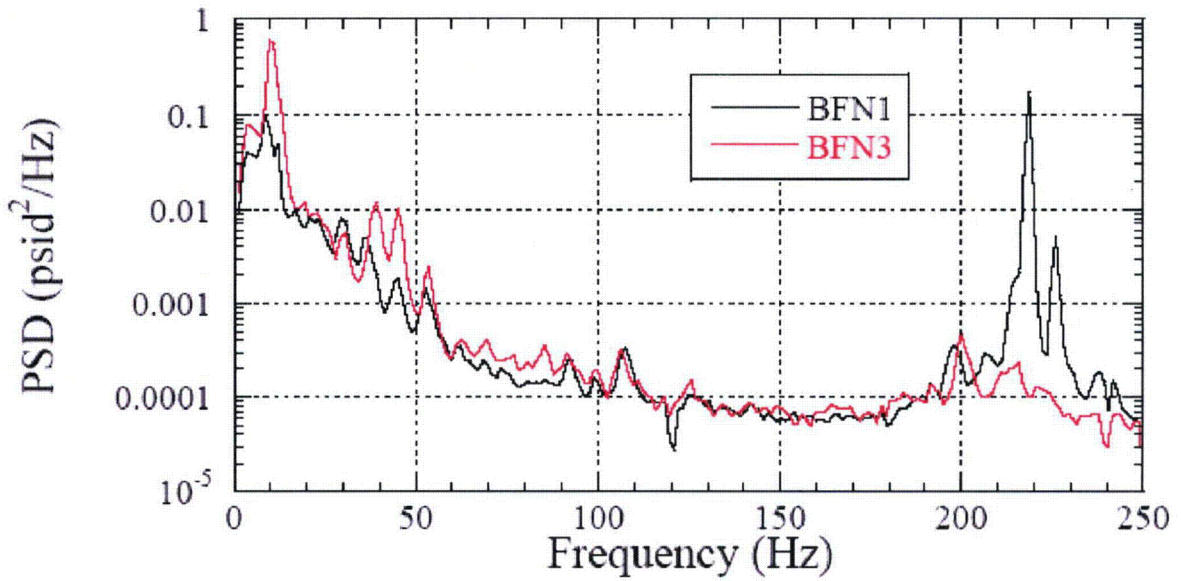
During the recent refueling outage on Unit 3, TVA installed AVSs and MSL strain gages as previously planned. During startup, the MSL strain gages experienced a high rate of failure. The set of operable strain gages (10 of 64) that remain useable is not sufficient to define a Unit 3 specific dryer load using the Acoustic Circuit Model (ACM) needed for performance of the Unit 3 steam dryer analysis as committed; however, they provide data that can be used in the following discussion.

- (a) The nature of the 218 Hz tone, along with the proposed changes to the standpipes, was previously discussed in the reply to EMEB.124/91 in the November 21, 2007 submittal, "Response to Preliminary Findings on Steam Dryer Stress Analysis," (ML073330483).

AVSs were installed in Unit 3 during the recent refueling outage on the blind flange standpipes in the MSL flow stream. Examination of the operable strain gages on the Unit 3 MSLs indicates that the 218 Hz tone has been eliminated. This is illustrated in Figures EMC.B.130/97-1 through 5. In these figures, data from the Unit 3 single strain gages at 100 percent power with AVSs installed are compared with data from Unit 1 single strain gages at 100 percent power at equivalent locations with no AVSs installed. In cases where the Unit 1 strain gage at the same location was inoperable, the diametrically opposite strain gage was used for comparison. Line noise and reactor recirculation system frequencies were filtered. The 218 Hz signal was not filtered on either unit.

- (b) Due to the failure of the Unit 3 MSL strain gages, the Unit 3 steam dryer stress analysis cannot be completed as originally scheduled. Since these gages are located in the drywell, necessary repairs will require a plant outage of sufficient duration to allow troubleshooting and replacement of the instrumentation. Following repair of the strain gages, a revised steam dryer stress analysis will be completed utilizing the load definition based on Unit 3 MSL strain gage data. The revised stress analysis will be performed with the same methodology used for the Unit 1 and Unit 2 steam dryer stress analyses.
- (c) Following the completion of the Unit 3 stress analysis discussed in (b) above, Unit 3 steam dryer limit curves will be generated. The method to generate the limit curves will be the same as previously used in the generation of the limit curves for Units 1 and 2.

Browns Ferry: MSL A Upper (Channel 1)



Browns Ferry: MSL A Upper (Channel 4)

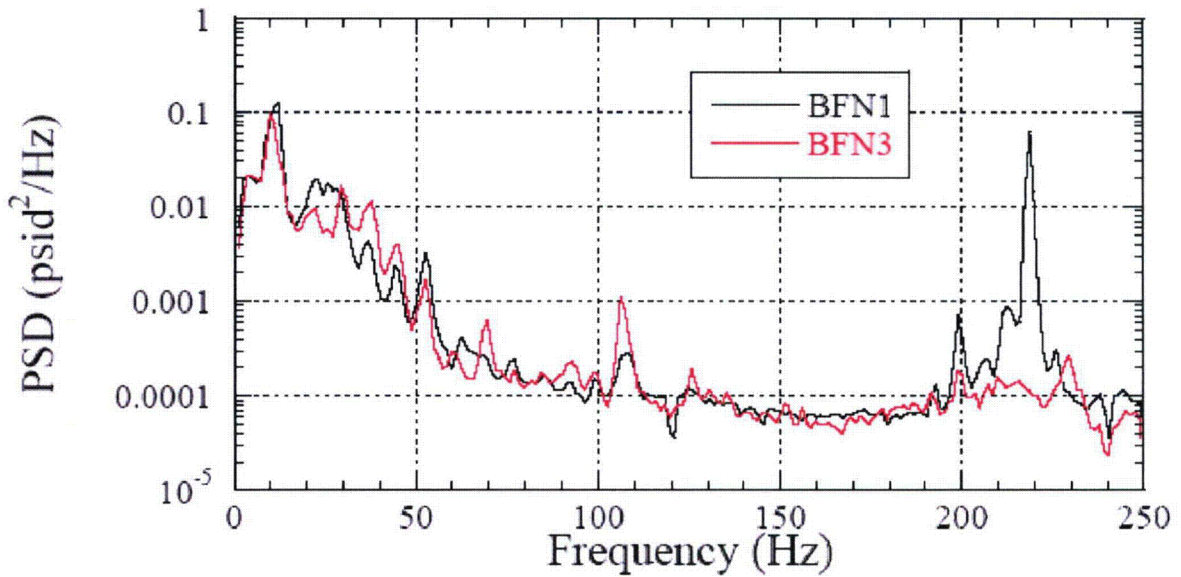
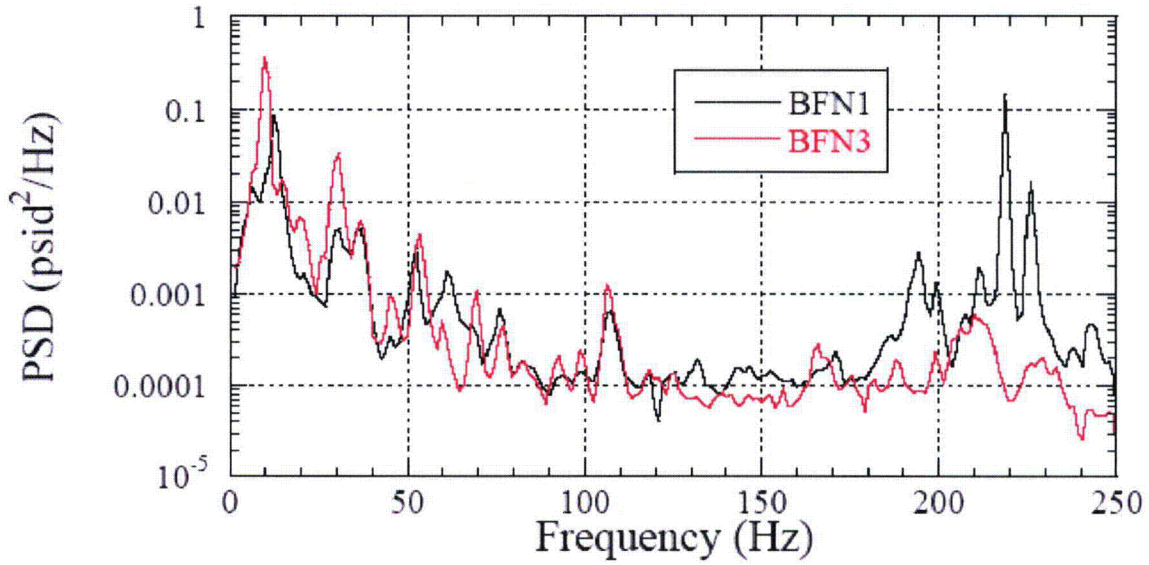


Figure EMCB.130/97-1: PSD comparison of pressure measurements on MSLs for Unit 1 and Unit 3

Browns Ferry: MSL A Lower (Channel 5)



Browns Ferry: MSL A Lower (Channel 8)

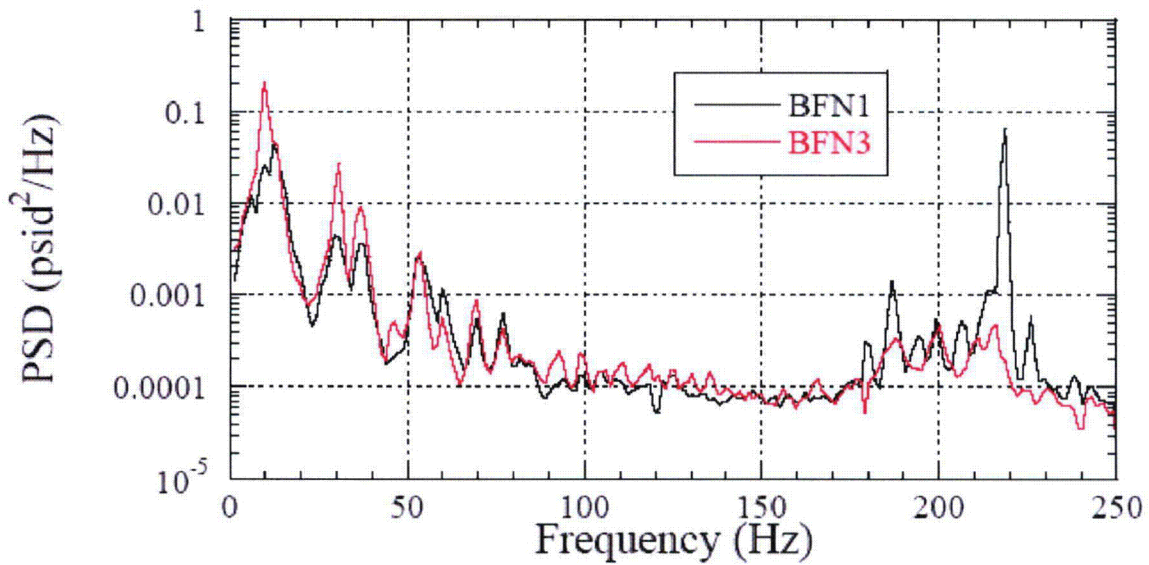
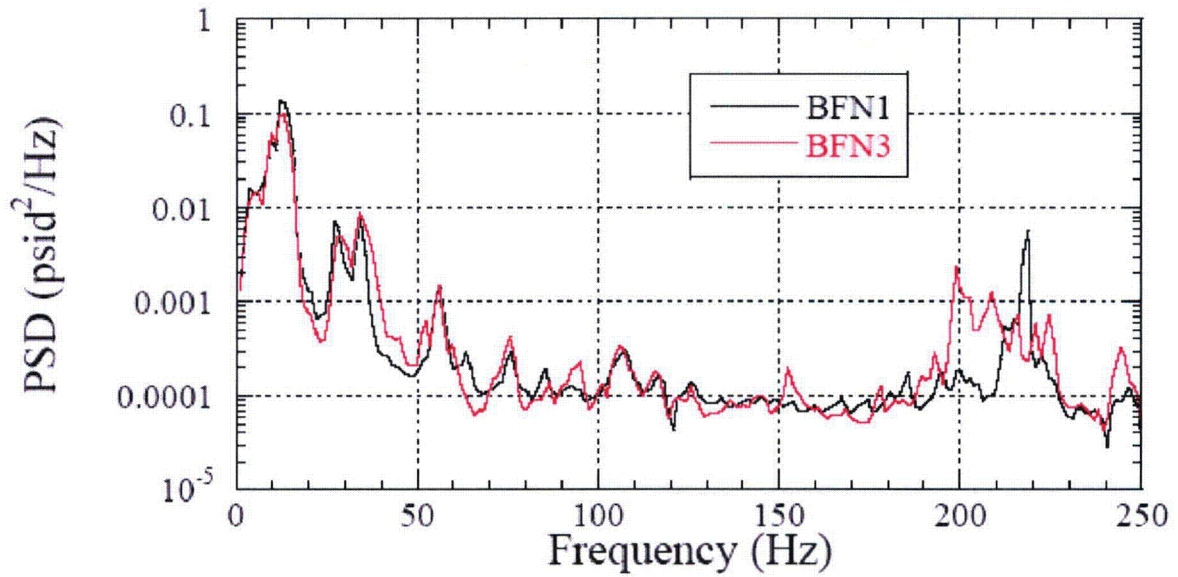


Figure EMCB.130/97-2: PSD comparison of pressure measurements on MSLs for Unit 1 and Unit 3

NON-PROPRIETARY INFORMATION

Browns Ferry: MSL B Lower (Channel 13)



Browns Ferry: MSL B Lower (Channel 14)

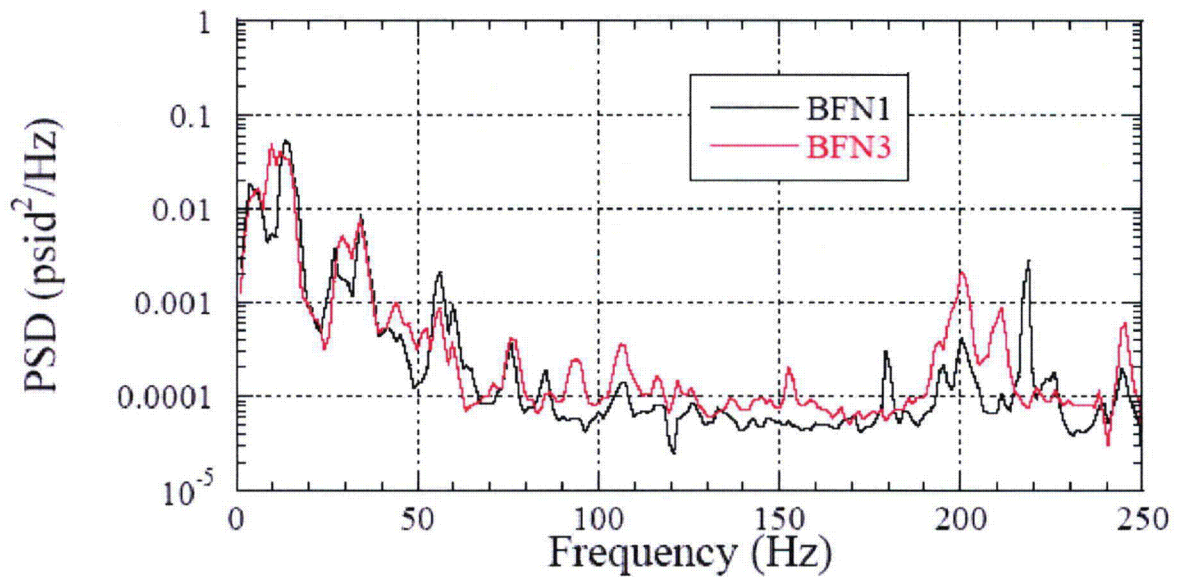
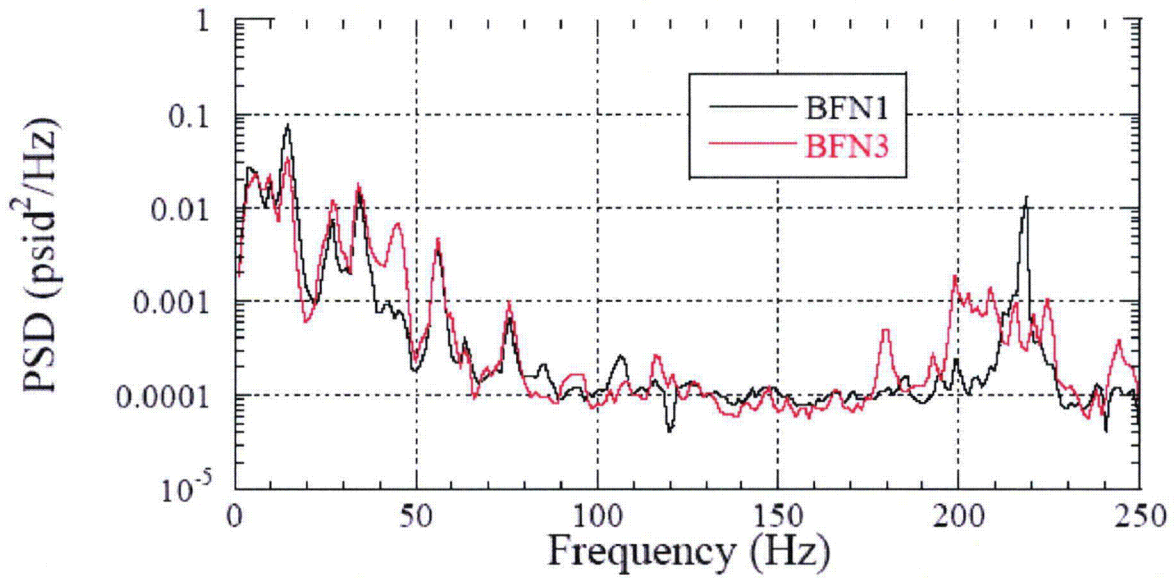


Figure EMCB.130/97-3: PSD comparison of pressure measurements on MSLs for Unit 1 and Unit 3

NON-PROPRIETARY INFORMATION

Browns Ferry: MSL B Lower (Channel 15)



Browns Ferry: MSL B Lower (Channel 16)

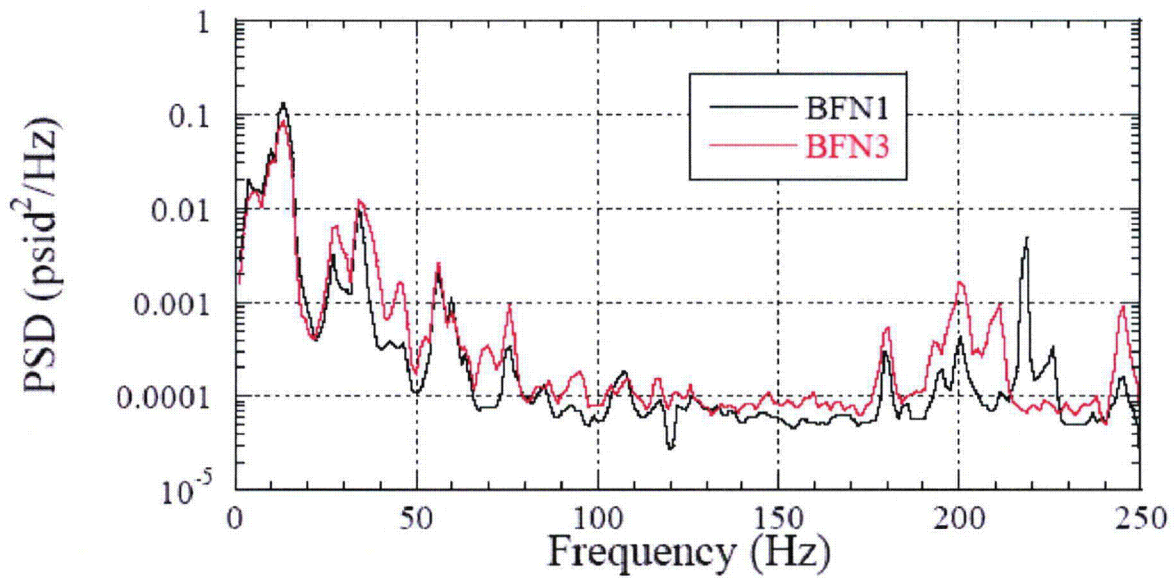
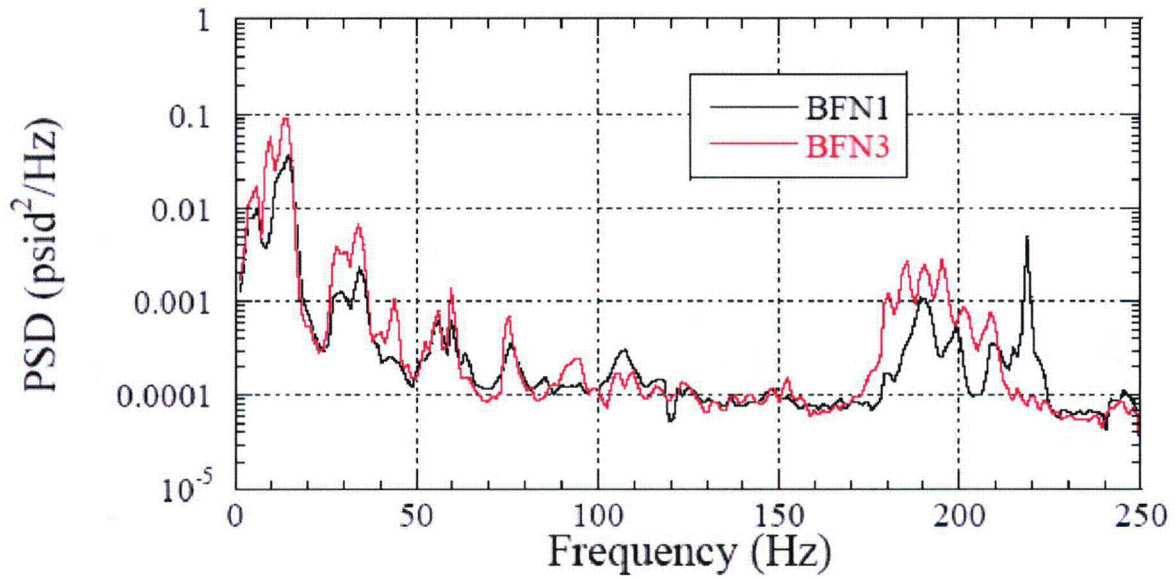


Figure EMCB.130/97-4: PSD comparison of pressure measurements on MSLs for Unit 1 and Unit 3

NON-PROPRIETARY INFORMATION

Browns Ferry: MSL C Lower (Channel 24)



Browns Ferry: MSL D Lower (Channel 30)

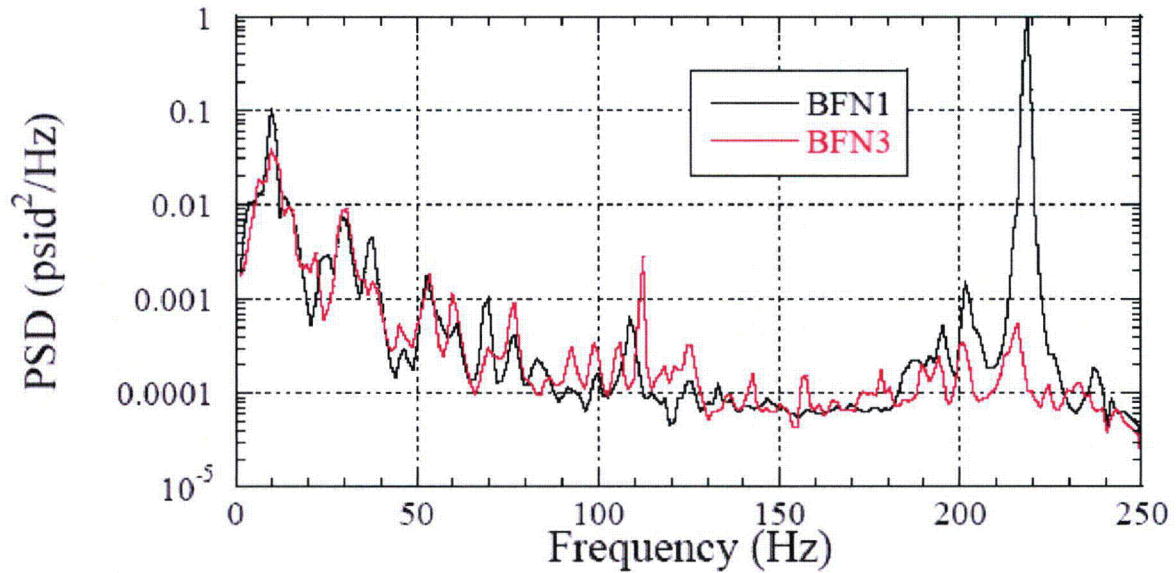


Figure EMCB.130/97-5: PSD comparison of pressure measurements on MSLs for Unit 1 and Unit 3

NON-PROPRIETARY INFORMATION

NRC RAI EMCB.166/133

Compare the revised Units 1, 2 and 3 limit curves to those for Hope Creek. For the Unit 1 limit curves, use the revised curves developed in response to RAI 165/132. For Unit 3 limit curves, use the curves developed in response to RAI 130/97. Also compare these limit curves to the MSL measurements for Quad Cities Unit 2 data at OLTP conditions prior to the installation of Acoustic Side Branches on the SRVs.

TVA Response to EMCB.166/133

A response to this RAI was initially provided in the January 31, 2008 submittal. As discussed previously, the limit curves for Unit 3 will be revised utilizing unit-specific MSL strain gage data. Due to the Unit 3 MSL strain gage failures discussed in the response to RAI EMCB.130/97 in this submittal, the Unit 3 limit curves will be generated following the repair of the MSL strain gages.

NRC RAI EMCB.135 (Units 2 and 3 only)

TVA has indicated the intent to install main steam line (MSL) strain gages and Acoustic Vibration Suppressors in the blind flanges responsible for the 218 Hz tones currently present on Unit 3. Therefore, a revised stress analysis of the Unit 3 dryer, using Unit 3 loads, will need to be used to develop limit curves.

Provide information about the strain gage instrumentation, including number of strain gages at each of the eight MSL locations, as well as their connections (i.e., whether all the strain gages will be used simultaneously) and associated uncertainties. Address how a strain gage failure at a MSL location would affect the uncertainty.

TVA Response to EMCB.135 (Units 2 and 3 only)

For BFN Units 1, 2, and 3, eight strain gages per elevation were installed at two locations on each main steam line (referred to as the "Upper" and "Lower" elevations). All strain gages were mounted in the hoop direction and in pairs 180 degrees apart. These strain gages measure the hoop strain and, thus, indirectly obtain the dynamic steam pressure inside the MSL. The hoop strain is also influenced by bending strain of the pipe. In order to minimize the bending error, the strain gages pairs are connected to a Wheatstone bridge in a half bridge configuration such that the signals from the individual strain gages are additive resulting in the cancellation of the bending strain and enhancement of the hoop strain sensitivity. For each MSL elevation, the four signals are averaged to minimize the bending errors and improve the signal to noise ratio.

Uncertainties associated with pressure measurement (strain gage) and pressure sensor location was previously discussed in the response to RAI EMCB.155/122 provided in the March 6, 2008 submittal, "Response to Round 15 Request for Additional Information (RAI) Regarding Steam Dryer Analyses, Group 2." Similar to Units 1 and 2, the uncertainty values for the Unit 3 strain gages will be provided in the Unit 3 load report.

In the case of a failure of a strain gage, the remaining strain gage in the half bridge is reconfigured into a quarter bridge. Eight strain gages (four strain gage pairs) at each MSL elevation allows measurement to continue with strain gage failures. The loss of several strain gages at a MSL location would result in a negligible change to the measurement uncertainty since the overall uncertainty is meant to relate the pressure uncertainty to the component uncertainties in the geometry, material property and the uncertainty in the strain measurement. Changes to the geometry due to the elimination of a few strain gages will not appreciably affect

NON-PROPRIETARY INFORMATION

the uncertainty since the uncertainty at the eight strain gage locations are combined into one uncertainty.

NRC RAI EMCB.168/136

For the Browns Ferry Nuclear Plant (BFN) units;

- (a) Describe the evolution of BFN tie bar design including the latest tie bar modification;
- (b) Explain how the difference between the BFN and Susquehanna steam dryer designs (slanted hood versus curved hood) affect the amplitude of the 15 Hz frequency, which is the resonance frequency associated with the MSL dead legs, present in the MSL strain gage signal. Discuss the insights into the cause(s) of the 15 Hz tones which can be inferred from Unit 3 low power MSL measurements.

TVA Response to EMCB.168/136

- (a) The original steam dryer tie bars were 1 inch x 1 inch x 3/16 inch thick stainless steel angle iron. Based on the operating history of the tie bars (see the response to RAI EMCB.134/101 in the March 6, 2008 submittal), the original tie bars have been replaced on Unit 1 with a revised design by General Electric (GE). These tie bars are 1 inch x 2.5 inch solid stock which are attached to the dryer banks with a gusset foot. This design is illustrated in Figure EMCB.168/136-1.

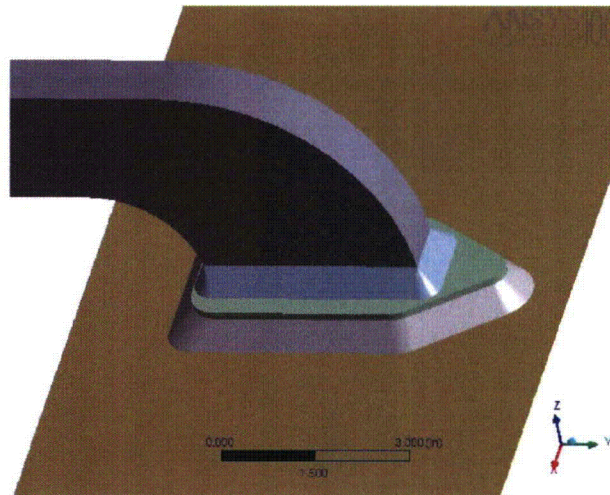


Figure EMCB.168/136-1: GE replacement tie bar design

In order to improve stress margins for the steam dryers, TVA has designed new tie bars that will be installed on all three BFN units. This new tie bar is constructed with 1 inch x 2 inch solid stock with modified attachments to the dryer banks. The new tie bar design is discussed and illustrated in the response to RAI EMCB.180 in this submittal.

- (b) Peaks in the MSL strain gage measurements at approximately 15 Hz have been identified at the two plants that have MSL dead legs as part of their design. As

NON-PROPRIETARY INFORMATION

presented in the response to RAI EMCB.133/100 in the January 31, 2008 submittal, the calculated resonance frequency of the dead legs on the B and C MSLs at BFN is 15 Hz. TVA does not have data or analysis that relates the steam dryer design to the amplitude of the 15 Hz frequency.

The 15 Hz loading is accounted for in the ACM which maps this load across the surfaces of the dryer. For BFN Units 1 and 2, the 15 Hz loading is shown as a contributor but not a dominant frequency in the stress analyses. See the response to EMCB.138/105 in the March 6, 2008, submittal for Unit 1 and the response to EMCB.146/113 in the April 4, 2008, submittal, "Response to Round 15 and Round 16 Requests for Additional Information (RAI) Regarding Steam Dryer Analyses, Group 3," for Unit 2.

A full set of MSL strain gages were not available to provide low power MSL measurements on Unit 3. However, low power MSL strain gage measurements were examined on Units 1 and 2. The 15 Hz peaks are established at low plant power levels and grow in amplitude while maintaining constant frequencies as the plant comes up in power.

NRC RAI EMCB.169/137

- (a) The BFN operating experience reveals that the steam dryers have experienced high-cycle fatigue cracking at three locations: vertical weld of drain channel of all three units in 1988-to-1992 period, Unit 3 tie bar failure in 2003, and Unit 1 support beam welded connection to support ring in 2006. Generally, high-cycle fatigue failures take place in the first few months of operation. However, the fatigue cracking in BFN steam dryers has occurred after 12 to 30 years of operation.

Address why it took so long for the cracking to be observed. Provide time histories of the stress intensities at these three failure locations and identify the frequencies of the highest alternating stress intensities that may be responsible for the observed cracking. Additionally, provide the root cause analyses reports for these three failures.

- (b) The justification for the high-cycle fatigue failure of the BFN drain channels, indicates that the original fillet welds on the channels may have had root defects. Therefore it appears that the high fatigue strength reduction factor (3.6) should be used. This factor is twice the one used in the stress analysis presented in Continuum Dynamics, Inc. (CDI) Report 07-06P.

Address why the higher fatigue strength reduction factor for the fillet welds, which might have root defects, is not used in the stress analyses of the dryers presented in CDI Reports 07-06P and 08-06P.

- (c) Regarding the fatigue failure of Unit 3 tie bar in 2003, confirm whether fatigue failure has occurred through the base metal, away from the weld. Provide a description of the loading acting on the tie bar and of its design.
- (d) As the purpose of the response to EMCB 134/101 was to assess the consistency of the stress analysis in lieu of support of the failure of the support beam; it appears that the observed failure of the support beam is not a fatigue failure. Explain the root cause of this failure, whether the fractured surface of the beam was flat, and if it revealed the presence of any plastic deformation.

NON-PROPRIETARY INFORMATION

TVA Response to EMCB.169/137

- (a) Each of the structural items noted is discussed below.

Drain Channels

In October 26, 1988, GE issued Service Information Letter (SIL) No. 474, "Steam Dryer Drain Channel Cracking," which advised BWR owners that cracks in the welds that attach the drain channels to the steam dryer skirt had been identified at several plants. In the SIL, GE's evaluation of the appearance of the cracking and analysis of potential sources of stress on the welds indicate that high cycle fatigue initiated the cracks in the drain channel welds.

At the time the SIL was issued, all three BFN units were in an extended shutdown. The drain channel weld cracks seen at BFN were identified during steam dryer inspections in response to the SIL prior to power operation of each unit after the extended shutdowns. Weld repair and reinforcement as provided by GE were made at that time.

It is not known how long the drain channel weld cracks existed prior to inspection in accordance with the SIL. No additional root cause analysis was performed further than what was provided in the GE SIL.

The stress time history for BFN Unit 2 Node 105514 on the drain channel (see Table EMCB.146/113-1 and Figure EMCB.146/113-9 in the April 4, 2008 submittal) is provided in Figure EMCB.169.137-1. This figure is based upon the Unit 2 stress analysis provided in the April 4, 2008 submittal. This stress analyses does not reflect the original design of steam dryers at the time the drain channel welds were cracked nor does it include the 218 Hz blind flange frequency which is being removed by the installation of the AVSs.

NON-PROPRIETARY INFORMATION

Node 105514, σ_{yy}

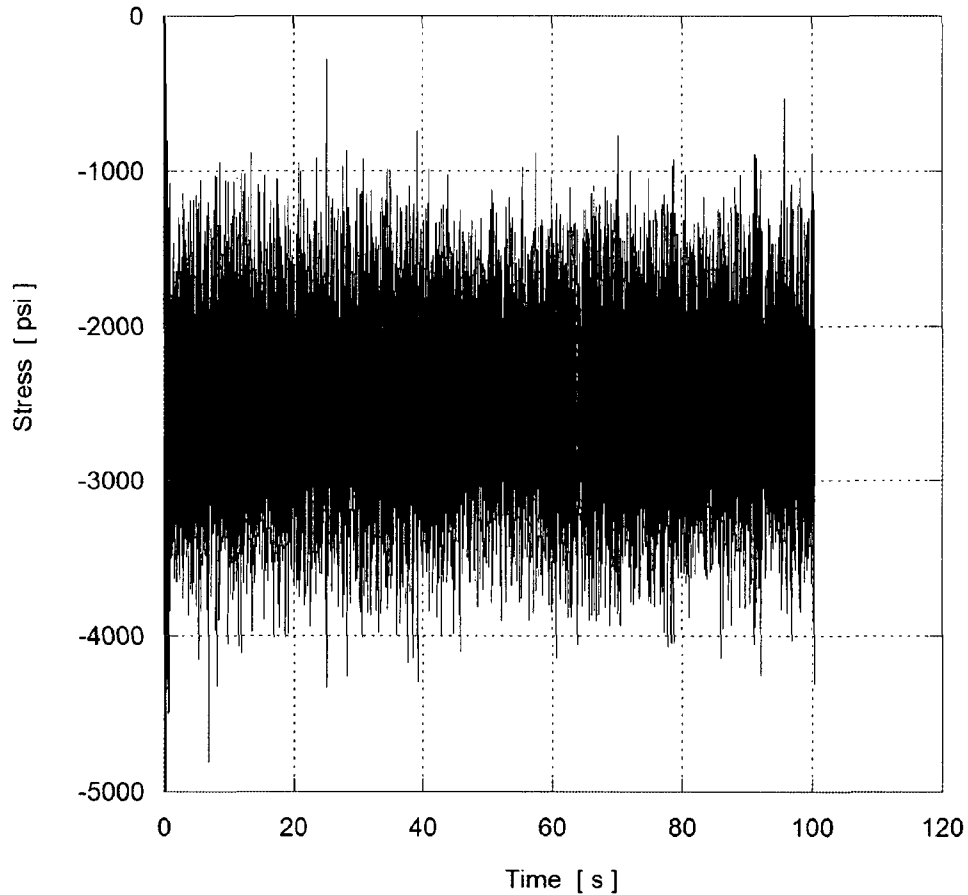


Figure EMCB.169/137-1: Time History for Drain Channel Unit 2 Node 105514

Tie bars

In 2003, during a mid-cycle outage, three of the original 1 inch x 1 inch x 3/16 inch angle iron tie bars in Unit 3 were observed to have failed. In each case the tie bar had failed at one end, near the weld between the tie bar and the top of the dryer bank. The connecting welds were intact. GE dispositioned the failures at BFN based on similar tie bar failures at two other units with a steam dryer of the same design.

The tie bars at the similar units were examined in the laboratory visually and using a scanning electron microscope. The failure mechanism was determined to be due to fatigue with no indication of stress corrosion cracking. The loading that resulted in the tie bar failures was not identified. The failed tie bars on the BFN steam dryer were visually identical to those examined from the similar plants and, therefore, were considered to have failed due to fatigue. No additional root cause analysis was performed for BFN.

NON-PROPRIETARY INFORMATION

The failed tie bars were identified during re-installation of the steam dryer during mid-cycle activities and were not identified as part of planned steam dryer inspections. It is not known how long the tie bar failures existed at the time of discovery.

The stress time history for BFN Unit 1 Node 88059 on the top cover by the tie bar attachment (see Table EMCB.170/138-1 and Figure EMCB.170/138-1 in this submittal) is provided in Figure EMCB.169.137-2. This figure is based upon the Unit 1 stress analysis provided in the March 6, 2008 submittal. This stress analysis does not reflect the original design of steam dryers and tie bars at the time the tie bar failure occurred nor does it include the 218 Hz blind flange frequency which is being removed by the installation of the AVSs.

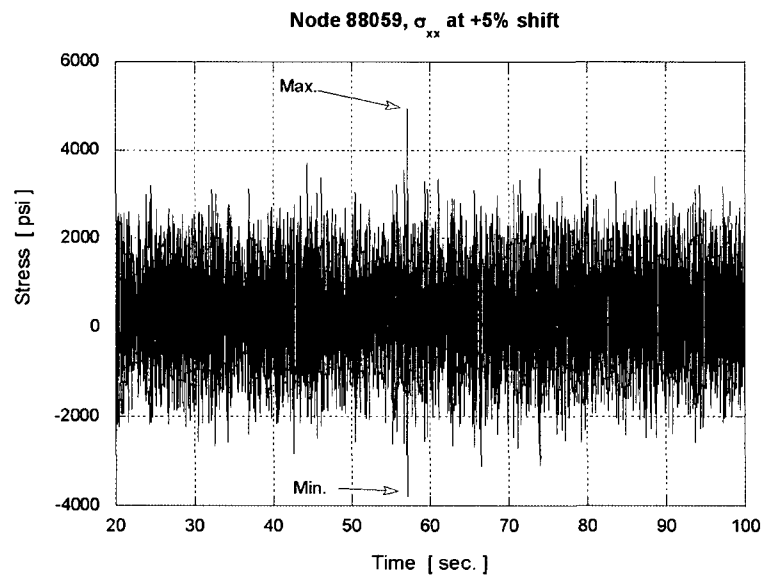


Figure EMCB.169/137-2: Time History for Top Cover Unit 1 Node 88059

Support Beam

When the Unit 1 steam dryer cover plate was removed during modifications, it was identified that the support beam stitch welds connecting the beam to the support ring had cracked at the welds. This beam was originally intended as a fabrication aid for vane bank assembly.

The location of this support beam interfered with the placement of the new cover plate. Since the support beam was not required by the stress analysis, the ends of the support beam were removed. No formal root cause analysis of the failure was performed since the attachment was not being preserved.

The failed support beam weld was identified during modification activities and was not identified as part of planned steam dryer inspections. It is not known how long the support beam failure existed at the time of discovery.

The stress time history for BFN Unit 2 Node 99056 on the support beam is provided in Figure EMCB.169/137-3. This figure is based upon the Unit 2 stress analysis provided

NON-PROPRIETARY INFORMATION

in the April 4, 2008 submittal. This stress analyses does not reflect the original design of steam dryers nor does it include the 218 Hz blind flange frequency which is being removed by the installation of the AVSs.

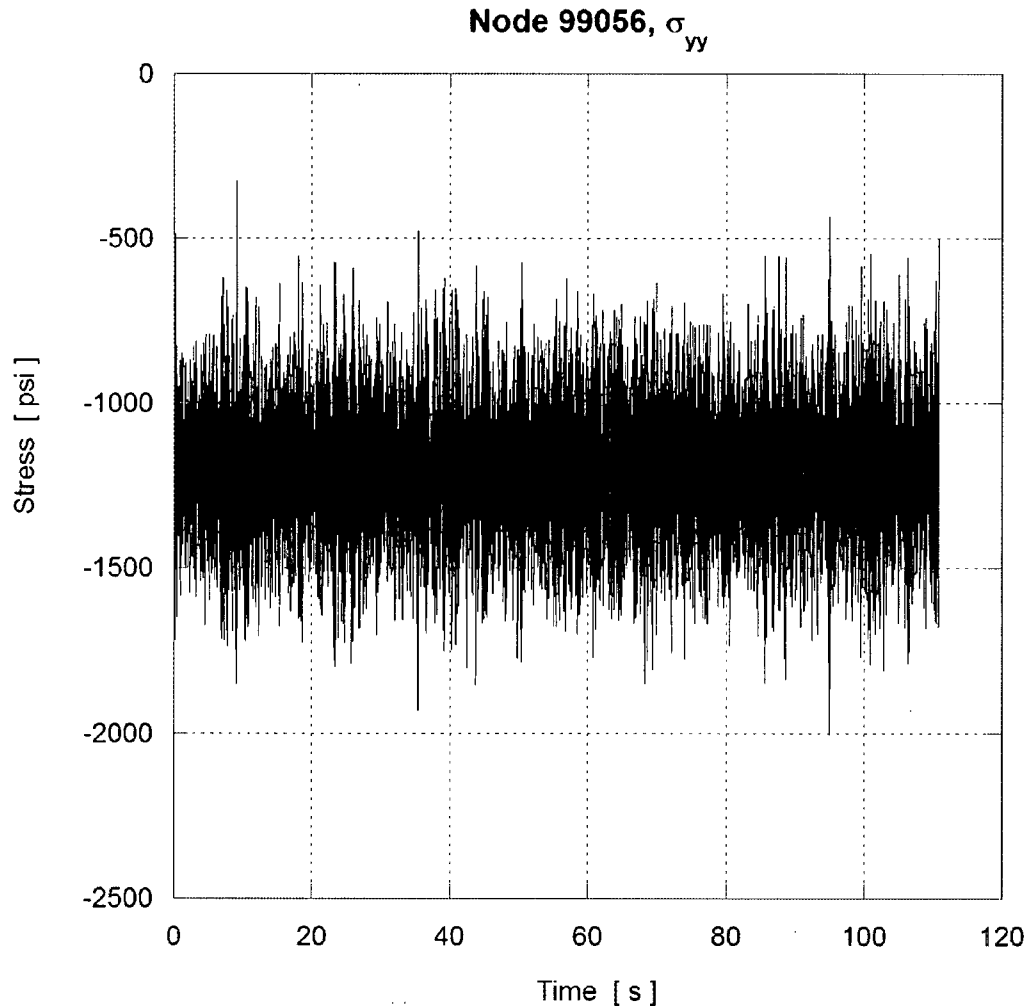


Figure EMCB.169/137-3: Time History for Support Beam Unit 2 Node 99056

- (b) The discussion of the drain channel weld cracks provided in the response to RAI EMCB.134/101 in the March 6, 2008 submittal was not intended to indicate that the drain channel welds contained root defects or that a larger weld factor should be used. This discussion was provided to demonstrate that the Unit 2 stress analyses, which were based on the modified steam dryer design including drain channel-to-dryer skirt weld reinforcement, would predict the drain channel failures seen on the original steam dryer design.

As indicated in GE SIL 474, several plants had experienced cracks in welds that attach the drain channels to the steam dryer skirt. This industry experience does not indicate a weld quality issue, but it does point to a common design problem in several steam dryers

NON-PROPRIETARY INFORMATION

that led to high cycle fatigue failure. The 1.8 weld fatigue factor remains appropriate for use in the BFN steam dryer analyses.

- (c) The design of the failed tie bars is discussed in the response to RAI EMCB.168/136 (a) in this submittal. The description of the failure is provided in part (a) above. The BFN steam dryer stress analyses modeled the modified tie bars and have not analyzed the failed tie bars. The analyses with the modified tie bars show that loading in the tie bar is primarily axial with some induced bending due to relative motions of the end points.
- (d) The failure of the support beam is discussed in part (a) above.

NRC RAI EMCB.170/138

- (a) For the nodes listed in Table EMCB 138/105-1 of the TVA response to EMCB 138/105 and located on shell elements, identify the section location and orientation of these components. For Top Cover/Tie Bar Base locations, discuss whether the plotted stress components act along the length of the tie bar. For locations including tie bars, indicate whether the dominating alternating loads acting on the tie bars are tensile loads or bending moments.
- (b) Provide accumulative power spectral density (PSD) curves of overall stress intensity, rather than individual stress components. Also, provide mode shapes (or unit MSL source driven dryer displacement response shapes) of the dryer at and near the peak stress frequencies of 34, 47, and 62 Hz. The mode shapes should show overall dryer vibration, as well as close-ups of smaller regions with strong vibration. For each mode shape, also show the motion of the perforated plates.

TVA Response to EMCB.170/138

The response to this RAI is based upon the analysis presented in CDI Report No. 08-06P, "Stress Assessment of Browns Ferry Nuclear Unit 1 Steam Dryer," Rev. 0, provided in the submittal dated March 6, 2008.

- (a) Figures EMCB.170/138-1 through 14 provide the location and orientation of the nodes with the lowest alternating stress ratios as discussed in the response to EMCB.138/105 in the March 6, 2008 submittal. Table EMCB.170/138-1 provides a correlation of the nodes to the appropriate figure. This table has been expanded from 10 to 14 nodes to facilitate the discussion in the response to RAI EMCB.180 in this submittal.

Figures EMCB.170/138-1 through 14 include orientation axes that correspond to the accumulative PSDs provided in Figures EMCB.138/105-1 through 10. For example, σ_{xx} denotes the stress component in the x direction which is in the direction of the length of the tie bars.

At Top Cover/Tie Bar Base locations such as shown in Figure EMCB.170/138-1, the stresses are primarily the result of local bending in various orientations in the cover plate adjacent to the tie bar pad plates. None of the locations with the lowest stress ratios is in the tie bars.

A review of finite element results indicated that the dominant load in the span of a tie bar is axial force with some bending also present. Due to the eccentricity of the tie bar axial centerline relative to the vane bank top cover, load at the tie bar pad-to-vane bank top cover interface is primarily bending, which is reacted as through-thickness bending in the

NON-PROPRIETARY INFORMATION

top cover plates. This observation led to the design of the new tie bars described in the response to RAI EMCB.180.

Table EMCB.170/138-1: List of nodes in the BFN Unit 1 dryer having the lowest alternating stress ratios

	Location	Node	SR-a	Figure
1.	Top Cover Inner Hood/Top Cover Overlap/Top Perf. Plate	88059	1.56	EMCB.170/138-1
2.	Top Cover/Tie Bar Base	107054	1.59	EMCB.170/138-2
3.	Top Cover/Tie Bar Base	102407	1.62	EMCB.170/138-3
4.	Top Cover Middle Hood/Top Perf.	91420	1.63	EMCB.170/138-4
5.	Top Cover/Tie Bar Base	96561	1.94	EMCB.170/138-5
6.	Top Perf/Top Cover/Dam Plate	103088	1.98	EMCB.170/138-6
7.	Submerged Drain Channel/Skirt	104539	2.15	EMCB.170/138-7
8.	Dam Plate/Lock	102521	2.19	EMCB.170/138-8
9.	Top Cover Inner Hood/Hood Support/Tie Bar Base	103094	2.28	EMCB.170/138-9
10.	Top Perf/Top Cover/Dam Plate	103089	2.40	EMCB.170/138-10
11.	Steam Dam to Top Cover Joint	93824	2.56	EMCB.170/138-11
12.	Inner Hood to Hood Support Joint at Bottom of Hood	94654	2.62	EMCB.170/138-12
13.	Steam Dam to Top Cover Joint	103082	2.67	EMCB.170/138-13
14.	(Not at weld joint) Steam Dam Lock Gusset at Contact Point with Tie Bar	107394	1.78	EMCB.170/138-14

NON-PROPRIETARY INFORMATION

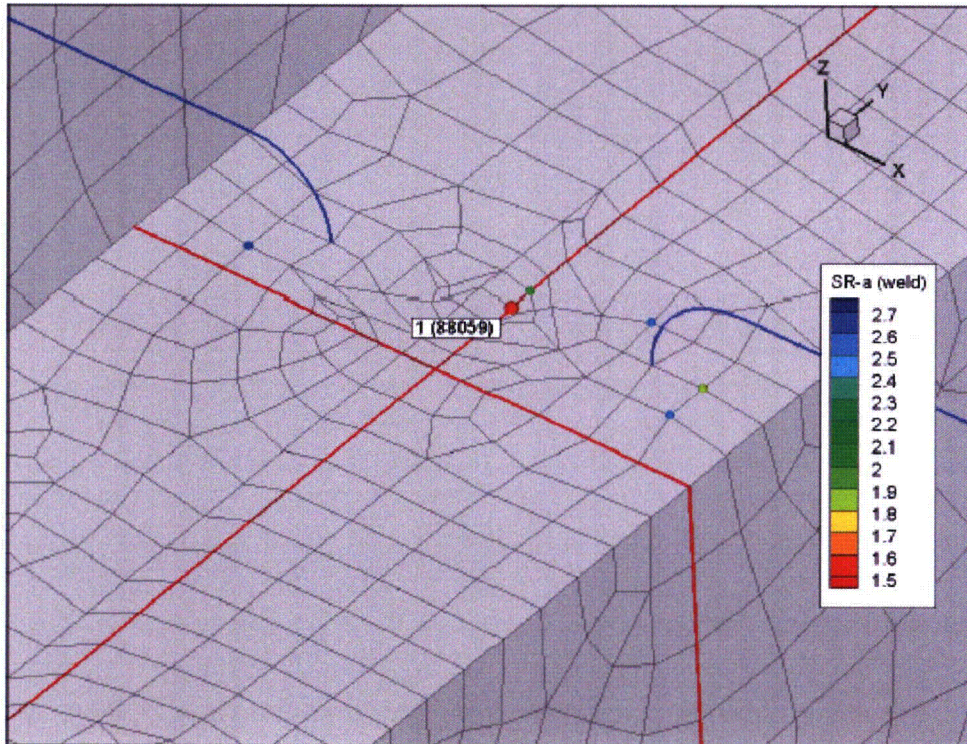
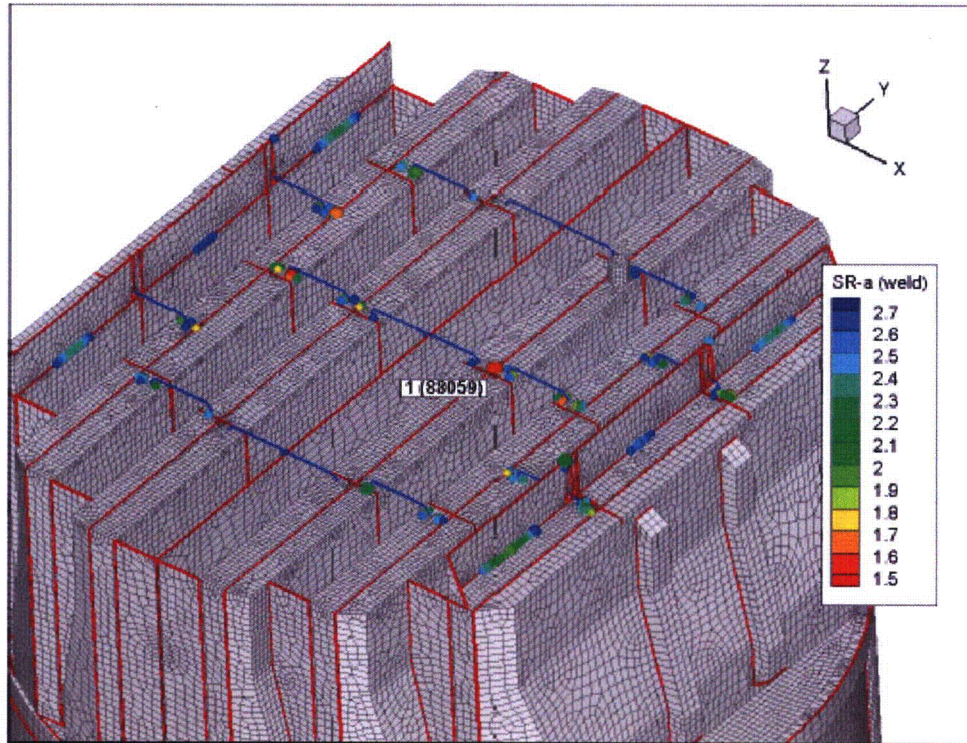


Figure EMCB.170/138-1: Node 88059

NON-PROPRIETARY INFORMATION

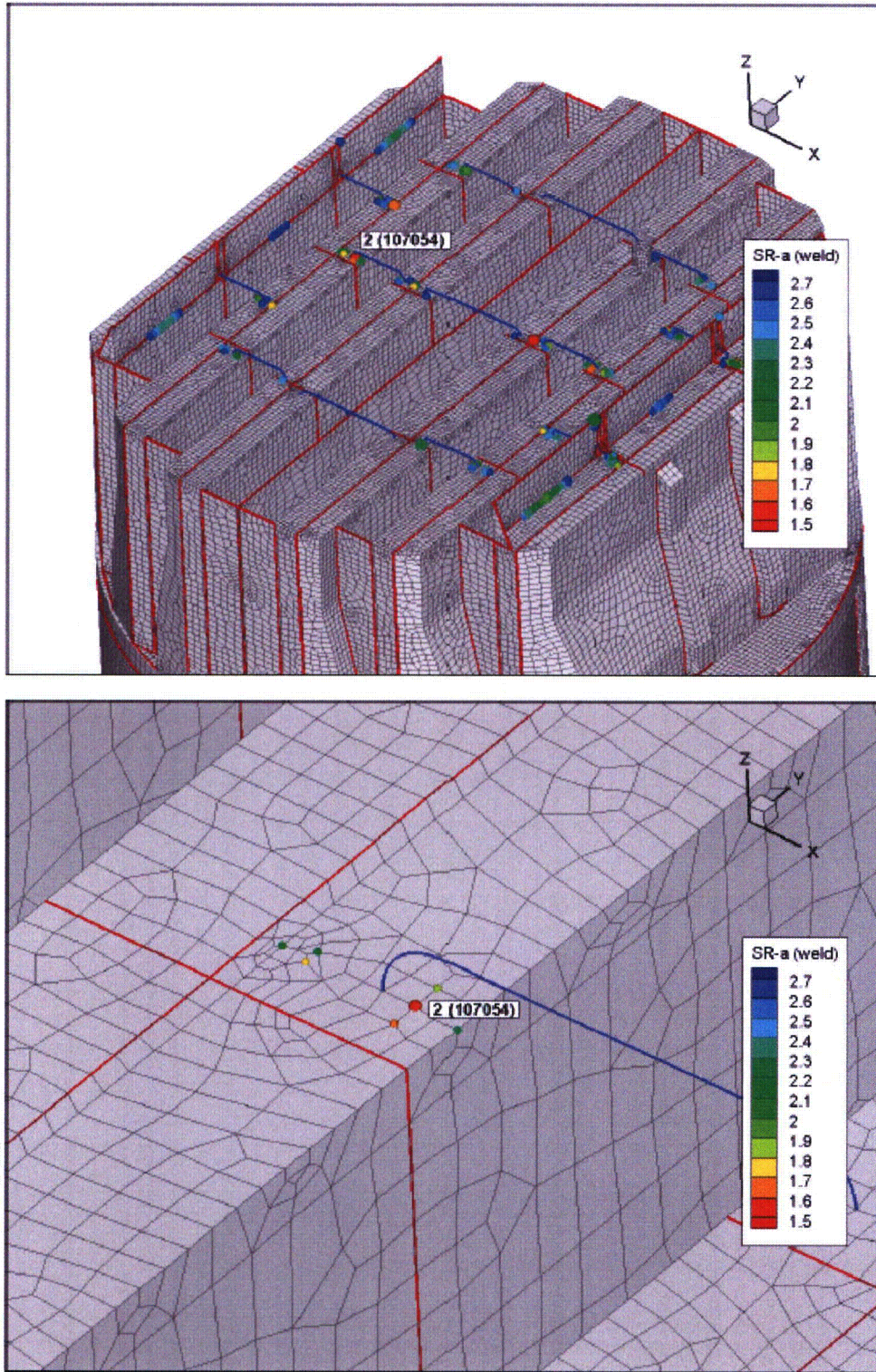


Figure EMCB.170/138-2: Node 107054

NON-PROPRIETARY INFORMATION

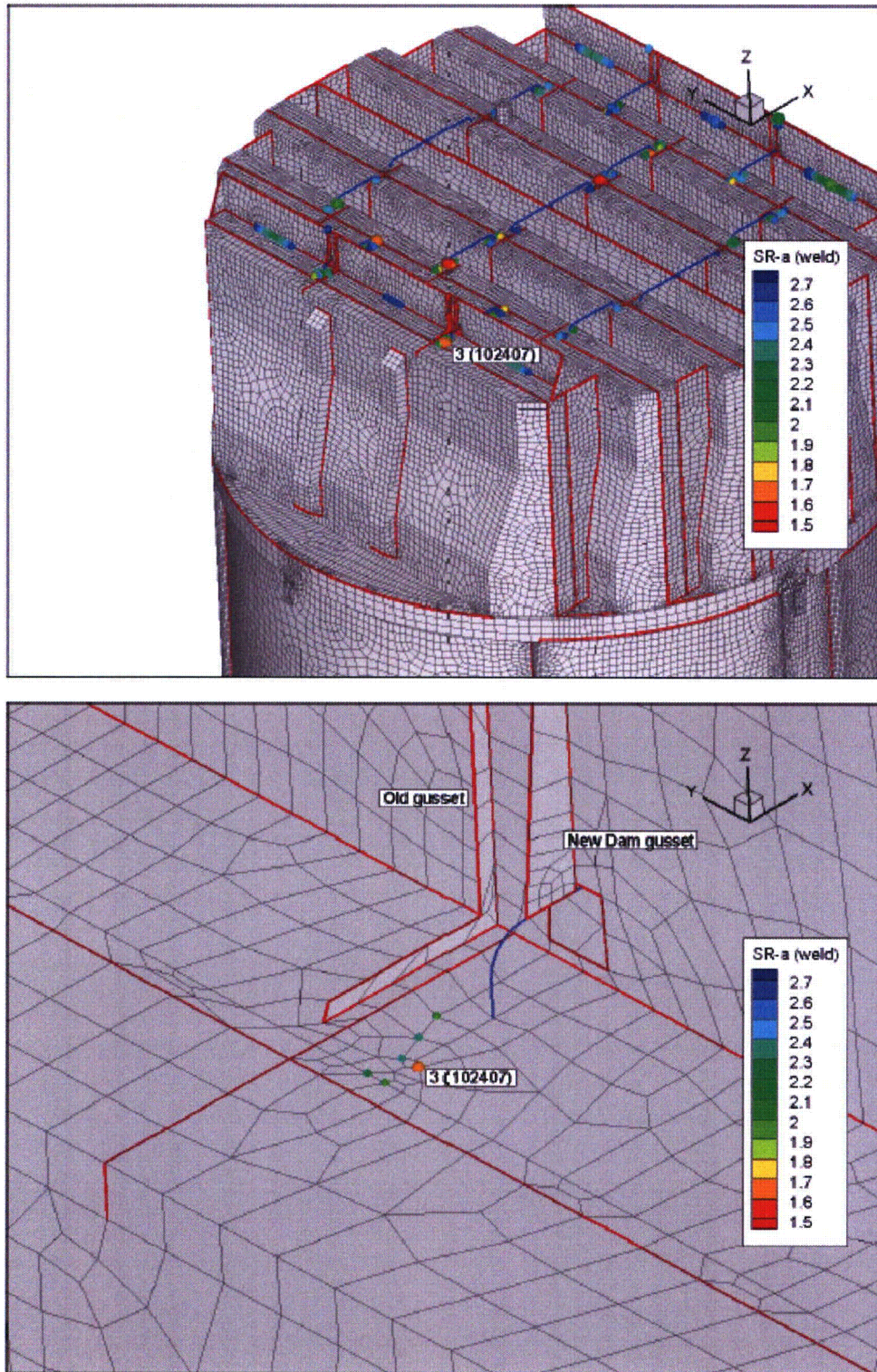


Figure EMCB.170/138-3: Node 102407

NON-PROPRIETARY INFORMATION

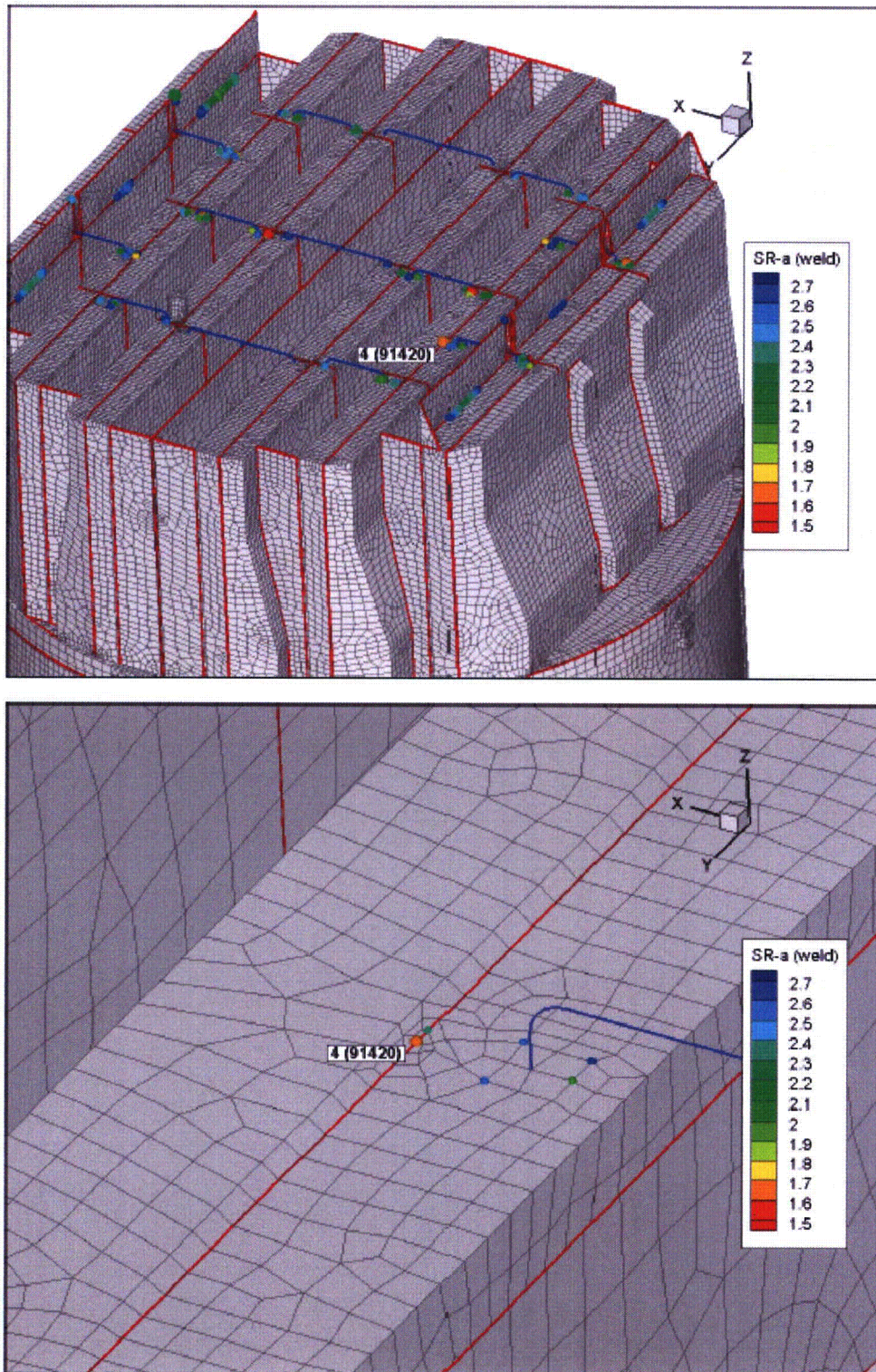


Figure EMCB.170/138-4: Node 91420

NON-PROPRIETARY INFORMATION

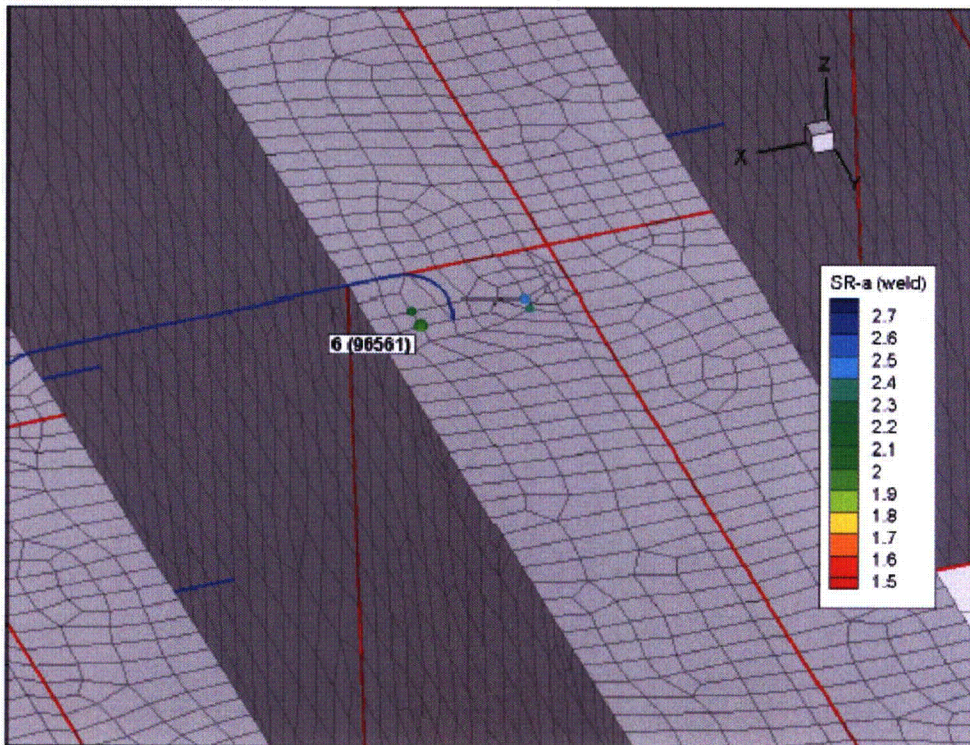
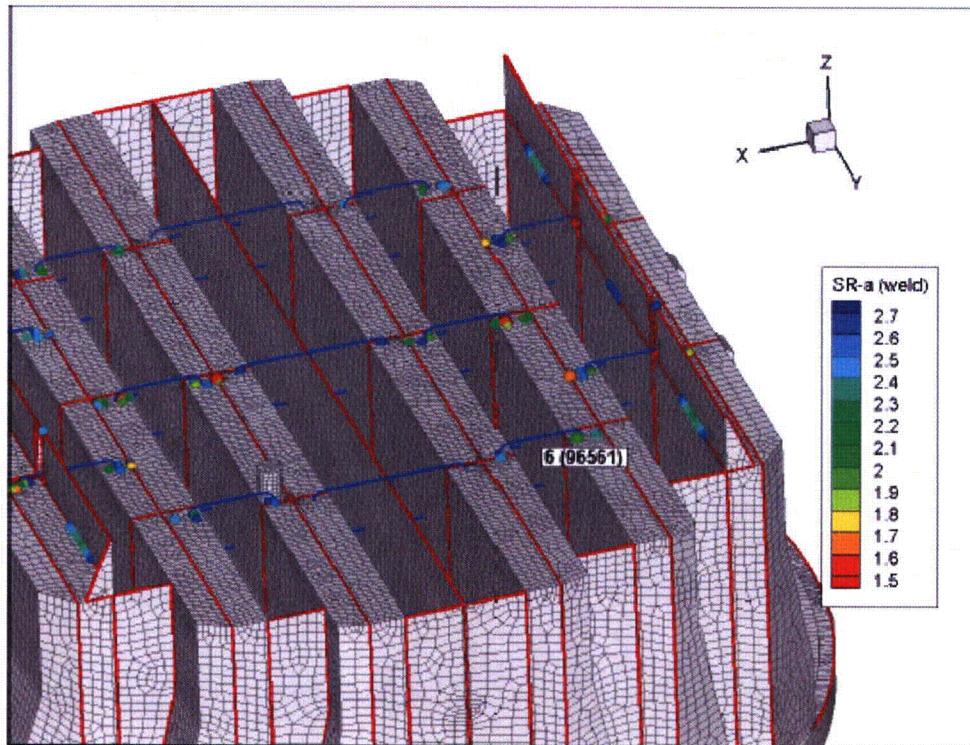


Figure EMCB.170/138-5: Node 96561

NON-PROPRIETARY INFORMATION

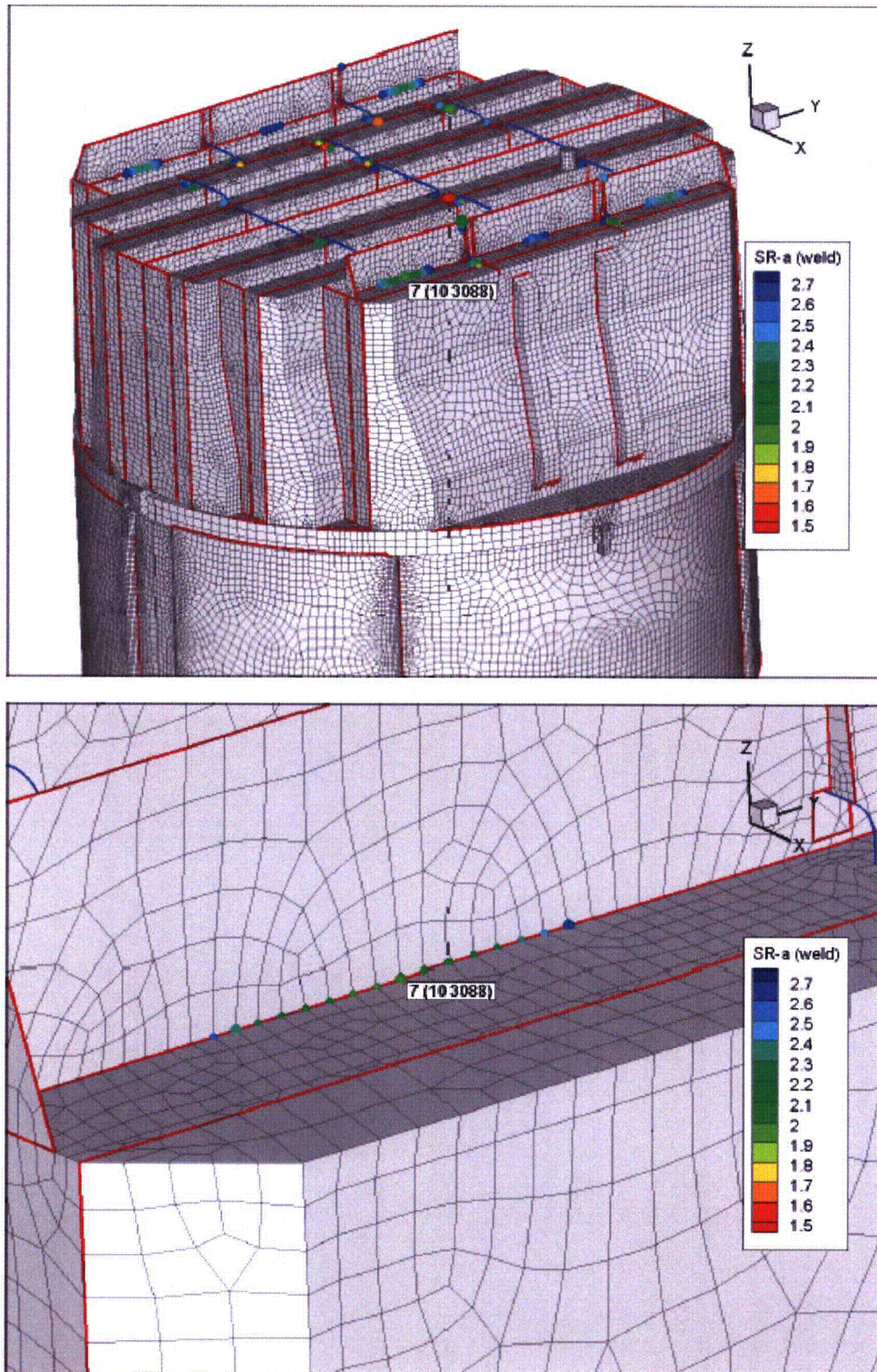


Figure EMCB.170/138-6: Node 103088

NON-PROPRIETARY INFORMATION

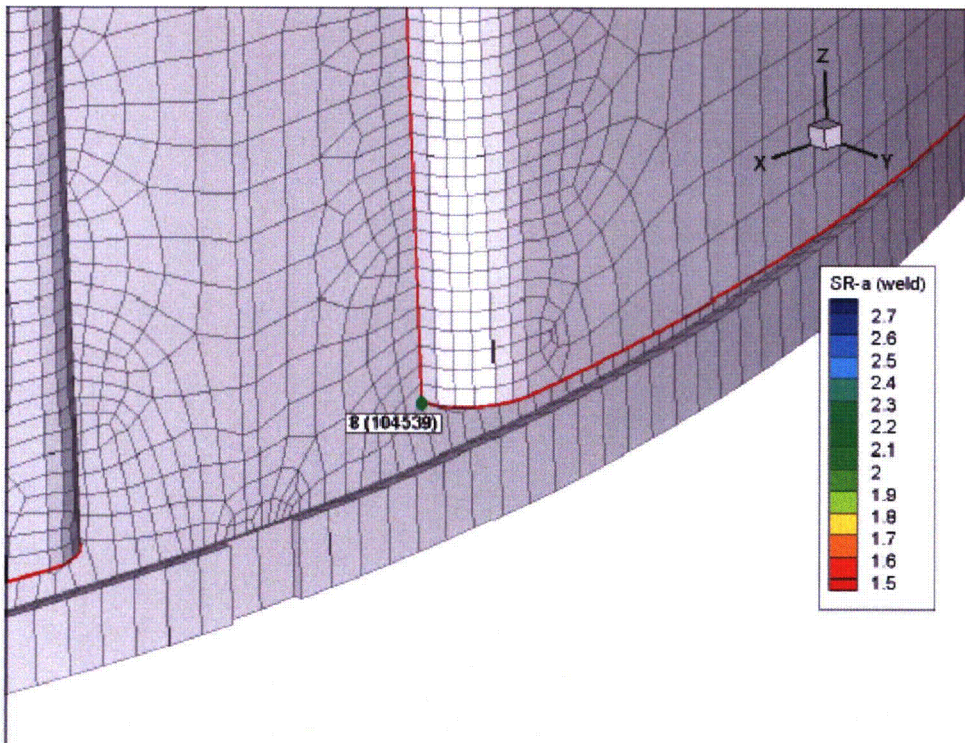
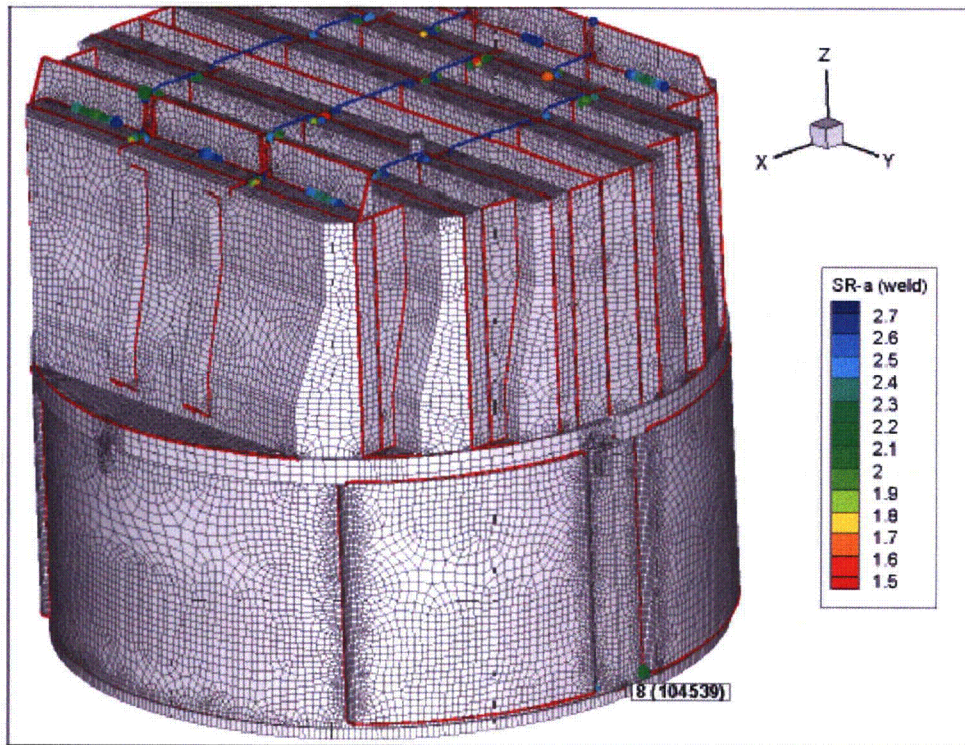


Figure EMCB.170/138-7: Node 104539

NON-PROPRIETARY INFORMATION

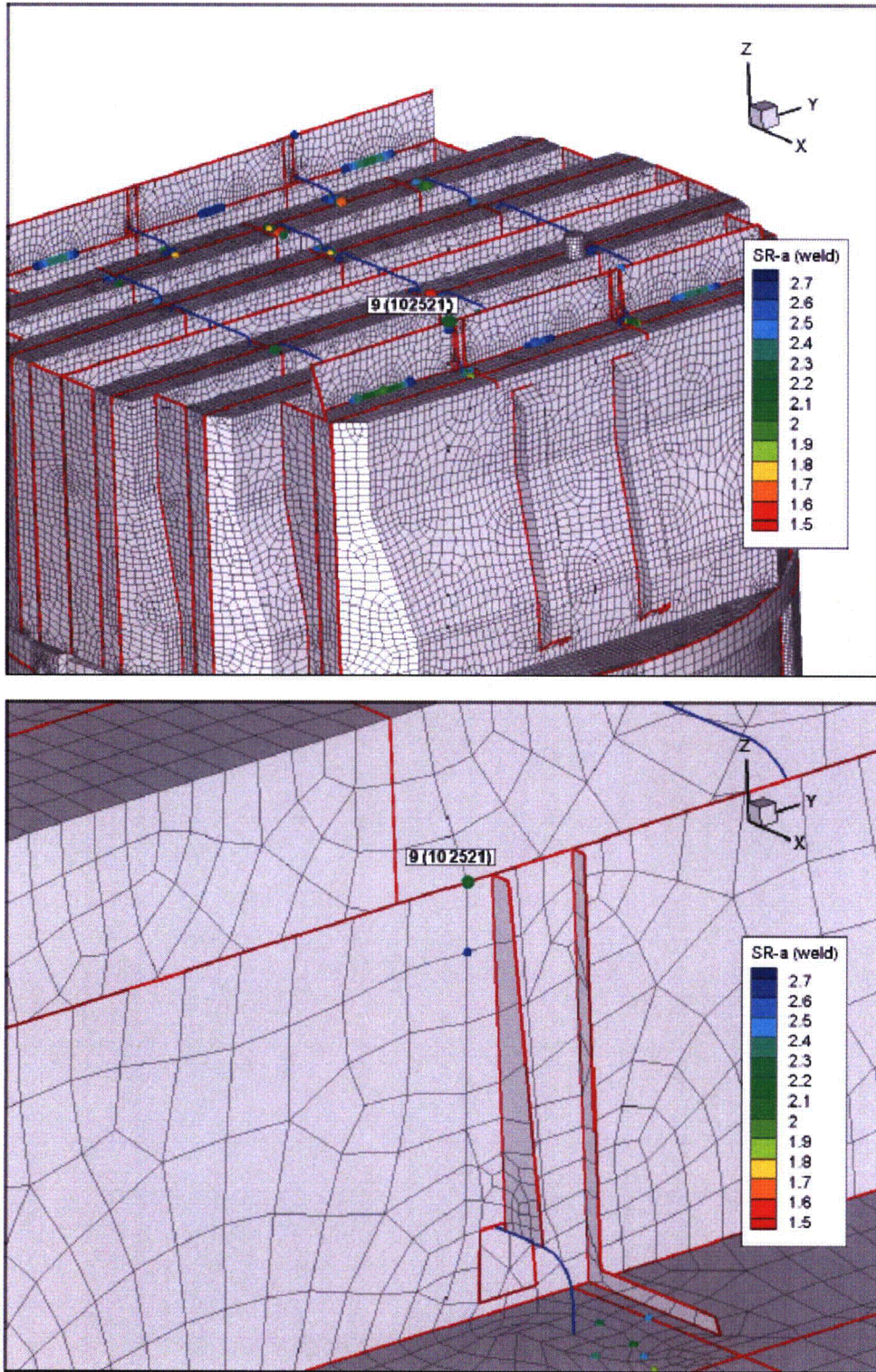


Figure EMCB.170/138-8: Node 102521

NON-PROPRIETARY INFORMATION

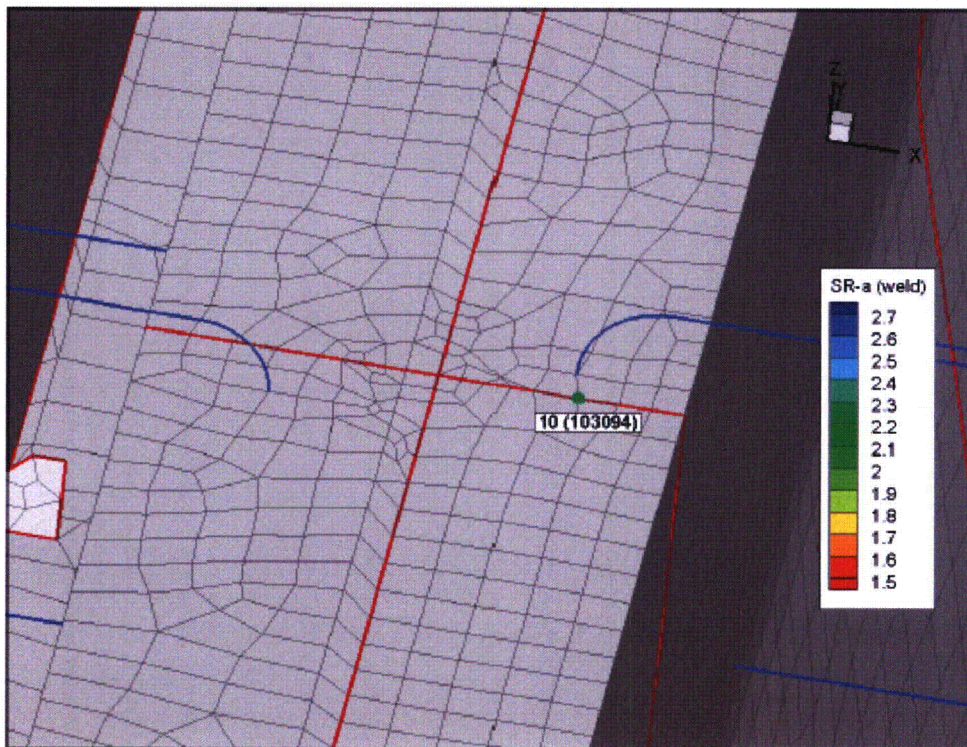
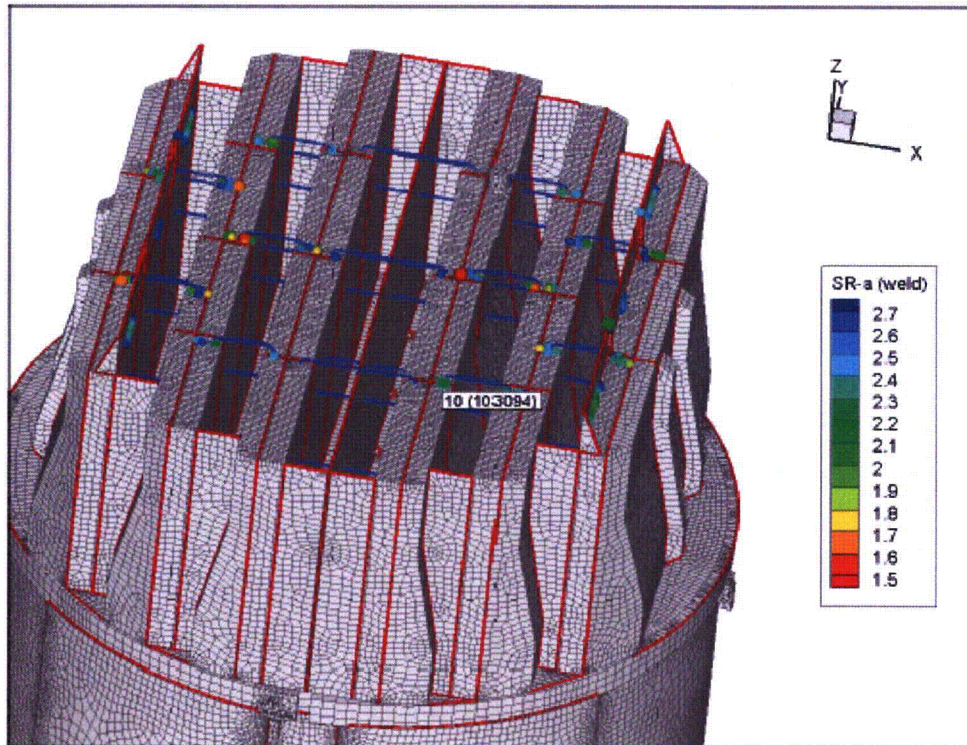


Figure EMCB.170/138-9: Node 103094

NON-PROPRIETARY INFORMATION

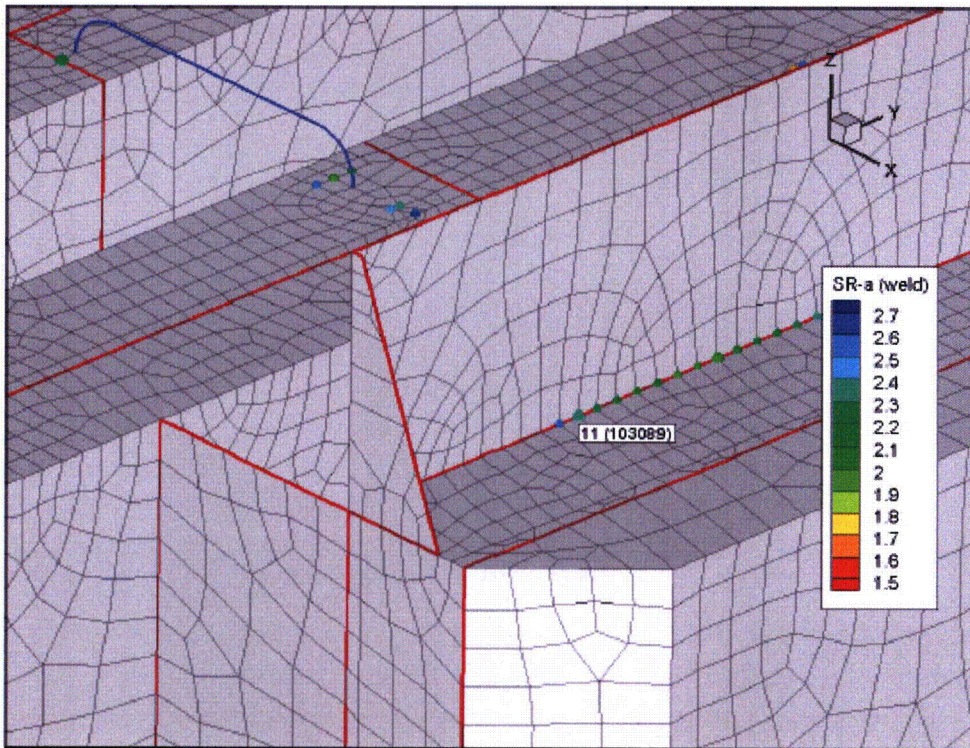
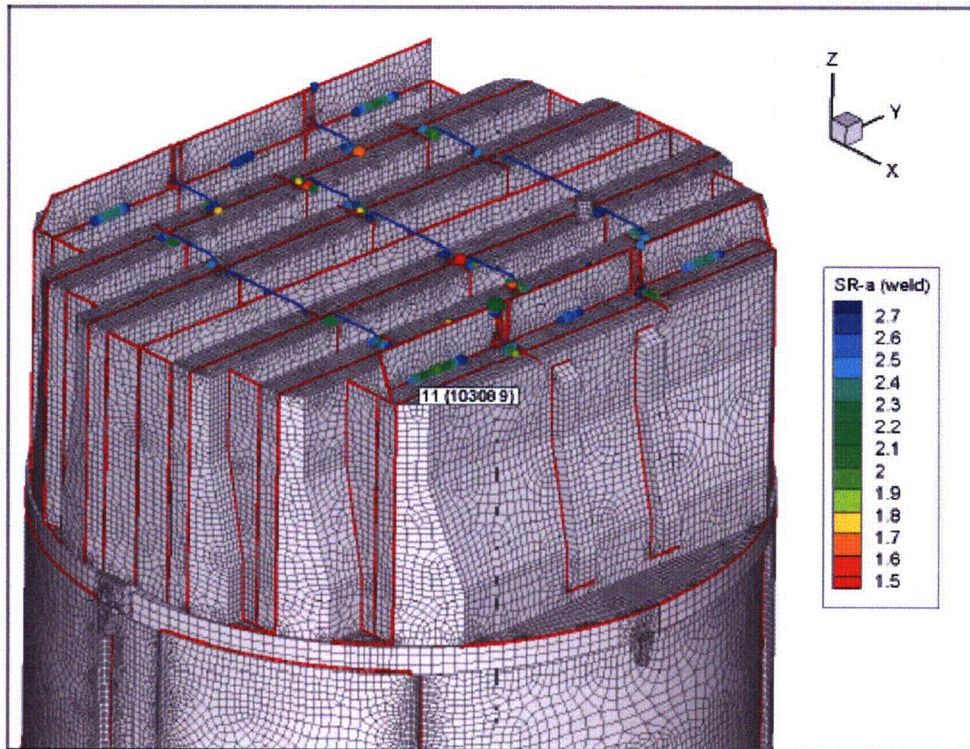


Figure EMCB.170/138-10: Node 103089

NON-PROPRIETARY INFORMATION

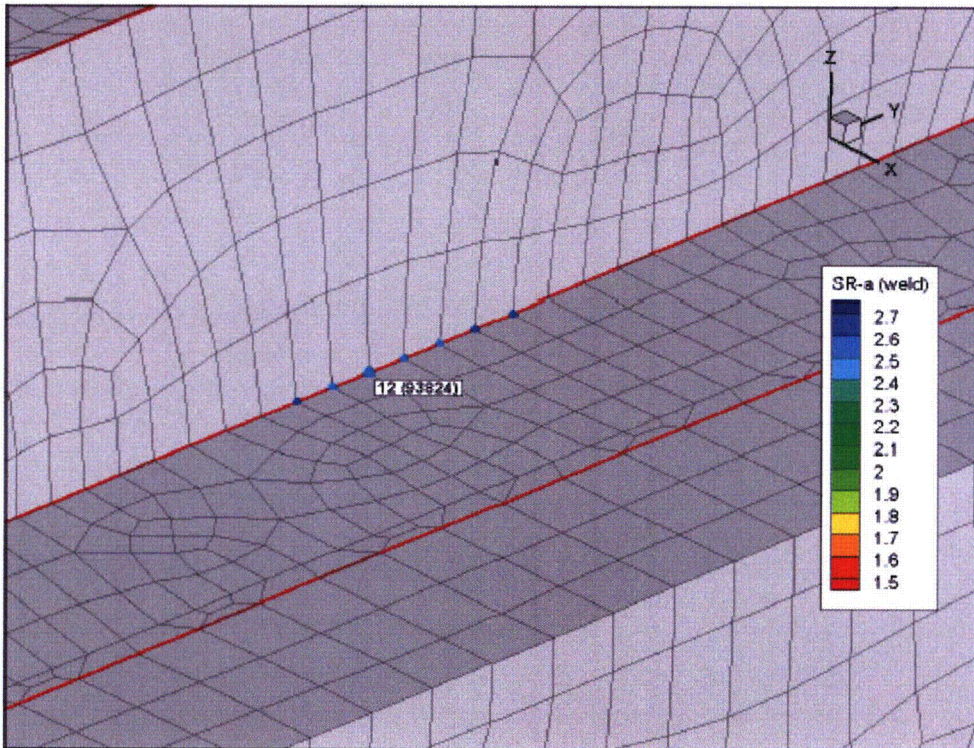
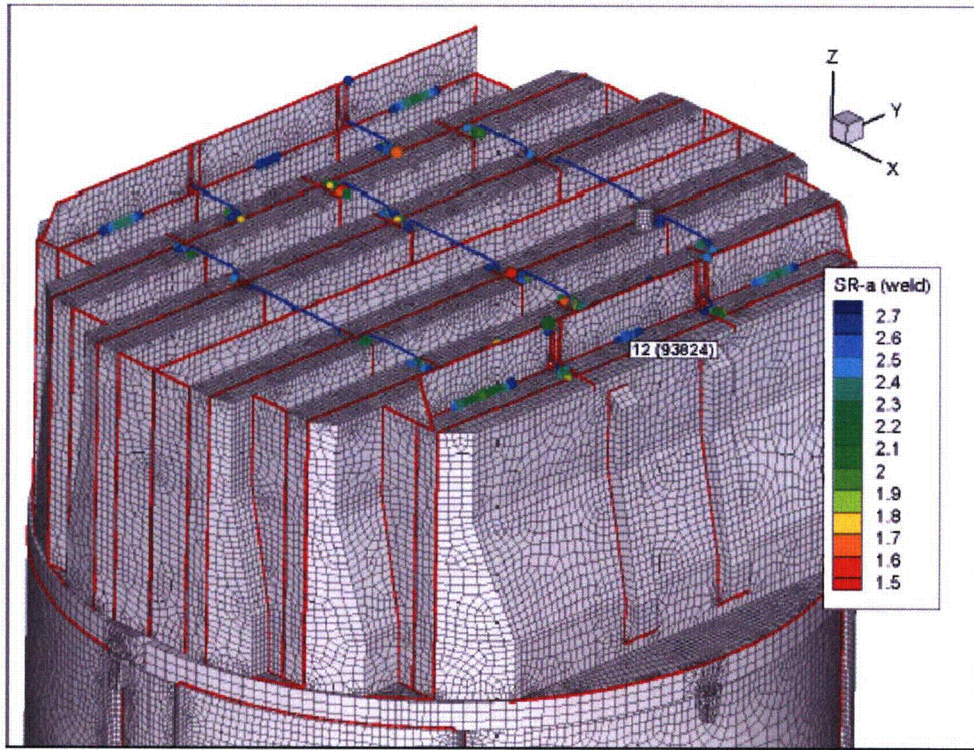


Figure EMCB.170/138-11: Node 93824

NON-PROPRIETARY INFORMATION

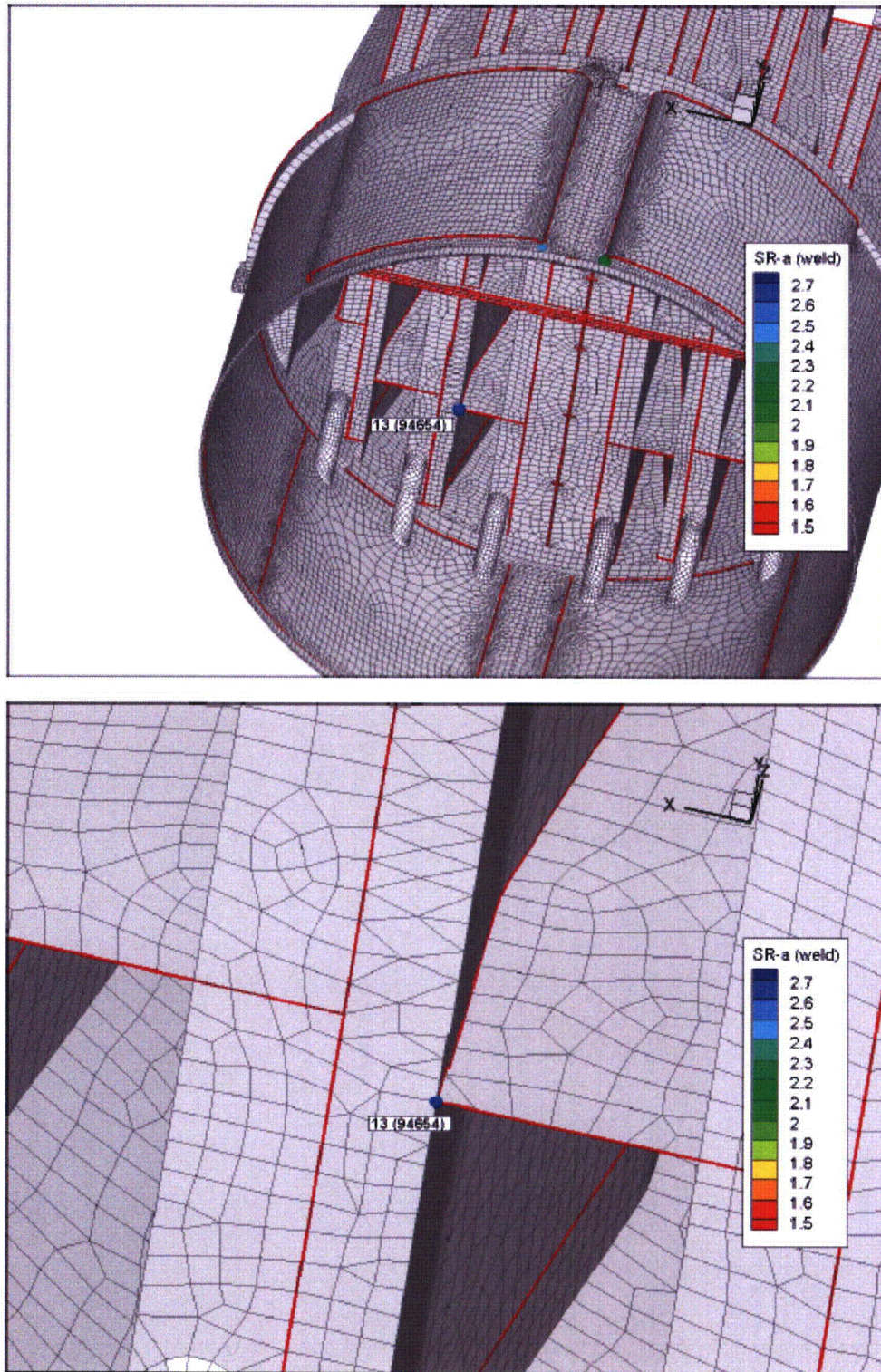


Figure EMCB.170/138-12: Node 94654

NON-PROPRIETARY INFORMATION

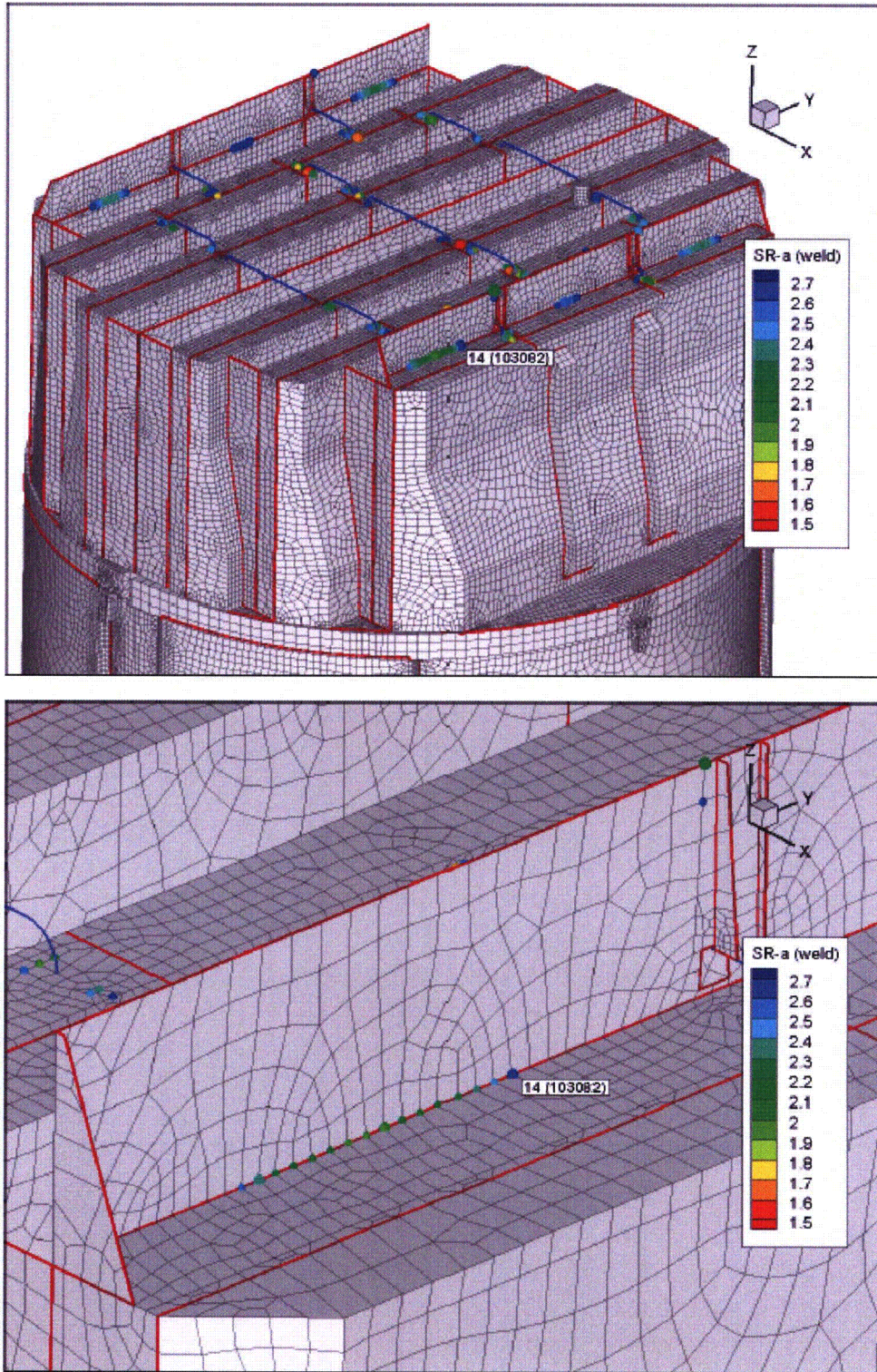


Figure EMCB.170/138-13: Node 103082

NON-PROPRIETARY INFORMATION

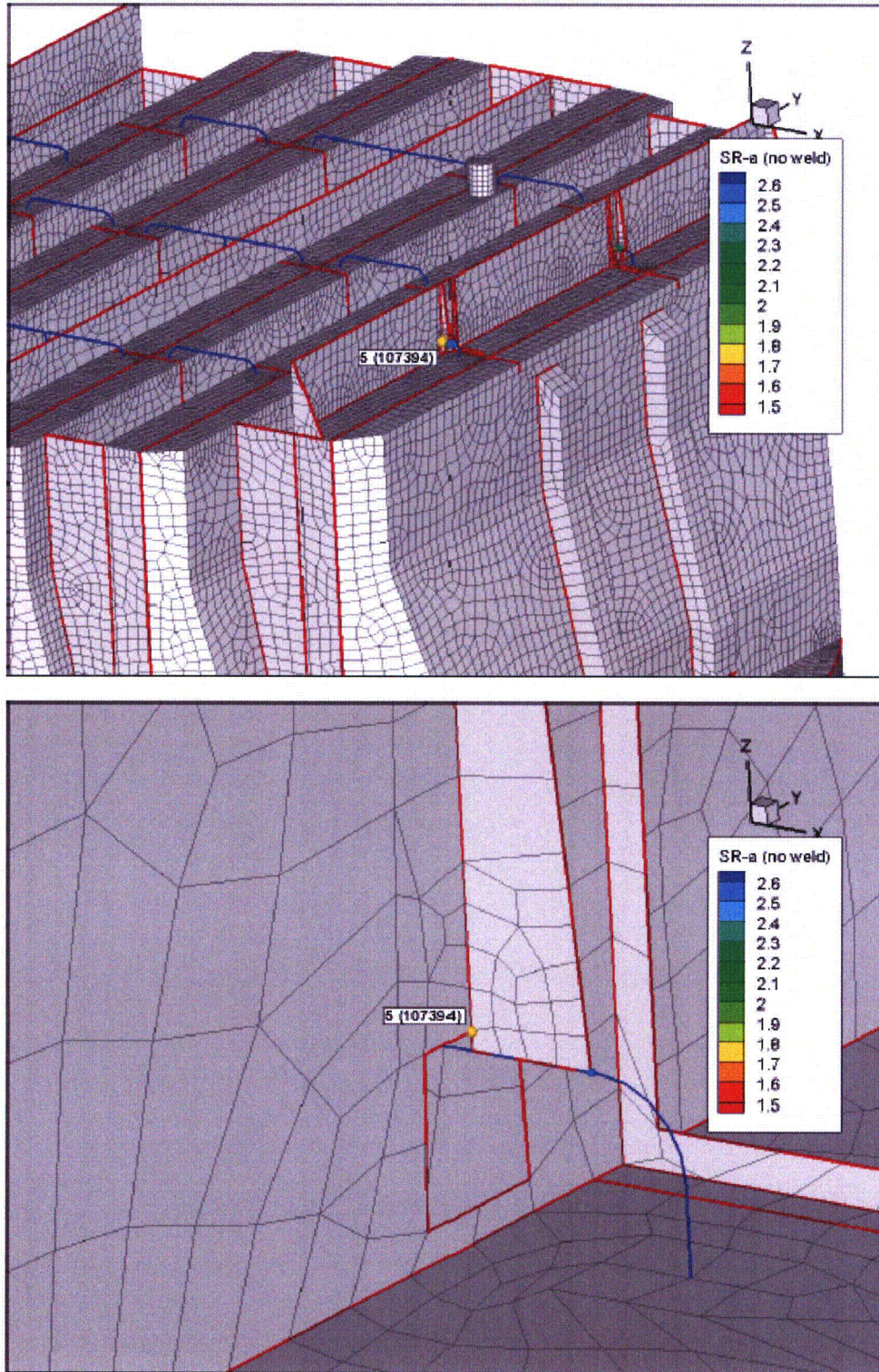


Figure EMC.B.170/138-14: Node 107394

NON-PROPRIETARY INFORMATION

- (b) According to the ASME code, the alternating stress intensity is defined as a peak-to-peak stress in the time domain and, as such, does not have a well-defined frequency-dependence. Specifically, the alternating stress intensity is obtained by considering the difference between every possible pair of stress tensors, $\Delta\sigma_{ij} = \sigma_i - \sigma_j$ at two different times, t_i and t_j and calculating the stress intensity, S_{ij} , for $\Delta\sigma_{ij}$ (i.e., the difference between the maximum and minimum eigenvalues of this tensor). The alternating stress intensity is then defined as one half times the maximum S_{ij} obtained over all possible pairs, i and j . Because the maximum operation is nonlinear, there is no simple way to relate the stress intensities of the stress tensor frequency components to an alternating stress intensity. Hence, no definition of an "accumulative PSD" for a stress intensity appears to be available. We give a plausible definition below, however, and report results using this definition.

First, it is important to emphasize the purpose and usage of the accumulative PSD curves as used in CDI's reports and previous RAI responses. The primary role is to identify the frequencies where significant stress contributions occur. This information can be obtained by examining PSDs or accumulative PSD curves of any stress component since the generally strong response in one stress component at a given frequency will be mirrored in the other components also due to the 3D coupling between stresses. Identifying the dominant frequencies is useful for both diagnostic work (e.g., determining whether the acoustic loading contains a strong component at the given frequency; inferring damping estimates from the PSD curve in cases with well-separated modes) and corrective design (e.g., limiting initial design analysis to a given frequency range). The PSD and accumulative PSD curves are of more limited value, however, for quantitative stress estimates. For example, it is possible that a frequency shift will increase the alternating stress intensity while reducing the accumulative PSD level. This typically occurs when the stress response exhibits one or a small number of localized peaks so that the peak-to-peak response increases, but the root mean square (RMS) average of the amplitudes shows a much smaller increase. In fact, it is easy to see that the peak-to-peak variation in a stress component will always be larger than the RMS amplitude since for any set of amplitudes, a_i with $i=1$ to N :

$$\max\{a_i\} \geq \sqrt{\frac{1}{N} \sum_i a_i^2}$$

This explains why the accumulative PSD stresses reported for a stress component are generally significantly lower than the reported alternating stress intensities at the same node.

To respond to the RAI, we define an accumulative alternating stress intensity, $\Sigma_a(f)$, as the alternating stress computed when zeroing all stress harmonics for frequencies above f . This can be programmed by inserting the current routine used to calculate the alternating stress inside a loop where the cutoff frequency is reduced from $f=250$ Hz to $f=0$ Hz in 5Hz decrements. In the first iteration the stress components are computed in the normal manner and the alternating stress calculated. In subsequent iterations, the stresses above the current cutoff frequency are zeroed and the alternating stress recomputed by computing the stress time history via inverse Fast Fourier transform (FFT) and applying the alternating stress algorithm to this history. The 5Hz increment is coarser than the frequency resolution afforded by standard PSDs and accumulative PSD curves. However, reducing the frequency increment to smaller values increases calculation times - processing four nodes at 0.01 Hz intervals would involve the same

NON-PROPRIETARY INFORMATION

calculation time as a complete steam dryer evaluation. The PSD and accumulative PSD curves of individual stress components, therefore, afford higher resolution of frequency peaks with minimal computational effort.

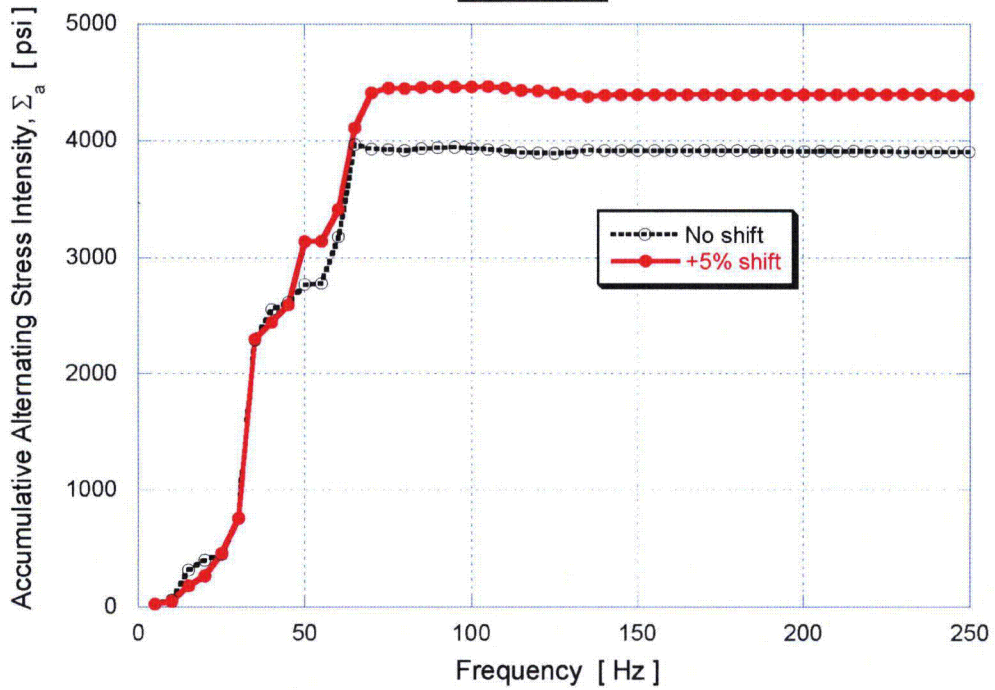
Using the definition of accumulative alternating stress intensity $\Sigma_a(f)$ above, one can plot the dependence of $\Sigma_a(f)$ upon frequency, f for the first ten nodes listed in Table EMCB.170/138-1. These are shown in Figures EMCB.170/138-1a through 1e.

Modal analysis was performed on the BFN Unit 1 steam dryer model using the ANSYS QR damped modal extraction algorithm. The frequency ranges examined were 33.5 - 34.5 Hz, 46 - 48 Hz and 61 - 63 Hz. Each range contained modes with low hydrodynamic damping where the perforated plate hydrodynamic damping ratio, $\zeta_{pp} < 1\%$, and modes with moderate hydrodynamic damping ($3\% < \zeta_{pp} < 10\%$). These damping ratios are determined by taking the ratios between the real and imaginary parts of the computed complex eigenvalues. In the following plots, the IFRQ is the imaginary part of the eigenvalue and corresponds to the steady-state frequency, whereas RFRQ is the real part and contains the decay coefficient. The damping ratio is then given by: $\zeta_{pp} = |RFRQ/IFRQ|$.

The contour plots below show the real parts of the displacement eigenvector for several modes in each frequency range. In general, lightly damped modes involve structural parts other than perforated plates while moderately damped modes involve higher participation by the perforated plates. As there are up to 30 modes per frequency range, only the most significant representative modes involving perforated plate motion are shown. Note that because of the nearly two-fold symmetry in the steam dryer structure (the planes of symmetry corresponding to the 0°-180° and 90°-270° lines) each mode shape shown below tends to have three reflected counterparts at the same frequency. Four distinct mode shapes, two with low and two with moderate hydrodynamic damping, are shown for each frequency range: Figure EMCB.170/138-2 (frequencies about 34 Hz); Figure EMCB.170/138-3 (frequencies about 47 Hz) and; Figure EMCB.170/138-4 (frequencies about 62 Hz).

NON-PROPRIETARY INFORMATION

Node 88059



Node 107054

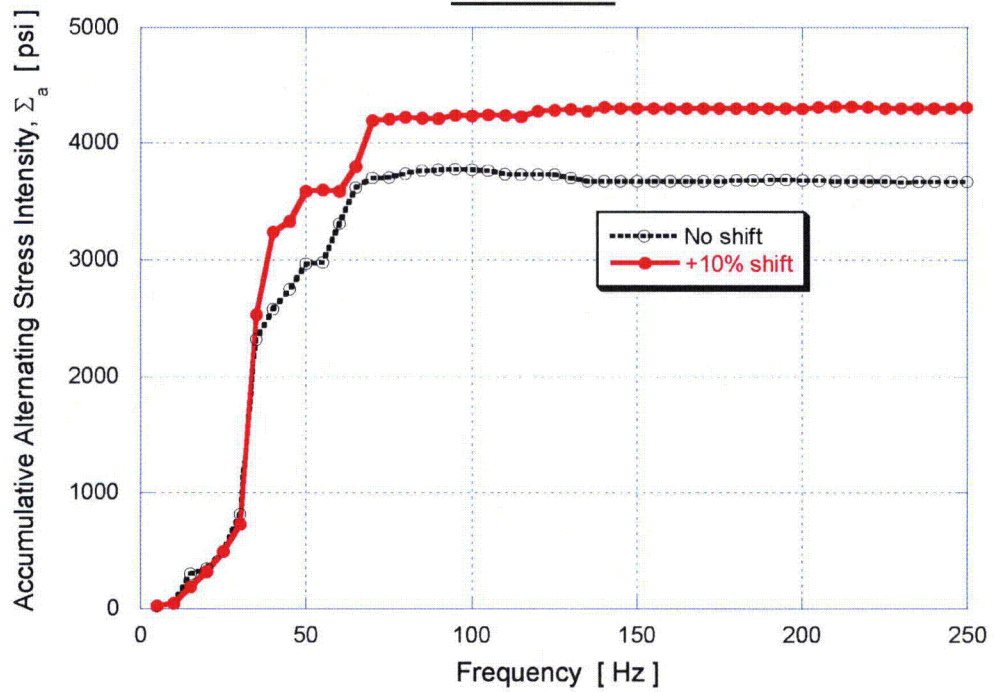
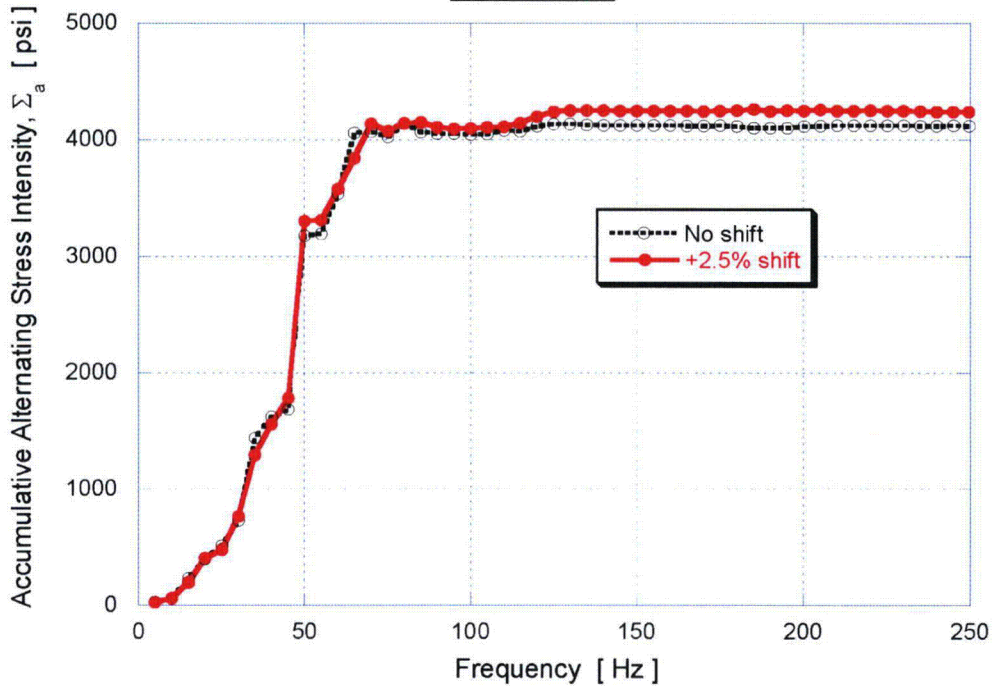


Figure EMCB.170/138-1a: Accumulative alternating stress intensity curves for nodes 88,059 and 107,054

NON-PROPRIETARY INFORMATION

Node 102407



Node 91420

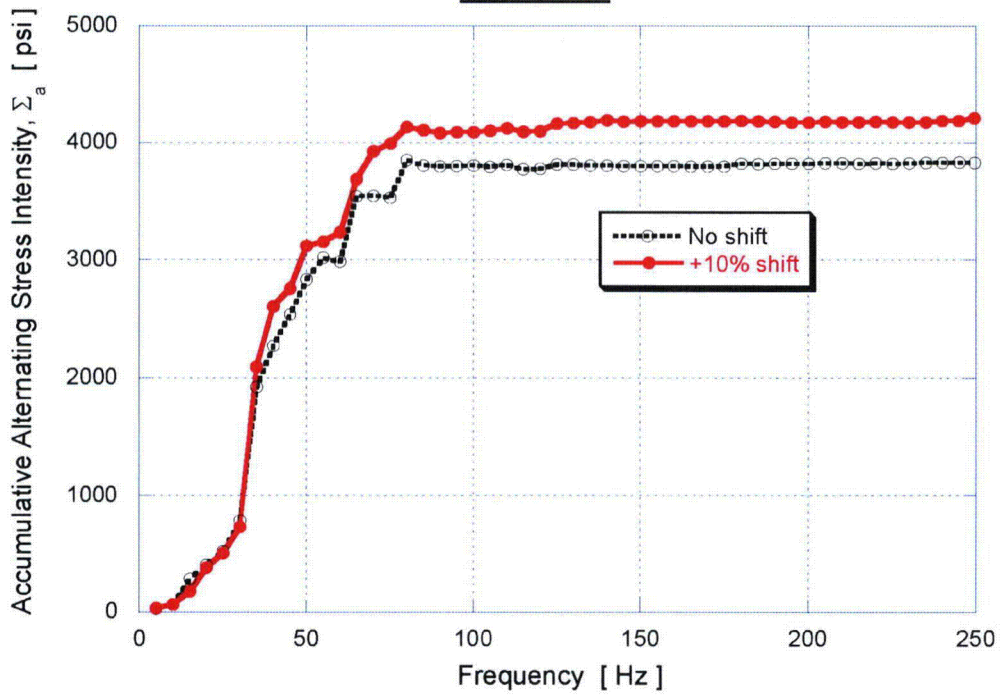
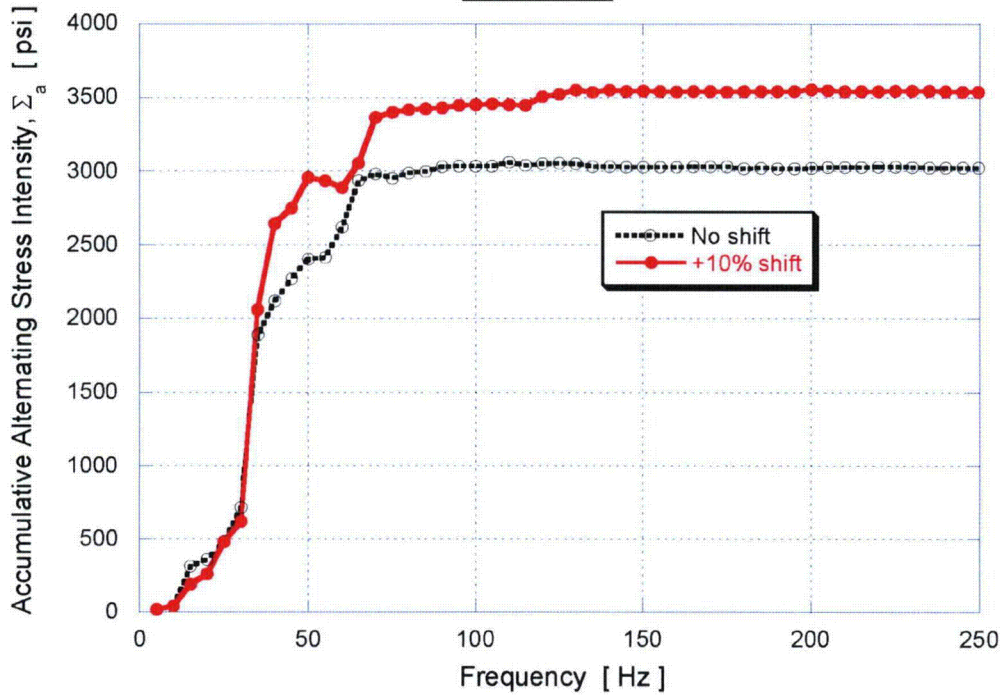


Figure EMCB.170/138-1b: Accumulative alternating stress intensity curves for nodes 102,407 and 91,420

NON-PROPRIETARY INFORMATION

Node 96561



Node 103088

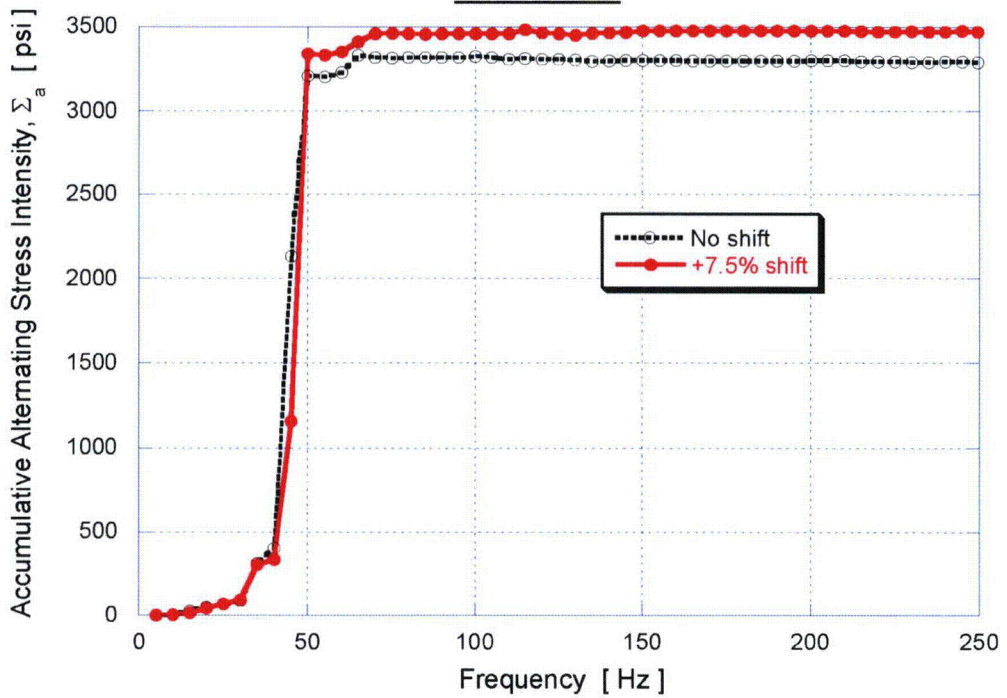
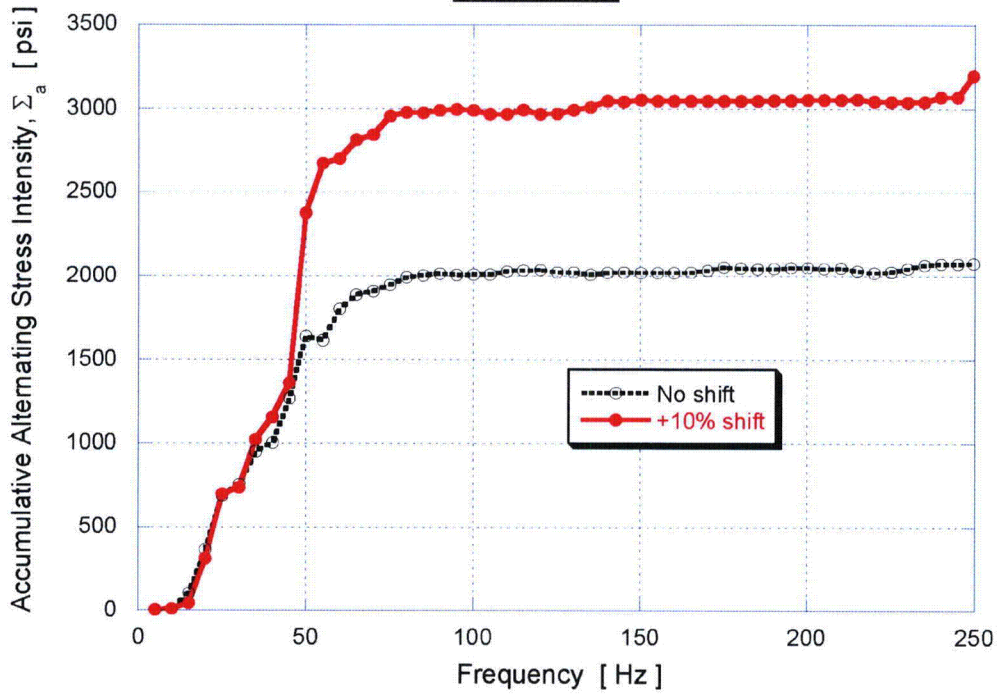


Figure EMCB.170/138-1c: Accumulative alternating stress intensity curves for nodes 96,561 and 103,088

NON-PROPRIETARY INFORMATION

Node 104539



Node 102521

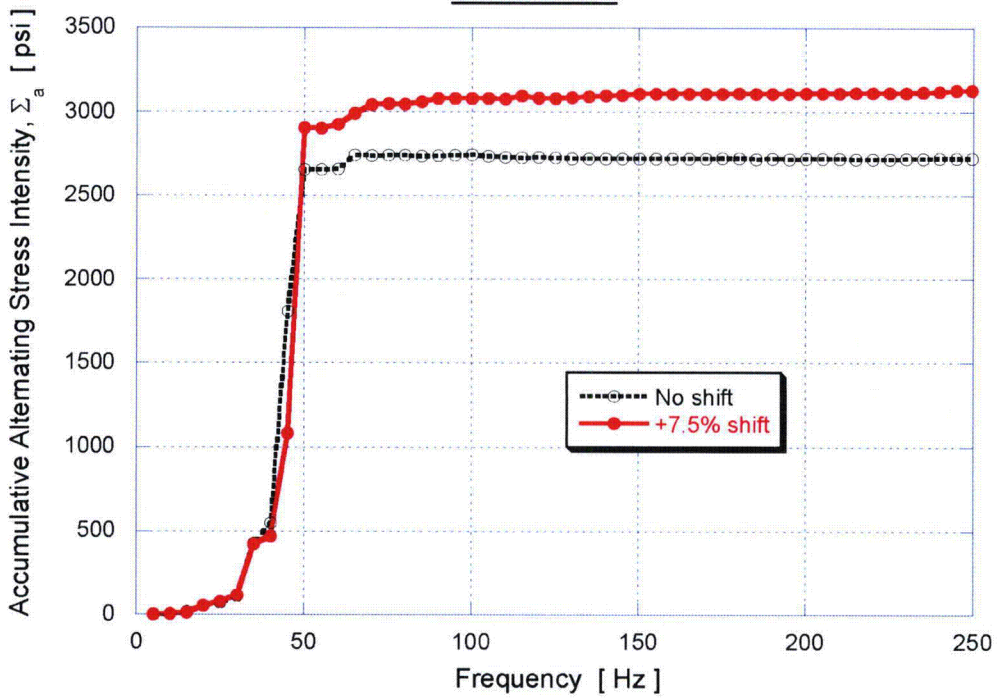
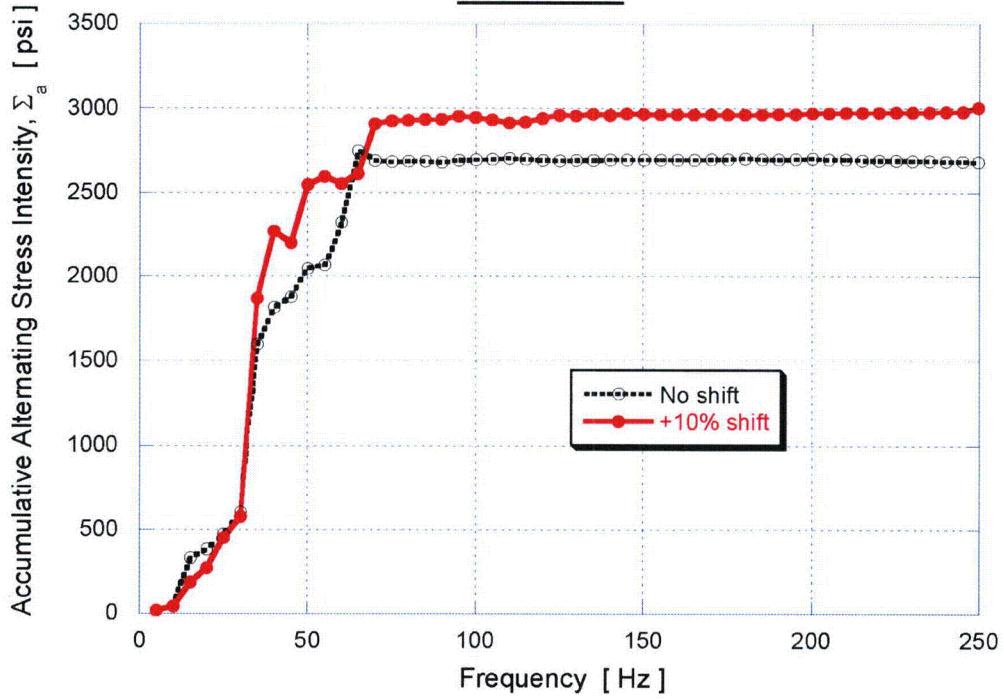


Figure EMCB.170/138-1d: Accumulative alternating stress intensity curves for nodes 104,539 and 102,521

NON-PROPRIETARY INFORMATION

Node 103094



Node 103089

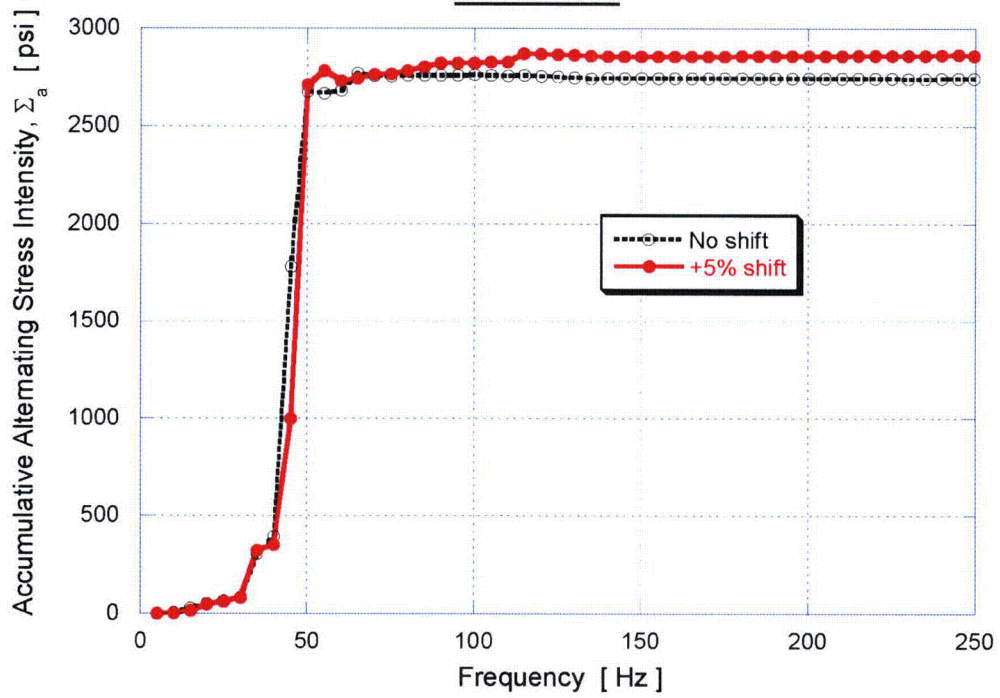
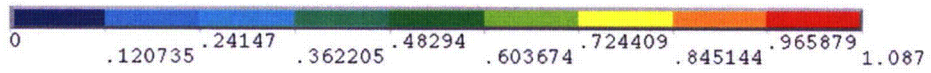


Figure EMCB.170/138-1e: Accumulative alternating stress intensity curves for nodes 103,094 and 103,089

NON-PROPRIETARY INFORMATION

STEP=1
SUB =6
RFRQ=-.176E-03
IFRQ=34.021
MODE Real part
USUM (AVG)
RSYS=0
DMX =1.087
SMX =1.087



STEP=1
SUB =7
RFRQ=-.001888
IFRQ=34.043
MODE Real part
USUM (AVG)
RSYS=0
DMX =1.07
SMX =1.07

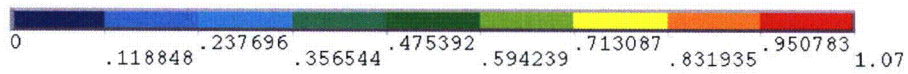


Figure EMCB.170/138-2a: Lightly damped skirt modes at 34.021 and 34.043 Hz.
Damping ratio $\zeta_{pp} < 1\%$.

NON-PROPRIETARY INFORMATION

STEP=1
SUB =8
RFRQ=-2.49
IFRQ=34.03
MODE Real part
USUM (AVG)
RSYS=0
DMX =1
SMX =1

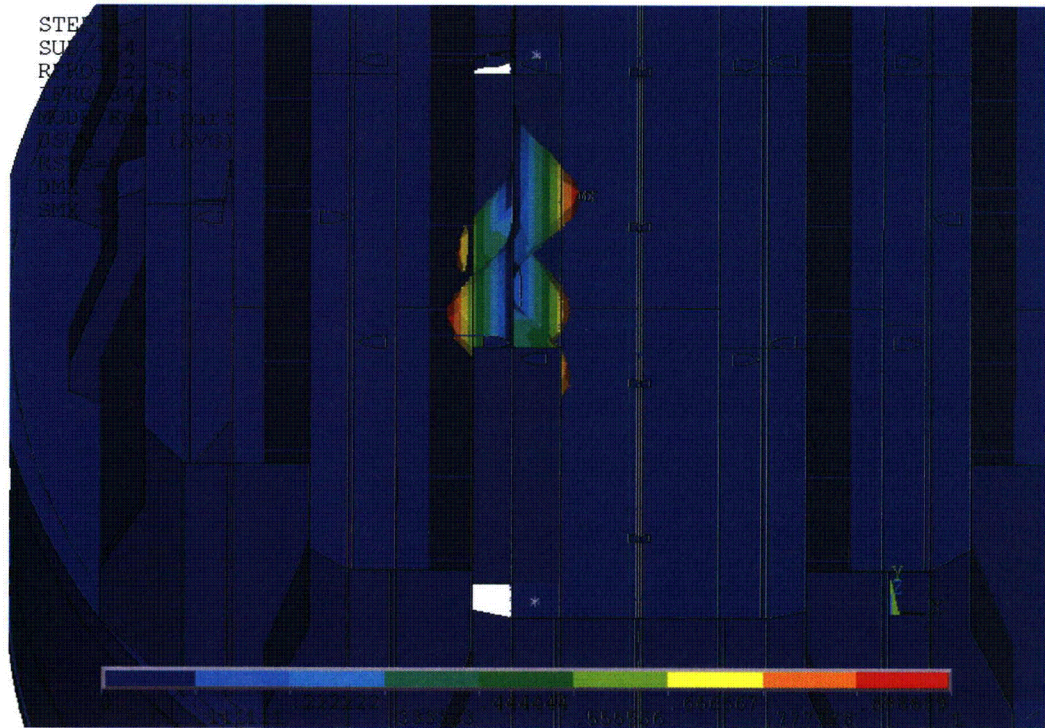
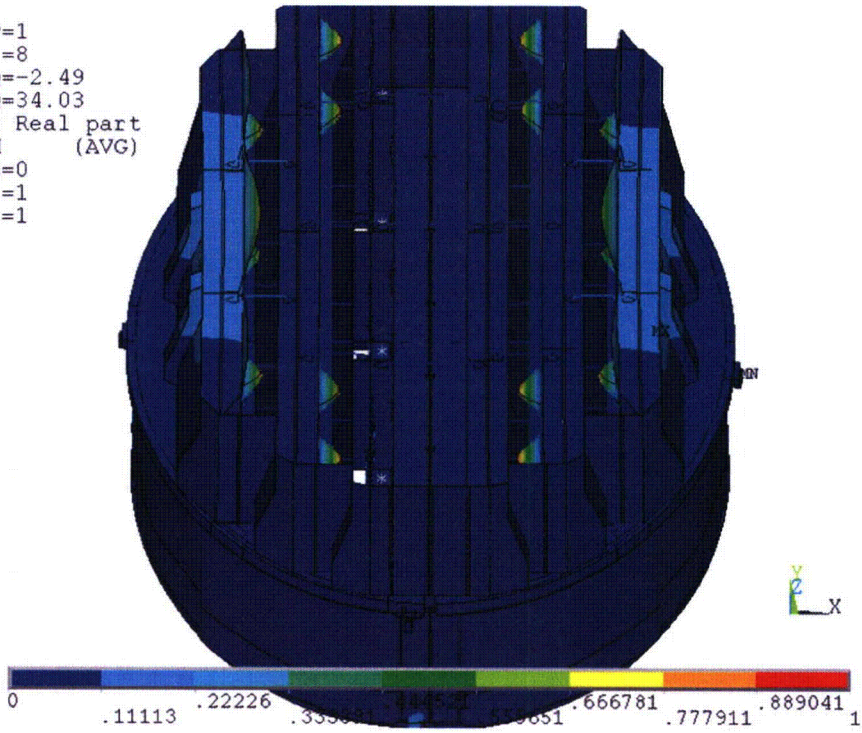
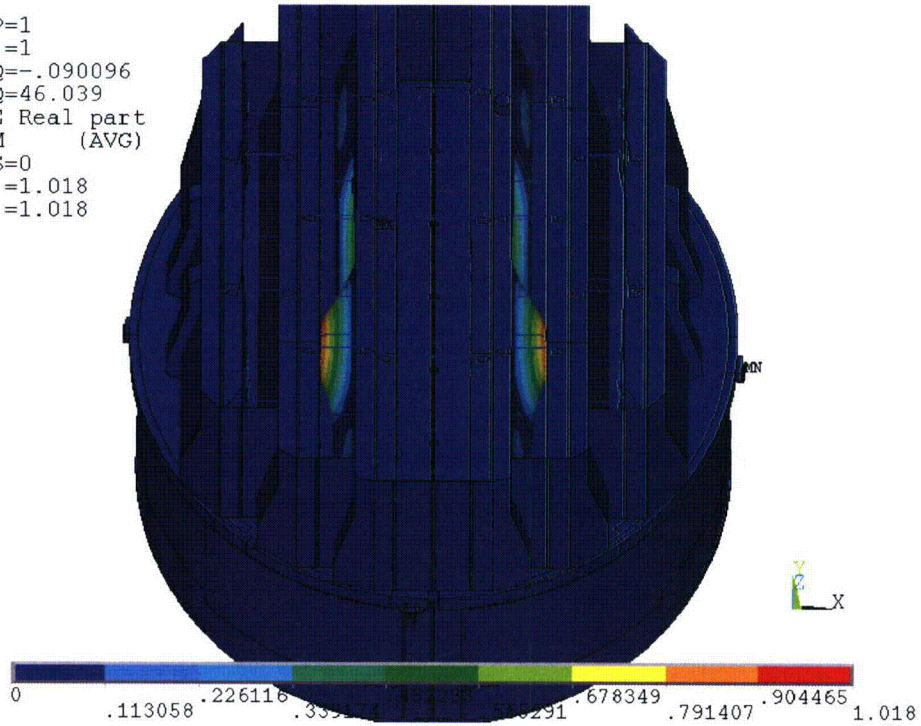


Figure EMCB.170/138-2b: Moderately damped modes at 34.03 and 34.36 Hz. Damping ratio, $\zeta_{pp} > 3\%$. On the bottom plot the top cover plate elements are removed for clarity

NON-PROPRIETARY INFORMATION

STEP=1
SUB =1
RFRQ=-.090096
IFRQ=46.039
MODE Real part
USUM (AVG)
RSYS=0
DMX =1.018
SMX =1.018



NODAL SOLUTION

STEP=1
SUB =2
RFRQ=-.219449
IFRQ=46.095
MODE Real part
USUM (AVG)
RSYS=0
DMX =1.018
SMX =1.018

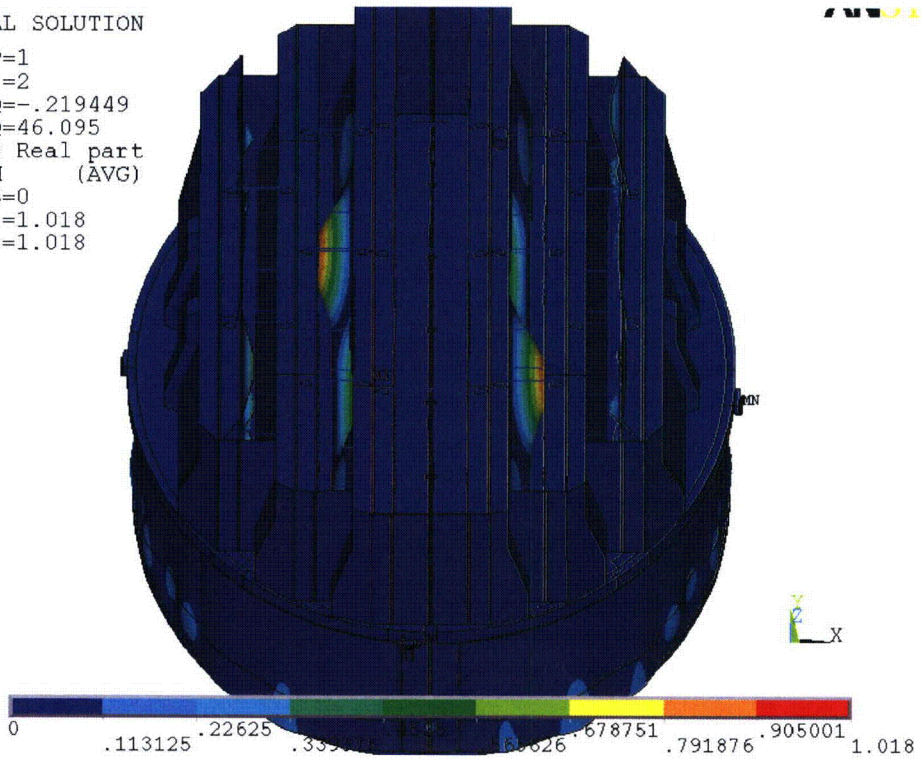


Figure EMCB.170/138-3a: Lightly damped hood modes at 46.039 and 46.095 Hz.
Damping ratio <1%

NON-PROPRIETARY INFORMATION

SUB =24
RFRQ=-3.424
IFRQ=47.043
MODE Real part
USUM (AVG)
RSYS=0
DMX =1
SMX =1

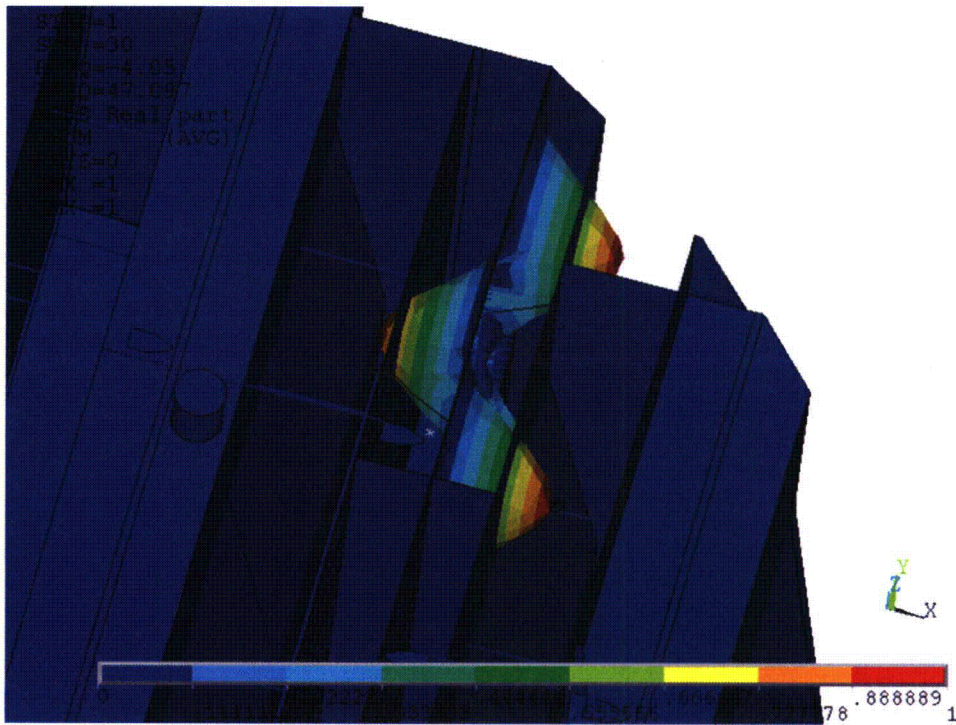
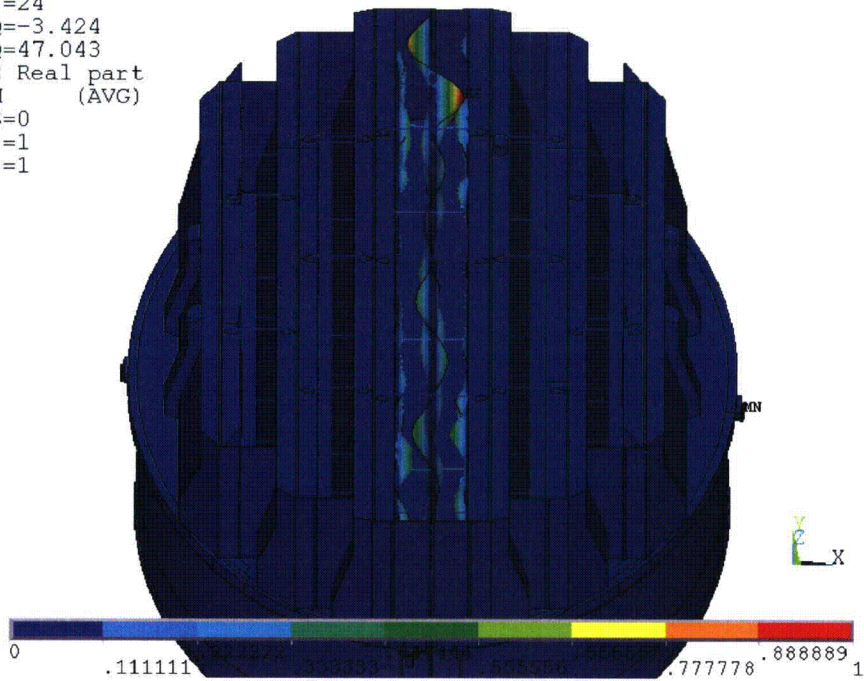
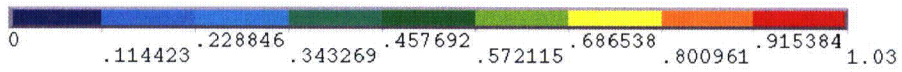


Figure EMCB.170/138-3b: Moderately damped modes at 47.043 and 47.097 Hz. Damping ratio $\zeta_{pp} > 3\%$. On the bottom plot the top cover plate elements are removed for clarity

NON-PROPRIETARY INFORMATION

```
SUB =4  
RFRQ=-.101673  
IFRQ=61.112  
MODE Real part  
USUM (AVG)  
RSYS=0  
DMX =1.03  
SMX =1.03
```



ANSYS

NODAL SOLUTION

```
STEP=1  
SUB =23  
RFRQ=-.590066  
IFRQ=61.686  
MODE Real part  
USUM (AVG)  
RSYS=0  
DMX =1.017  
SMX =1.017
```

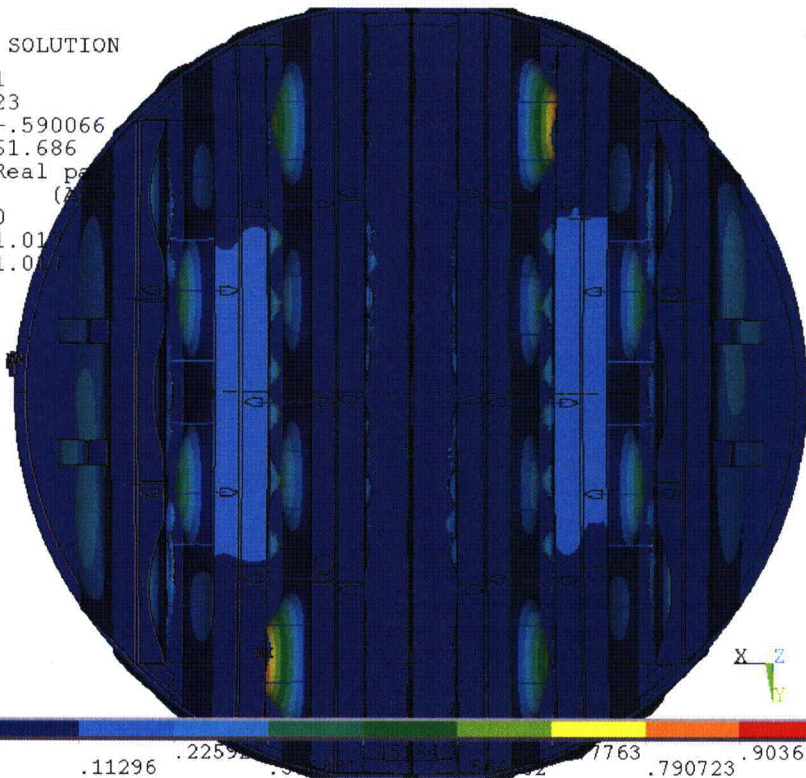


Figure EMCB.170/138-4a: Lightly damped modes at 61.112 and 61.686 Hz.
Damping ratio $\zeta_{pp} < 1\%$

NON-PROPRIETARY INFORMATION



NODAL SOLUTION

STEP=1
SUB =25
RFRQ=-1.768
IFRQ=61.699
MODE Real part
USUM (A) $\times 10^{-4}$
RSYS=0
DMX =1
SMX =1

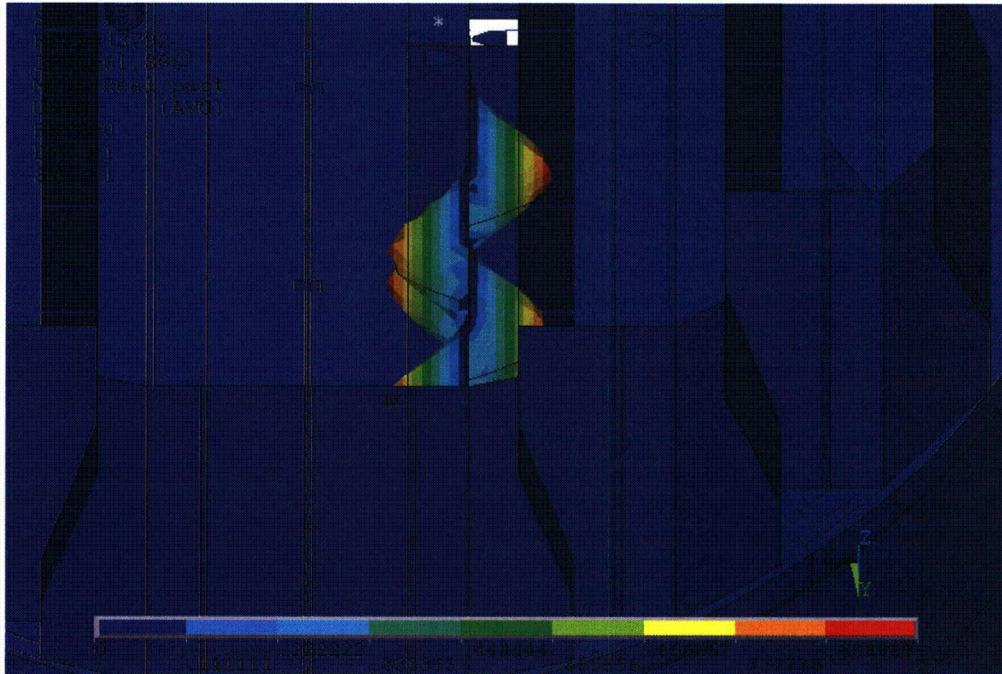
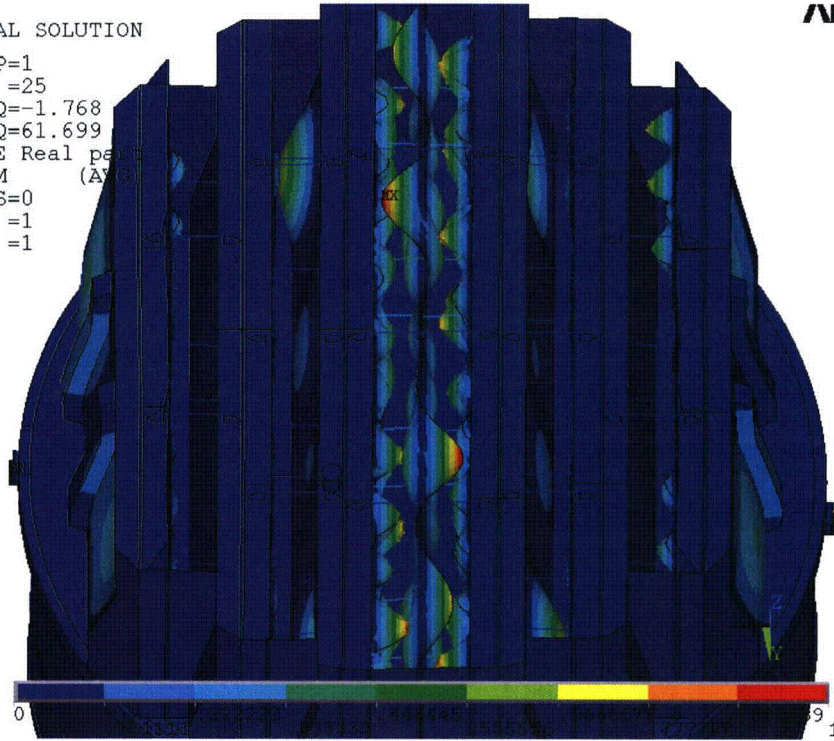


Figure EMCB.170/138-4b: Moderately damped modes at 61.699 and 61.888 Hz. Damping ratio $\zeta_{pp} > 2\%$. On the bottom plot the top cover plate elements are removed for clarity

NON-PROPRIETARY INFORMATION

NRC RAI EMCB.171/139

Expand the table in the response to EMCB 139/106-2 to include frequencies near 47 and 62 Hz. Also, explain why the stress ratio decreases from 2.00 to only 1.77 at node 76,452 (inner hood top cover plate/tie bar) in Tables EMCB 139/106-3 and 106-4, when Table EMCB 139/106-2 and Figure EMCB 139/106-2a show that the dominant 34 Hz peak stress decreases by 42 percent. Discuss what contributes to the major portion of stress near 34, 47 and 62 Hz frequencies to the peak alternating stresses at Node 76,452.

TVA Response to EMCB.171/139

The table focused mainly on the 34 Hz mode because it had the most isolated peak. Inferring damping ratios by comparing peaks or using 1/2-power bandwidth estimates is only strictly valid for a single degree-of-freedom system. It can also be used in a multi degree-of-freedom system for modes that are well separated, but the accuracy of the approach will deteriorate when other modes are present at nearby frequencies. For this dryer/load combination, the 34 Hz mode was clearly dominant and the response peak sufficiently resembled that of a single degree-of-freedom system, so that reasonable estimates of damping ratios could be obtained. This was not the case for the other two frequencies – 47 Hz and 62 Hz – so these were omitted.

Below (Figure EMCB.171/139-1) are close-up depictions of the PSD peaks in the vicinity of the 47 and 62 Hz peaks for the same nodes selected in Table EMCB.139/106-2. These show that the peaks involve multiple modes. Moreover, in a small number of instances, increasing the damping actually increases the peak which is physically compatible with a displacement-driven modal response. In light of these results we strongly caution that estimating damping ratios from these curves by comparing peaks or using the 1/2 power formula is subject to gross error. With this warning in mind, Table EMCB.171/139-1 is provided to be responsive to the RAI. For the 47 Hz peak, the damping estimates are made using nodes 76452 and 84412 since these have the highest peaks. For the latter result, the 48 Hz peak is used and the second mode at 47 Hz is ignored. The same nodes are used to estimate the damping at 62 Hz. In this case, the response for node 76452 shows two strong peaks indicating that the rise in the accumulative PSD about 62 Hz is due to the summed contribution of the peaks at 61.5 Hz and 64.2 Hz. The damping is estimated from the higher frequency peak.

There are several reasons why the stress ratio at node 76452 can decrease from 2.00 to 1.77 (a 12% increase in stress) whereas the dominant 34 Hz peak stress changes by 42%. (a) The 42% reduction (with damping included) pertains to the PSD peak which represents stress *squared* rather than stress amplitude. The corresponding change in stress amplitude is only $(1.42)^{1/2} - 1 = 19.2\%$ as indicated in Table EMCB 139/106-2. (b) Utilizing single-degree-of-freedom techniques to extract damping for a system that contains multiple modes incurs error as discussed above. This is why even for the dominant mode, the estimated change in damping obtained by comparing peaks (19%) differs from that obtained from the half-power rule (14% - which is very close to the 12% change in stress inferred from Tables EMCB.139/106-3 and 4). (c) There are other peaks in the 0-250 Hz range which, though not dominant, still contribute to the complete stress state at the node. (d) As discussed in the response to RAI EMCB.170/138 in this submittal, the stress intensity used to calculate stress ratios is a nonlinear function of the six stress component time histories. While qualitative comparisons between the stress intensities and any stress component can be made, considerable caution is due when seeking quantitative comparisons since stress intensity and stress tensor history are different entities. Note too that this node, like the others residing on or near tie bar bases now have significantly lower alternating stresses following the redesign of the tie bars.

NON-PROPRIETARY INFORMATION

For a complex system such as the steam dryer and acoustic circuit model, identifying what mechanism contributes to a given stress peak is not trivial. In general, the stress response depends on three factors: (i) the spectral content of the load and how closely a given peak in the load matches a structural frequency; (ii) how well the acoustic pressure field at a given frequency couples to a structural model (this can be formally quantified for a mode by integrating the product of the mode shape times acoustic pressure field at the modal given frequency, over the structural surface); and (iii) the generalized mass for the mode which effectively relates the modal forcing and response amplitudes. In Figure 15 of CDI Report No. 08-06P, the PSD peaks (34 Hz, 47 and 62 Hz) do not shift when the load frequency is shifted. If the response were dominated by strong peaks in the acoustic signal one would expect the stress PSD peaks to shift with frequency or significantly increase/decrease with frequency shift. Since they do not, the best explanation is that at these frequencies, the structure contains modes that are more easily excited by acoustic loads.

NON-PROPRIETARY INFORMATION

||

||

Figure EMCB.171/139-1a: PSD for σ_{xx} at node 76,452

NON-PROPRIETARY INFORMATION

[[

]]

Figure EMCB.171/139-1b: PSD for σ_{xy} at node 76,949

NON-PROPRIETARY INFORMATION

[[

]]

Figure EMCB.171/139-1c: PSD for σ_{yy} at node 84,412

NON-PROPRIETARY INFORMATION

[[

]]

Figure EMCB.171/139-1d: PSD for σ_{xx} at node 87,364

NON-PROPRIETARY INFORMATION

[[

]]

Figure EMCB.171/139-1e: PSD for σ_{xx} at node 89,175

NON-PROPRIETARY INFORMATION

[[

]]

Table EMCB.171/139-2: Damping ratio estimate using peak response ratios

Location	Frequency, Hz	Peak PSD ratio S_0/S_{damp}	ξ_{damp}/ξ_0 (peak comparison)	ξ_{damp}/ξ_0 (1/2 power method)
Node 76452	47	0.75	0.86	0.32
	64	1.44	1.20	1.13
Node 84412	48	1.10	1.05	1.00
	65	1.24	1.11	0.88

NRC Request EMCB.172 (Unit 1 only)

- (a) Provide the following for Unit 1:
- (i) Plots comparing MSL strain gage PSDs for current licensed thermal power (CLTP) (without low-flow background noise removal), low-flow conditions, and CLTP (with low-flow background noise removal).
 - (ii) Plots similar to those in (a), [[

]]

NON-PROPRIETARY INFORMATION

In the above plots, annotate and discuss any significant reductions in amplitude over broad and narrow frequency ranges, particularly near frequencies associated with high stresses, like 34, 47, and 62 Hz.

- (b) Comparing Tables 9b and 10b in CDI Report No. 08-06P, Rev. 0, dated March 2008, reveals that the alternating stress ratios at several locations in the Unit 1 dryer finite element (FE) model are improved significantly when plant and sensor background noise is removed from the MSL strain gage measurements.

Background noise removal reduces stresses by factors ranging from 1.03 to 1.40, and by an average of 22 percent. Explain how the background noise removal leads to the stress reductions, including which frequencies experience the strongest loading/stress reductions. The explanation should be consistent with the accumulative stress plots provided in the response to EMCB 138/105, which show that stresses are dominated by low frequency peaks at 34, 47, and 62 Hz.

- (c) Describe the modeling simplifications made for the tie bar attachment to the steam dryer and explain why they are conservative.
- (d) Since the strains due to non-acoustic piping structural bending modes will be filtered out by the MSL strain gages, explain how the piping structural modes can cause any other contamination of the strain gage signals.

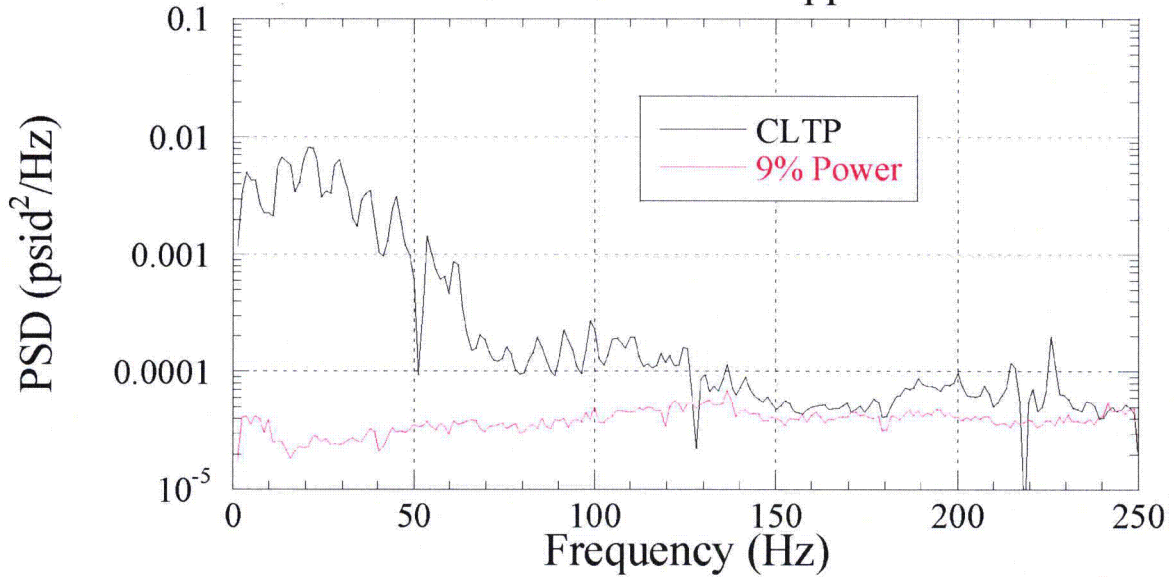
TVA Response to EMCB.172 (Unit 1 only)

The response to this RAI is based upon the analysis presented in CDI Report No. 08-06P Rev. 0, provided in the submittal dated March 6, 2008.

- (a) The following figures are provided.
 - (i) Figures EMCB.172-1 through 4 provide the MSL strain gage PSDs for CLTP (without low-flow background noise removal) and low flow conditions at each of the MSL strain gage locations. Noise is removed at the MSL inlets and not at the MSL strain gage signals. Therefore, a plot of the MSL strain gage PSDs for CLTP (with low-flow background noise removal) does not exist.

NON-PROPRIETARY INFORMATION

BFN1: MSL A Upper



BFN1: MSL A Lower

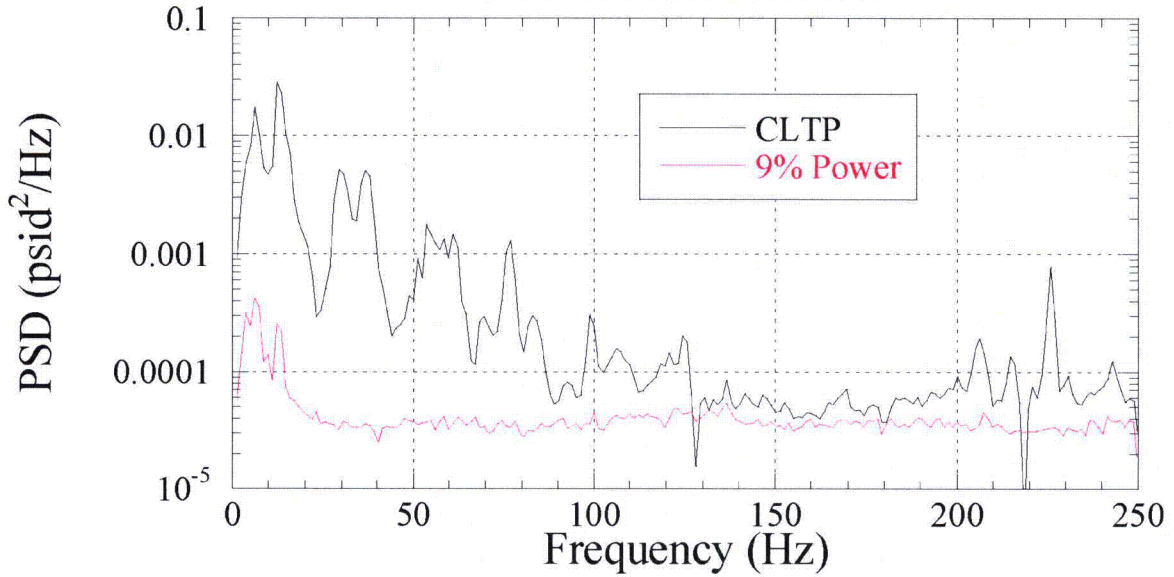
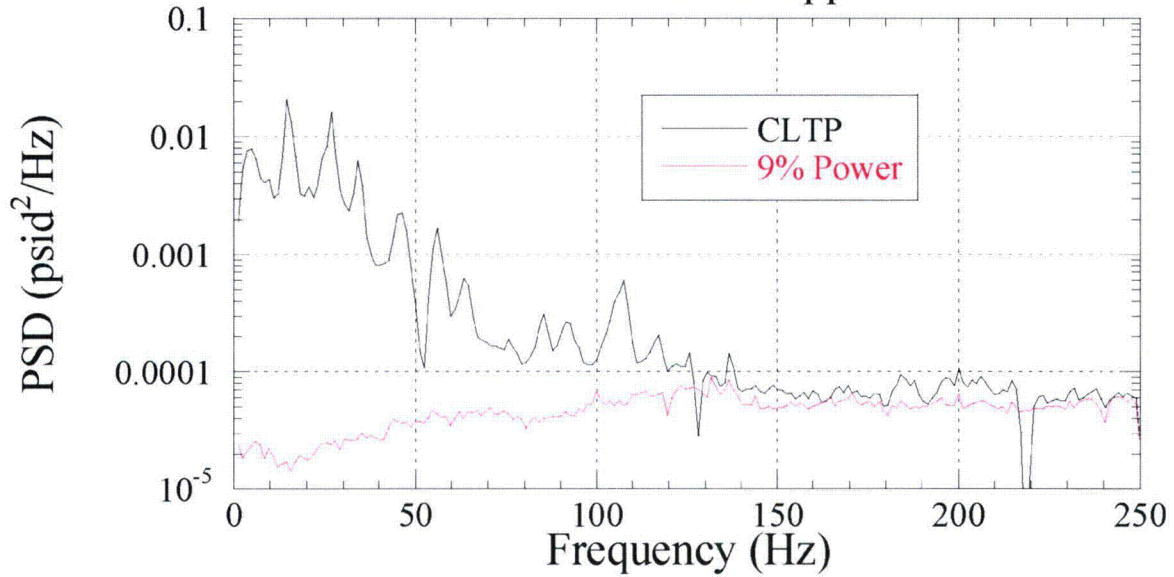


Figure EMCB.172-1: PSD comparison of pressure measurements on main steam line A at strain gage locations upper (top) and lower (bottom), for CLTP and 9% power conditions.

NON-PROPRIETARY INFORMATION

BFN1: MSL B Upper



BFN1: MSL B Lower

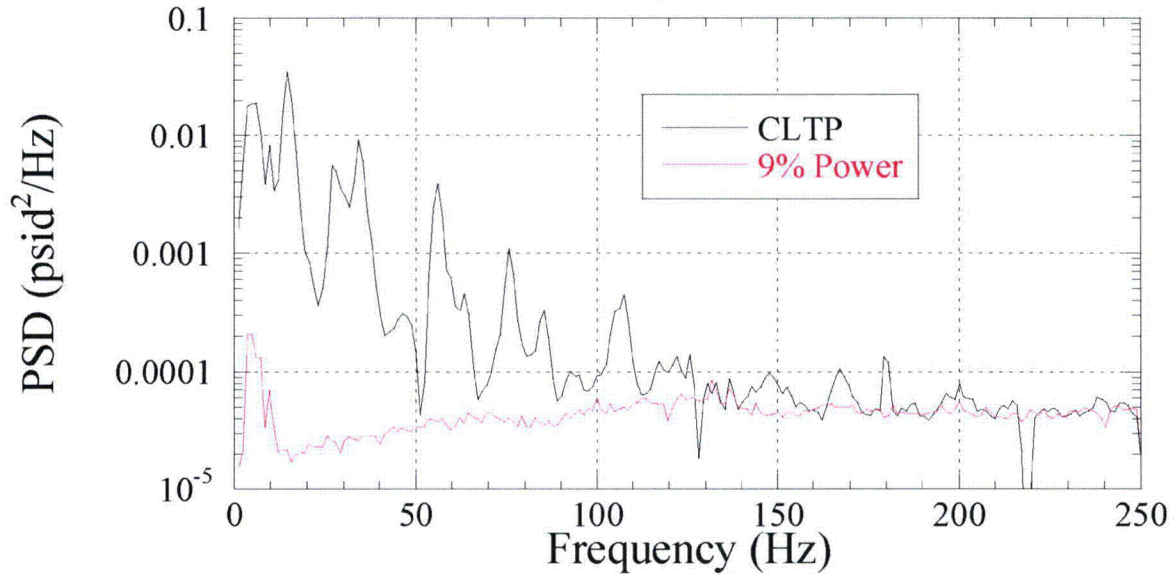
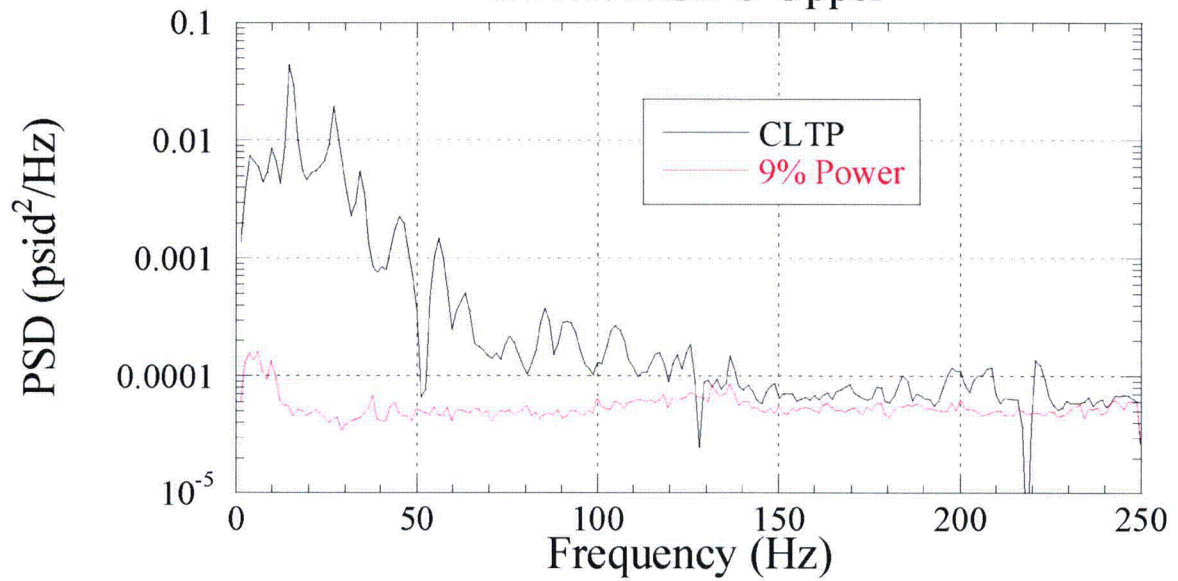


Figure EMCB.172-2: PSD comparison of pressure measurements on main steam line B at strain gage locations upper (top) and lower (bottom), for CLTP and 9% power conditions

NON-PROPRIETARY INFORMATION

BFN1: MSL C Upper



BFN1: MSL C Lower

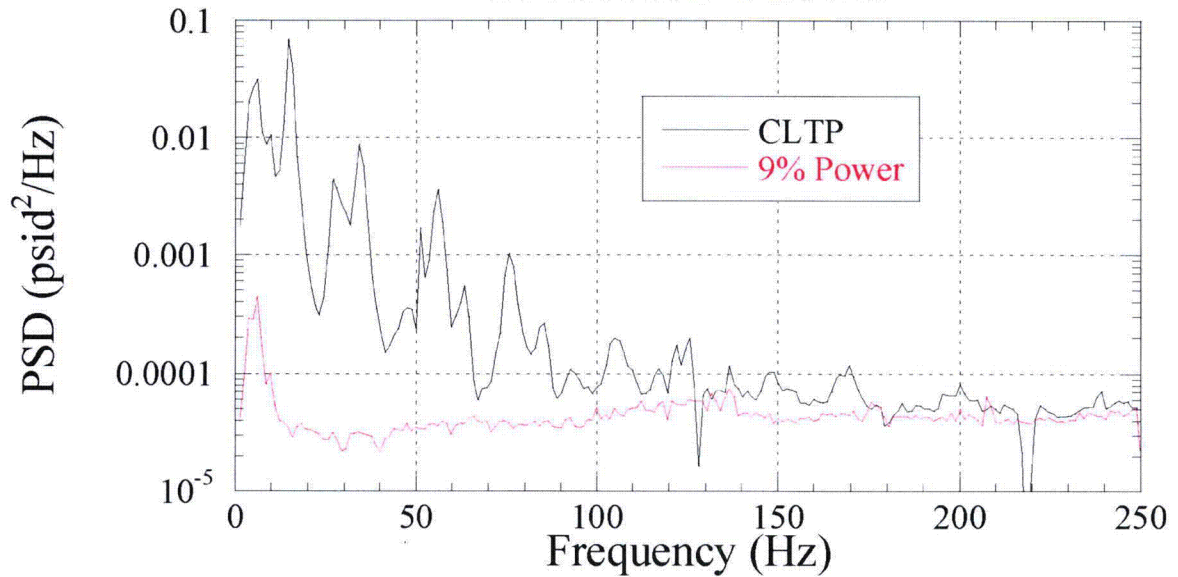
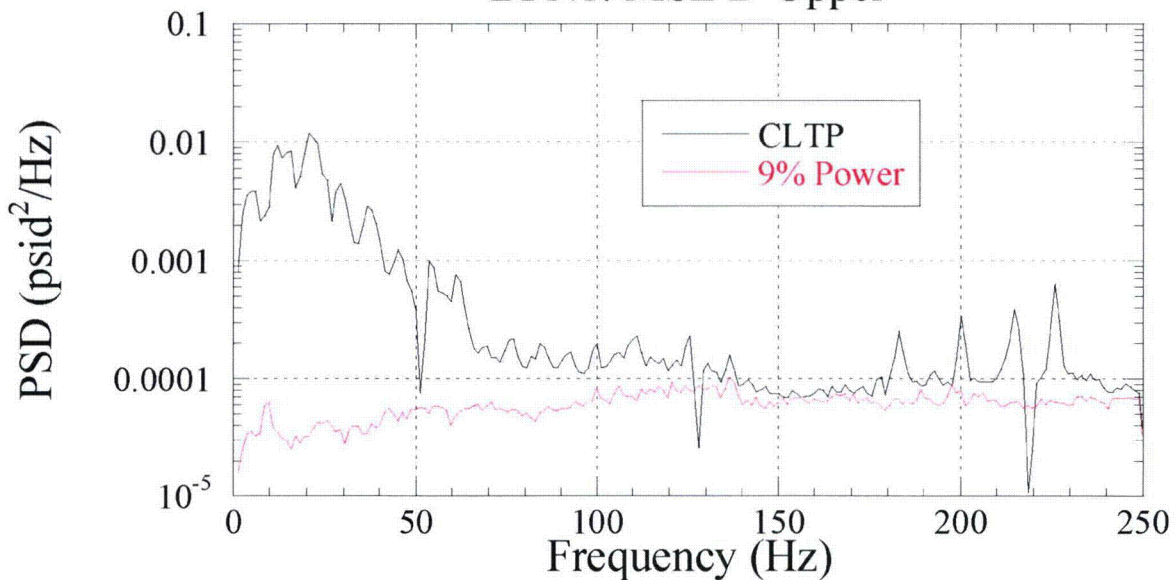


Figure EMCB.172-3: PSD comparison of pressure measurements on main steam line C at strain gage locations upper (top) and lower (bottom), for CLTP and 9% power conditions

NON-PROPRIETARY INFORMATION

BFN1: MSL D Upper



BFN1: MSL D Lower

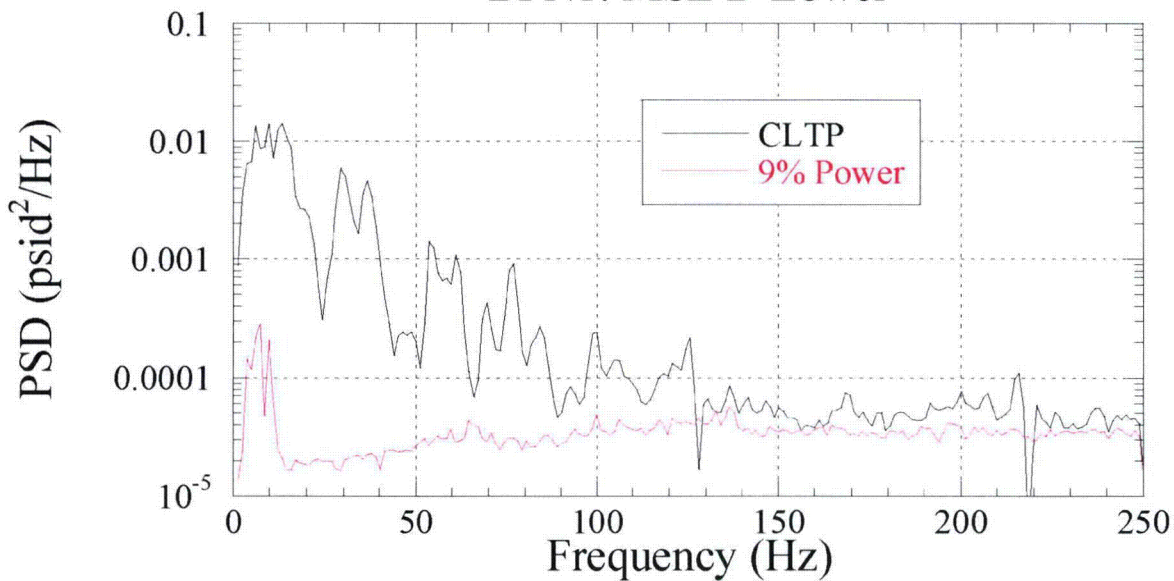


Figure EMCB.172-4: PSD comparison of pressure measurements on main steam line D at strain gage locations upper (top) and lower (bottom), for CLTP and 9% power conditions

NON-PROPRIETARY INFORMATION

- (ii) [[]] The noise removal scheme is the same as described in CDI Report No. 08-06P, Rev. 0, provided in the March 6, 2008 submittal, specifically the paragraph containing equations (8) and (9) on page 38. Equation (8) of that report is modified, however, to

$$P(f) = P_0(f) * \max \left[0.5, 1 - \frac{\overline{N}(f)}{P_0(f)} \right]$$

so that the signal cannot be reduced to less than 1/2 its original (i.e., with noise) amplitude. Previously, the noise removal scheme allowed the signal to be reduced to zero and this actually occurred during implementation particularly at higher frequencies where the noise was quite high. Limiting the amplitude reduction to 3dB or less (equivalent to a power reduction to 6dB or less) is judged both more reasonable and conservative than permitting zero pressure amplitude.

The noise removal algorithm limits the maximum reduction in the amplitude to 50% of the original signal. This value is considerably higher (i.e., more conservative) than what is considered common practice in spectral subtraction methods [References 1 - 4]. For example, values of $\beta=0.002$ [Reference 3] and $\beta=0.005$ to as high as 0.1 [Reference 4] are suggested as spectral floor values in the context of over-subtraction methods. Since these values pertain to power spectral subtraction, the equivalent values for the amplitude subtraction approach here would be $\sqrt{\beta}$ or values in the range 0.044 to 0.316. The value of 0.5 currently used is higher than this range and thus is more restrictive in the amount of amplitude reduction that is permitted (i.e., it is more conservative).

[[

NON-PROPRIETARY INFORMATION

NON-PROPRIETARY INFORMATION

NON-PROPRIETARY INFORMATION

]]

References

1. Saeed Vaseghi, *Advanced Digital Signal Processing and Noise Reduction*, 2nd Ed., John Wiley & Sons, Ltd., 2000.
2. Steven F. Boll, "Suppression of acoustic noise in speech using spectral subtraction," *IEEE Trans. on Acoustics, Speech and Signal Processing*, 27(2), April 1979.
3. Sunil D. Kamath and Philipos C. Loizou, "A multi-band spectral subtraction method for enhancing speech corrupted by colored noise," *IEEE International Conference on Acoustics, Speech and Signal Processing – Proceedings*, Vol. 4, pp. IV/4164, 2002
4. M. Berouti, R. Schwartz, J. Makhoul, Enhancement of speech corrupted by acoustic noise, *Proceedings of the IEEE ICASSP'79, Washington, 1979*, pp. 208-211.

Table EMCB.172-1: Mean Pressure Fourier Coefficient Amplitude (psi)

MSL	Power Level				
	0%	9%	19%	Min. Pow.	100%
A-Lower	39.70	35.96	34.02	32.15	104.33
B-Upper	40.59	37.45	36.04	34.55	105.34
B-Lower	42.15	39.03	37.60	34.54	105.05
C-Upper	43.92	41.56	40.90	38.02	111.62
C-Lower	42.50	40.38	39.99	38.10	113.40
D-Upper	44.14	40.86	39.46	37.62	115.04
D-Lower	40.81	38.46	36.94	35.63	50.24

Note: MSL A Upper was not detrended and thus contains a bias that increases with frequency. Therefore, results for this station were not considered in this response.

NON-PROPRIETARY INFORMATION

Table EMCB.172-2a: Reductions in monopole amplitude peaks due to noise filtering

MSL	Frequency [Hz]	PSD [psi^2/Hz] $\times 10^4$	Frequency [Hz]	PSD [psi^2/Hz] $\times 10^4$	% Amplitude Change
A	37.64	2.141	37.64	2.065	-1.78
"	44.96	2.362	44.96	2.201	-3.48
"	48.30	0.889	48.26	0.674	-12.93
"	61.61	3.324	61.62	2.414	-14.79
"	63.90	1.568	63.87	0.976	-21.12
B	34.58	3.109	34.57	2.892	-3.56
"	45.84	1.819	45.84	1.428	-11.40
"	56.22	1.922	56.23	1.255	-19.18
"	63.95	2.699	63.94	1.763	-19.17
C	34.36	2.521	34.36	2.198	-6.62
"	45.46	1.506	45.46	1.131	-13.34
"	57.69	1.176	57.62	0.621	-27.36
"	63.91	2.294	63.90	1.302	-24.66
D	61.80	2.040	61.78	1.277	-20.88

NON-PROPRIETARY INFORMATION

Table EMCB.172-2b: Reductions in dipole amplitude peaks due to noise filtering

MSL	Frequency [Hz]	PSD [psi ² /Hz]x10 ⁴	Frequency [Hz]	PSD [psi ² /Hz]x10 ⁴	% Amplitude Change
A	31.79	0.635	32.65	0.469	-14.01
"	44.93	0.591	44.94	0.561	-2.64
"	48.28	0.180	48.22	0.139	-12.26
"	56.28	0.243	56.27	0.178	-14.52
"	58.80	0.276	58.80	0.198	-15.33
B	32.24	0.627	32.26	0.488	-11.76
"	34.60	2.332	34.60	2.109	-4.90
"	45.81	0.436	45.81	0.357	-9.54
"	48.93	0.127	48.92	0.085	-18.31
"	56.25	0.777	56.25	0.600	-12.12
"	60.22	0.002	60.20	0.001	-27.02
C	34.42	1.397	34.42	1.126	-10.22
"	45.43	0.290	45.43	0.224	-12.20
"	48.59	0.074	48.56	0.044	-22.62
"	55.96	0.365	55.96	0.260	-15.51
"	58.84	0.140	58.77	0.077	-25.92
D	33.48	0.229	33.46	0.188	-9.41
"	35.99	0.602	36.01	0.515	-7.44
"	45.13	0.162	45.14	0.120	-13.99
"	48.43	0.071	48.41	0.041	-23.91
"	56.83	0.152	56.83	0.080	-27.19
"	59.23	0.162	59.22	0.092	-24.42

NON-PROPRIETARY INFORMATION

[[

]]

NON-PROPRIETARY INFORMATION

[[

]]

NON-PROPRIETARY INFORMATION

[[

]]

NON-PROPRIETARY INFORMATION

[[

]]

NON-PROPRIETARY INFORMATION

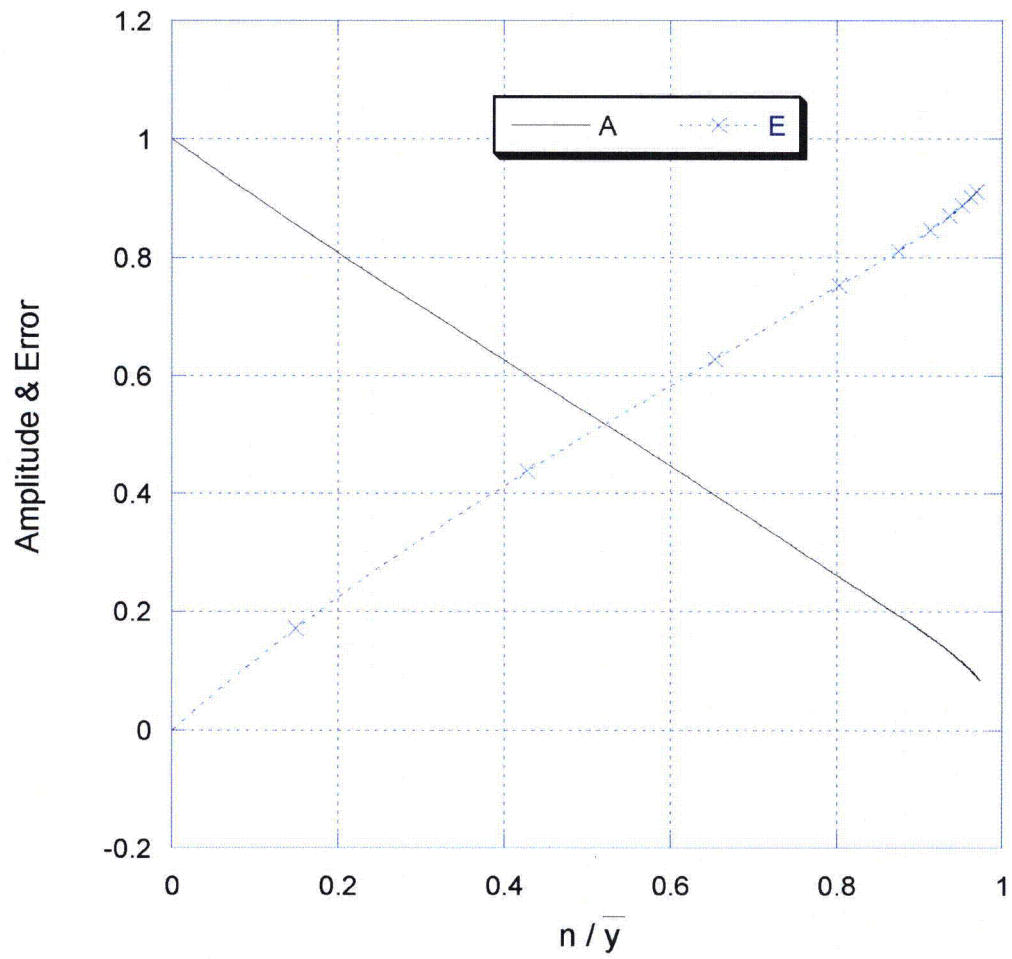


Figure EMCB.172-6: Variation of amplitude, A, and error, E, with n/\bar{y}

NON-PROPRIETARY INFORMATION

[[

Figure EMBC-7a: Comparison of measured and quadratic-fitted pressure amplitudes as a function of power on MSL A-lower at 61.502 Hz]]

NON-PROPRIETARY INFORMATION

[[

Figure EMCB.172-7b: Comparison of measured and quadratic-fitted pressure amplitudes as a function of power on MSL B at low frequency peak 12.732 Hz and at 107 Hz]]

NON-PROPRIETARY INFORMATION

[[

Figure EMCB.172-7c: Comparison of measured and quadratic-fitted pressure amplitudes
as a function of power on MSL C at mid-frequency peak 167.40 Hz and at 34.351 Hz]]

NON-PROPRIETARY INFORMATION

[[

Figure EMCB.172-7d: Comparison of measured and quadratic-fitted pressure amplitudes
as a function of power on MSL D at 46.549 Hz and at high-frequency peak 226.10 Hz]]

NON-PROPRIETARY INFORMATION

[[

]]

Figure EMCB.172-8a: Variation of pressure amplitude and quadratic fit error with frequency for MSL A

NON-PROPRIETARY INFORMATION

[[

Figure EMCB.172-8b: Variation of pressure amplitude and quadratic fit error with frequency for MSL B

]]

NON-PROPRIETARY INFORMATION

[[

Figure EMCB.172-8c: Variation of pressure amplitude and quadratic fit error with
frequency for MSL C

]]

NON-PROPRIETARY INFORMATION

[[

Figure EMCB.172-8d: Variation of pressure amplitude and quadratic fit error with frequency for MSL D

]]

NON-PROPRIETARY INFORMATION

[[

Figure EMCB.172-9a: Variation of quadratic-fit pressures with frequency for MSL A
Lower at 0 to 120 Hz

]]

NON-PROPRIETARY INFORMATION

[[

Figure EMCB.172-9b: Variation of quadratic-fit pressures with frequency for MSL A
Lower at 120 to 250 Hz

]]

NON-PROPRIETARY INFORMATION

[[

]]

NON-PROPRIETARY INFORMATION

- (b) The responses to RAIs EMCB.138/105 in the March 6, 2008 submittal and EMCB.170/138 in this submittal compare the accumulative PSDs of selected nodes (those with low alternating stress ratios) at zero frequency shift and the frequency shifts that yielded the lowest alternating stress ratios. These results showed that the stresses are dominated by frequency peaks about 34, 47 and 62 Hz. Further investigation examining the pressure signal PSDs in the response to part (a)(ii) above, shows that the effect of noise filtering is strongest for the 62 Hz signal where the average reduction in the signal amplitude is 21% for the monopoles and 20.3% for the dipoles, and weakest at the 34 Hz frequency with noise reductions of 3.99% for the monopoles and 9.6% for the dipoles. Because the signal amplitudes are reduced by the noise filtering, one expects that the resulting stress amplitudes will also be reduced. Because the system is linear, reducing all the MSL signals at a given frequency by some fraction will lower the corresponding stress harmonics by the same amount. More generally, since each MSL signal is reduced by different amounts (see Table EMCB.172-2) the change in stress is more complicated. Furthermore, since the stress intensity is related nonlinearly to the stress harmonics, it follows that changes in pressure signal amplitudes can produce changes in stress intensities that differ in both magnitude and occasionally sign (i.e., stress intensity increase or reduction). These issues are discussed further in the responses to RAIs EMCB.138/105 and EMCB.170/138.

In order to quantify the frequency-dependent effect of noise reduction on computed stresses, the accumulative PSDs with and without noise reduction are compared for the same ten nodes in Figures EMCB.172-11a through 11e. As indicated in part (a)(ii) above, the current noise filtering algorithm prevents reductions in signal amplitude greater than 50%. Nevertheless, comparisons of the accumulative PSDs obtained using the current filtering algorithm and the older one that permitted up to 100% reductions in amplitude (i.e., allowed the filtered signals to have zero amplitude) show very little difference. The comparisons of the accumulative PSDs obtained with and without noise filtering corroborate the general conclusions made in the preceding section (a)(ii) namely that: (1) there is relatively small change in stress (less than 10% change) at the 34 Hz level based on the curves for nodes 88059, 107054, 96561 and 103094; (2) a moderate (approximately 15%) reduction at 47 Hz based on the plots for nodes 102407, 103088, 102521 and 103089; and (3) an additional separating of the curves at 62 Hz and higher. The final values of the accumulative PSDs at 250 Hz directly correspond to the RMS values of the stress histories. These RMS stress values are tabulated below in Table 172-3. The average reduction in RMS stress resulting from the noise reduction algorithm is 16.9%.

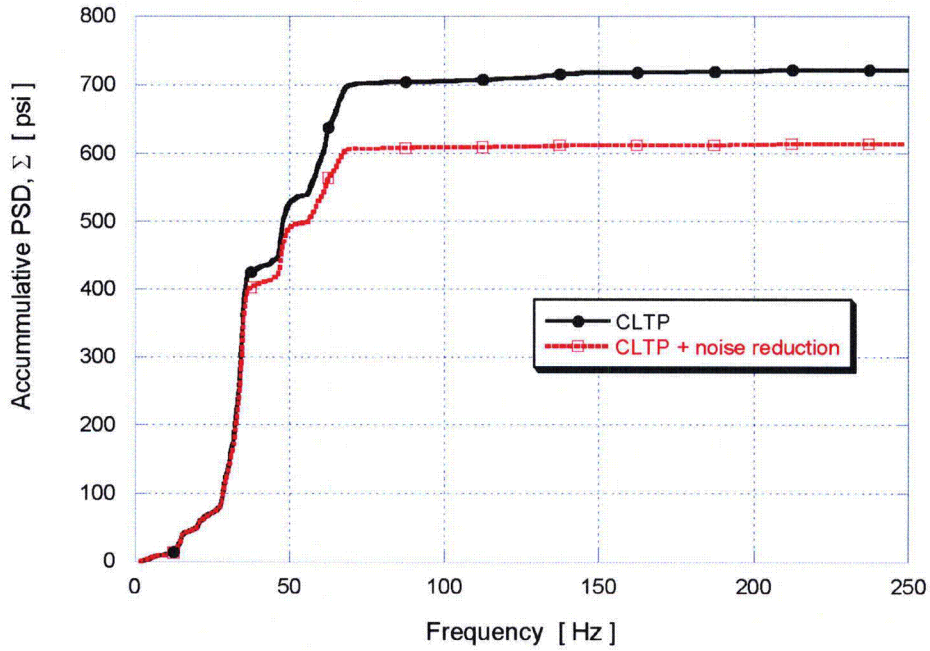
NON-PROPRIETARY INFORMATION

Table EMCB.172-3: Reductions in RMS component stresses resulting from noise filtering

Location	Node	Stress component	Stress RMS (psi)		Reduction (%)
			original signal	with noise reduction	
1. Top Cover Inner Hood/Top Cover Overlap/Top Perf. Plate	88059	σ_{xx}	722.3	613.8	15.0
2. Top Cover/Tie Bar Base	107054	σ_{xx}	761.7	646.6	15.1
3. Top Cover/Tie Bar Base	102407	σ_{xx}	671.3	521.9	22.3
4. Top Cover Middle Hood/Top Perf. Plate/Top Cover Overlap	91420	σ_{xx}	862.1	679.4	21.2
5. Top Cover/Tie Bar Base	96561	σ_{xx}	623.8	522.7	16.2
6. Top Perf/Top Cover/Dam Plate	103088	σ_{xx}	575.3	496.8	13.6
7. Submerged Drain Channel/Skirt	104539	σ_{yy}	657.4	499.1	24.1
8. Dam Plate/Lock	102521	σ_{yy}	505.7	434.8	14.0
9. Top Cover Inner Hood/Hood Support/Tie Bar Base	103094	σ_{xy}	266.6	227.5	14.7
10. Top Perf/Top Cover/Dam Plate	103089	σ_{xx}	552.8	483.1	12.6

NON-PROPRIETARY INFORMATION

Node 88059, σ_{xx} (+5% shift)



Node 107054, σ_{xx} (+10% shift)

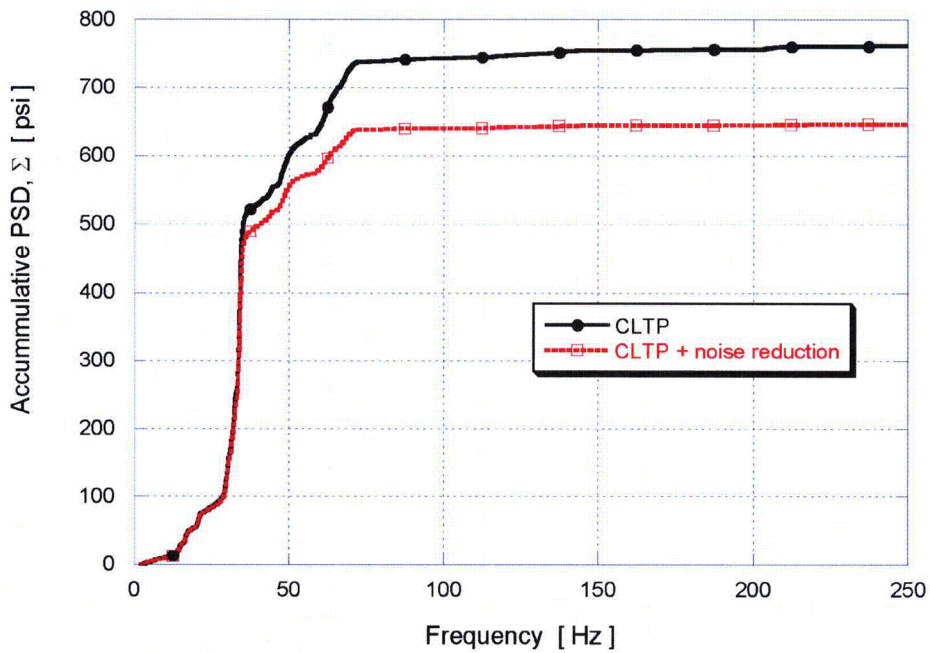
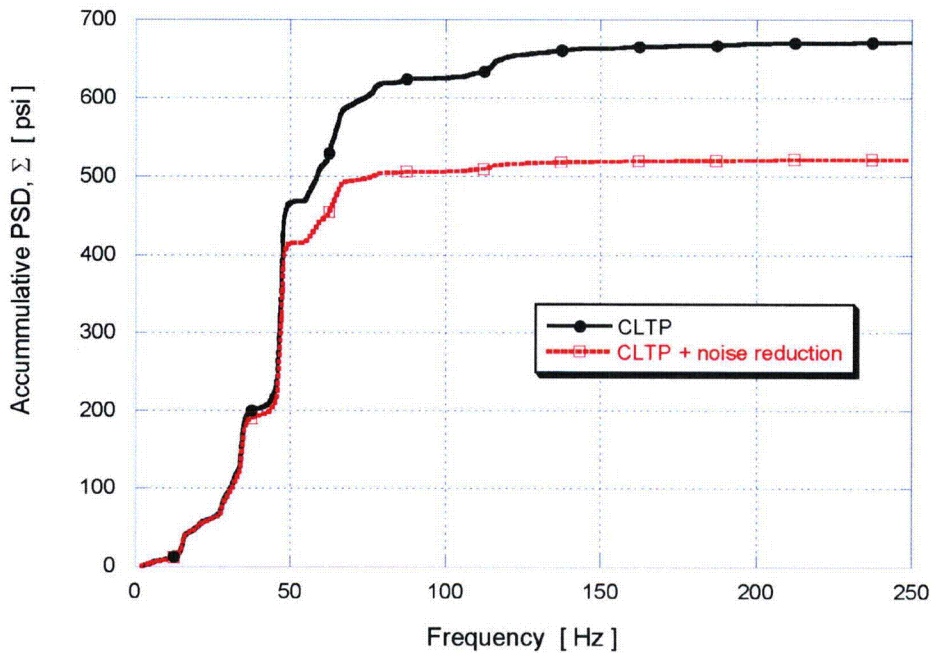


Figure EMCB.172-11a: Accumulative PSD curves for nodes 88,059 and 107,054 with and without noise reduction

NON-PROPRIETARY INFORMATION

Node 102407, σ_{xx} (+2.5% shift)



Node 91420, σ_{xx} (+10% shift)

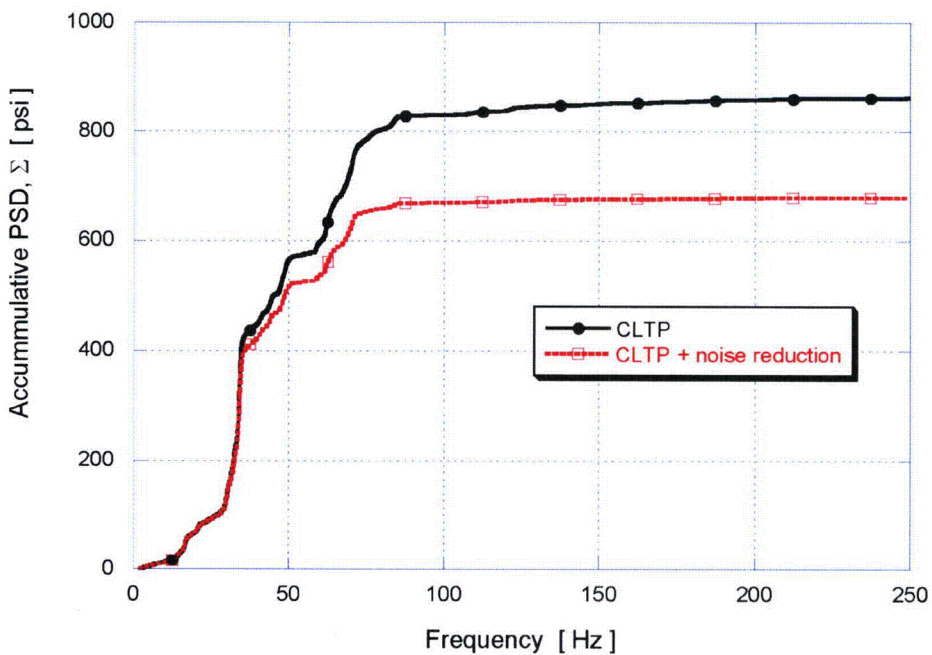
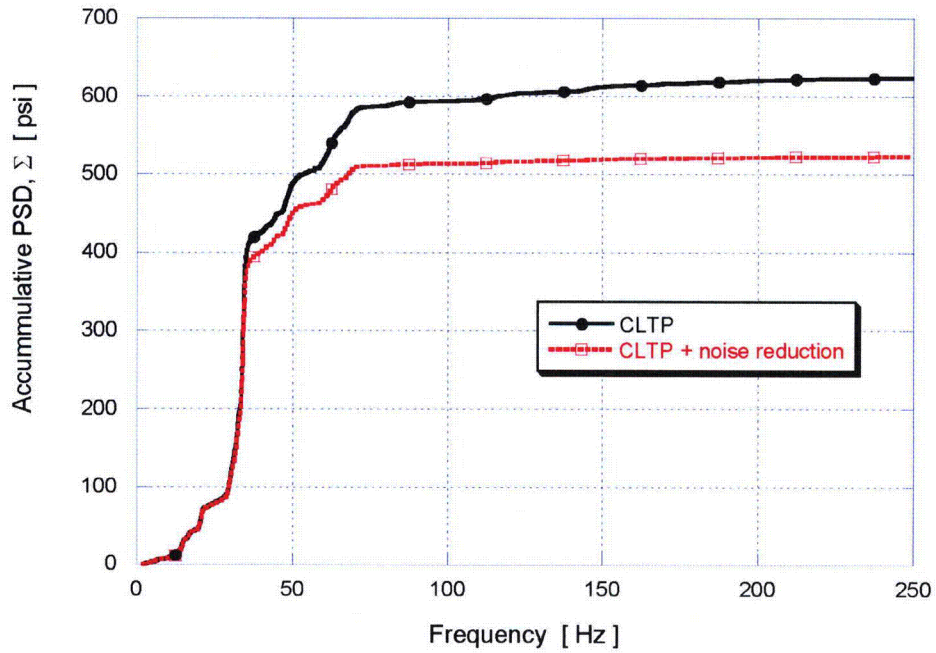


Figure EMCB.172-11b: Accumulative PSD curves for nodes 102,407 and 91,420 with and without noise reduction

NON-PROPRIETARY INFORMATION

Node 96561, σ_{xx} (+10% shift)



Node 103088, σ_{xx} (+7.5% shift)

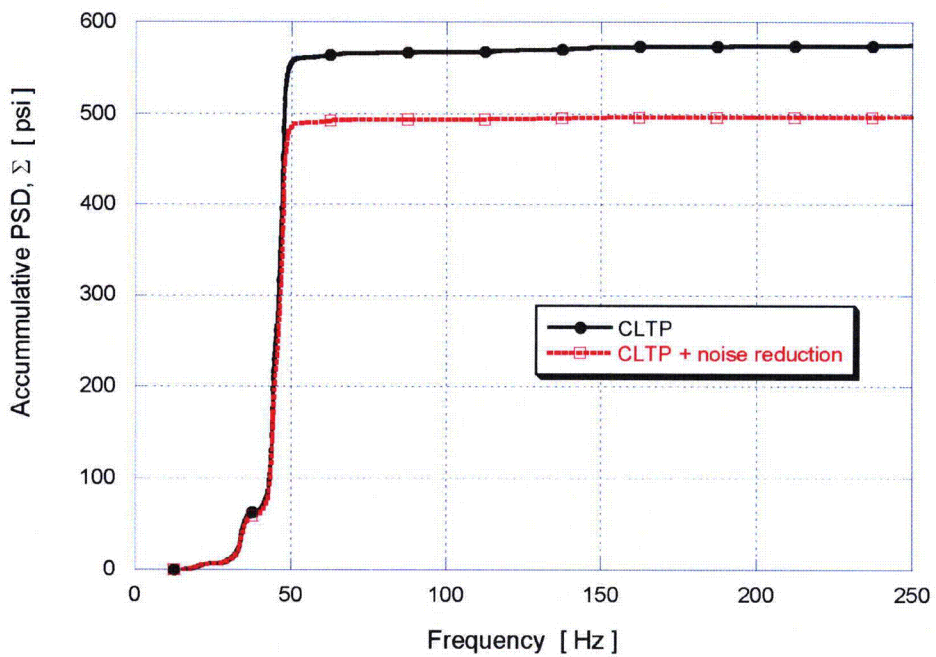
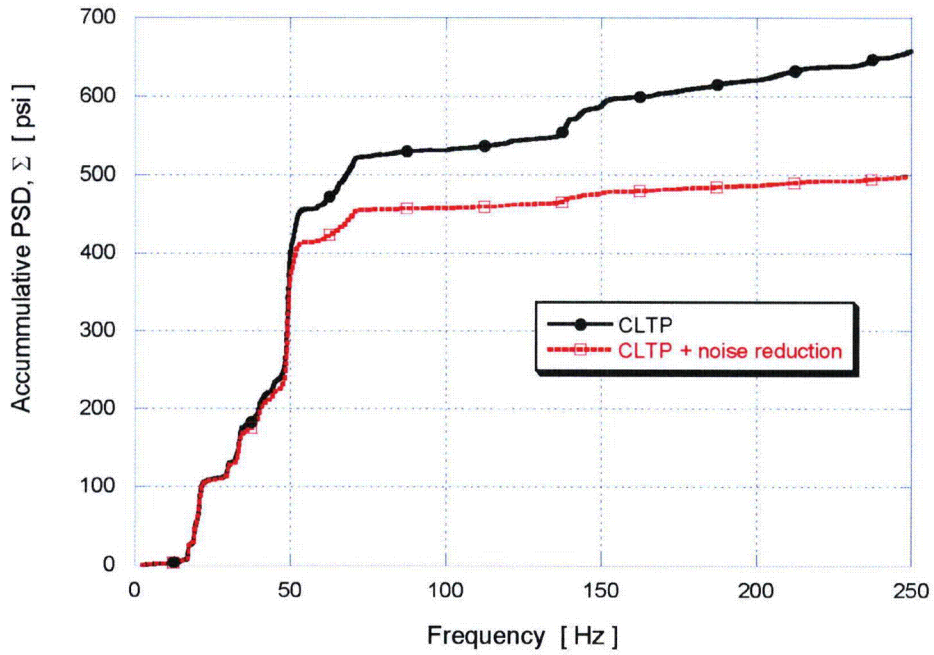


Figure EMCB.172-11c: Accumulative PSD curves for nodes 96,561 and 103,088 with and without noise reduction

NON-PROPRIETARY INFORMATION

Node 104539, σ_{yy} (+10% shift)



Node 102521, σ_{yy} (+7.5% shift)

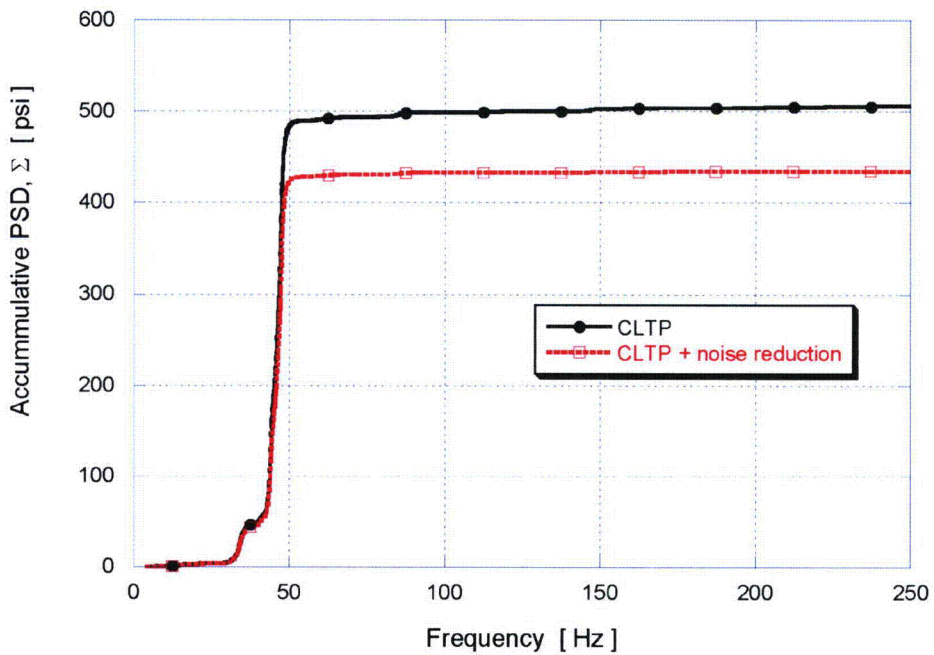
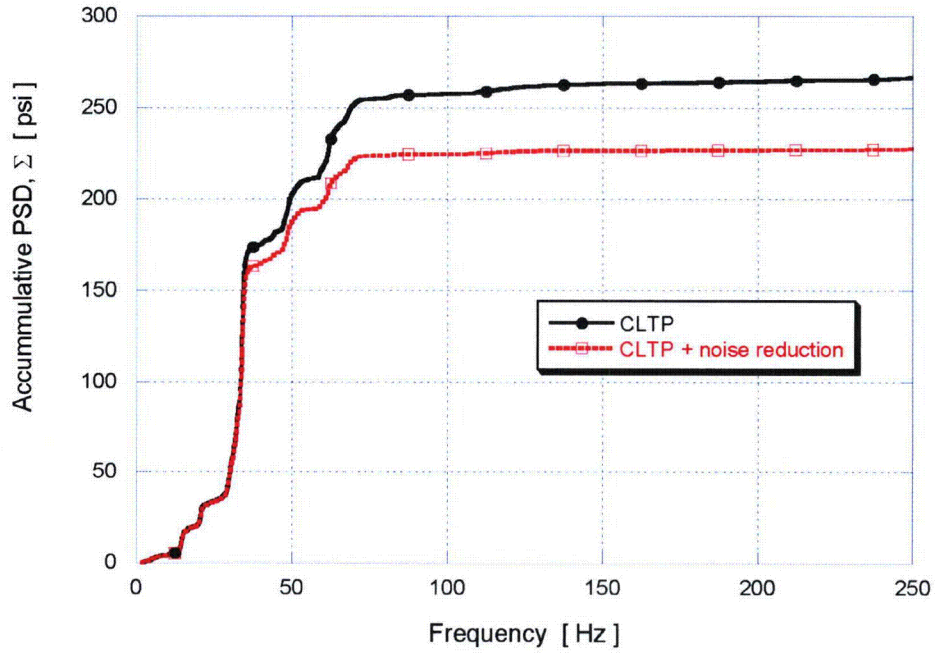


Figure EMCB.172-11d: Accumulative PSD curves for nodes 104,539 and 102,521 with and without noise reduction

NON-PROPRIETARY INFORMATION

Node 103094, σ_{xy} (+10% shift)



Node 103089, σ_{xx} (+5% shift)

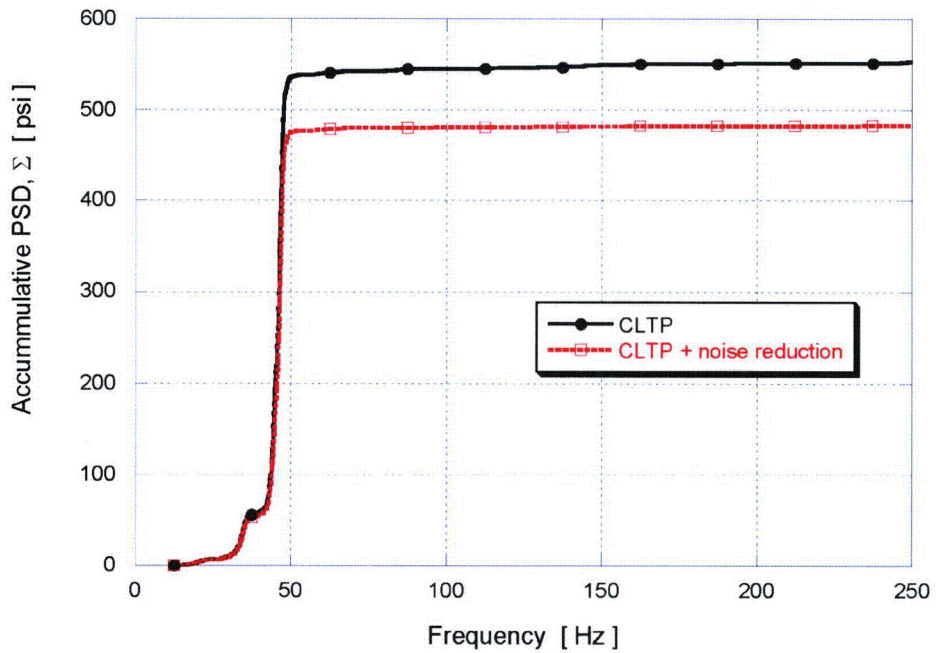


Figure EMCB.172-11e: Accumulative PSD curves for nodes 103,094 and 103,089 with and without noise reduction

NON-PROPRIETARY INFORMATION

- (c) Industry steam dryer stress analyses to support EPU's have traditionally been performed using shell and beam finite element models. This general approach has been applied for modeling replacement tie bars and their attachment to the steam dryers. Specifically, the tie bars are modeled as beam elements and the tie bar attachment pad is modeled as a shell element, which is in turn attached to either hood or vane bank covers, which are also modeled using shell elements. In this technique, the weld joints connecting the tie bar to the pad and the pad to the cover plates are modeled simply as common nodes. This modeling approach introduces a conservatively severe discontinuity between connected parts of differing thickness because it ignores the 3-dimensional strain distribution provided by the fillet weld. Although this simplification does not significantly affect the overall structural dynamic behavior of the steam dryer, it reduces the number of nodes in a model to a manageable level. Figure EMCB.170/138-1 shows an example of shell and beam modeling for the tie bar attachments compared to a more detailed solid model representation given in Figure EMCB.168/136-1. Experience with solid element modeling of this tie bar attachment design yielded reduced stresses at the weld relative to shell and beam modeling. It should be noted that the tie bars are being re-designed as detailed in the response to RAI EMCB.180 in this submittal to increase stress margin and, therefore, the above tie bar configuration will not be used.
- (d) Most of the bending is removed in the strain gage signals. In pure bending, assuming the neutral axis is through the center of a beam cross section, half of the cross section above the neutral axis will experience axial tension and the other half will be under compression. When the strain gages are directed to measure the hoop strain (circumferential), bending will introduce errors due to the Poisson effect. However, if two strain gages are located diametrically opposite to each other, the composite signal will cancel out the bending contribution. Since the plane of bending is not known a priori, a number of such strain sensor pairs will minimize the bending contribution in all possible planes but not totally eliminate the bending.

NRC RAI EMCB.173/140

It was indicated that TVA plans to deviate from the FE modeling uncertainty used by PSEG for the Hope Creek dryer (25.26 percent), claiming that uncertainty in the loss factors inferred from the hammer tests reduces the FE modeling uncertainty to 21.5 percent. However, the uncertainty used in the Unit 1 limit curves (shown in Table 3 of CDI Technical Note 07-30P, Rev. 1) is 25.26 percent. Clarify the FE model uncertainty used in all BFN analyses, and provide more detail on how a 37 percent uncertainty in hammer test damping reduces FE modeling uncertainty from 25.26 percent to 21.5 percent.

TVA Response to EMCB.173/140

In the response to RAI EMCB.143/110 in the January 31, 2008 submittal, TVA indicated that 21.5 percent value would be used for subsequent BFN analyses. However, in order to facilitate the review and approval of the BFN EPU license amendment, TVA decided to use the same value that was used in the Hope Creek analyses (25.26 percent).

The use of the 25.26 percent 'Shaker Test' uncertainty is reflected in Table 5.2 of CDI Report No. 08-04P (Enclosure 3 of the March 6, 2008, submittal) for Unit 1 and CDI Report No. 08-05P (Enclosure 3 of the April 4, 2008, submittal) for Unit 2. This value is also being used for the Unit 3 steam dryer analyses and will be reflected in the associated Unit 3 load report.

NON-PROPRIETARY INFORMATION

NRC RAI EMCB.174/141

In the response to EMCB 153/120, TVA uses another set of Quad Cities Unit 2 (QC2) data to validate the Acoustic Circuit Model (ACM) Rev. 4. According to the response to EMCB 154/121(a), the dipole source terms calculated from ACM Rev. 4 are stronger in BFN than in QC2. Provide a validation of the ACM Rev. 4 against additional dryer data where the low frequency loading on the dryer is more pronounced (i.e., higher than that of BFN).

TVA Response to EMCB.174/141

As previously stated in the response to RAI EMCB.153/120 in the January 31, 2008, submittal, no additional data sets are available to TVA to undertake further validation of ACM Rev. 4.

NRC RAI EMCB.175/142

[[

]]

[[

]]

TVA Response to EMCB.175/142

[[

NON-PROPRIETARY INFORMATION

NON-PROPRIETARY INFORMATION

NON-PROPRIETARY INFORMATION

NON-PROPRIETARY INFORMATION

NRC RAI EMCB.176/143

[[

]]

TVA Response to EMCB.176/143

[[

]]

NON-PROPRIETARY INFORMATION

NON-PROPRIETARY INFORMATION

NON-PROPRIETARY INFORMATION

]]

NON-PROPRIETARY INFORMATION

NRC RAI EMCB.177/144

[[

]]

(a) Explain where this pressure is measured;

(b) [[

]]

(c) [[

]]

TVA Response to EMCB.177/144

[[

NON-PROPRIETARY INFORMATION

NON-PROPRIETARY INFORMATION

NON-PROPRIETARY INFORMATION

NON-PROPRIETARY INFORMATION

NON-PROPRIETARY INFORMATION

]]

NRC RAI EMCB.178/145

The [[]] bias error associated with FE model displacement convergence should not be subsumed by the FE model uncertainty determined from the hammer test data. As the overall FE mesh convergence bias error reported in Table 3 of CDI Technical Note 07-30P, Rev. 1, appears to be [[]]. Address why [[]] percent is appropriate.

TVA Response to EMCB.178/145

TVA will include the [[]] bias error associated with FE model displacement convergence in the revised BFN steam dryer stress analyses.

NRC RAI EMCB.179/146

Provide plots to support the information submitted in the response to EMCB 166/133. Limit curves for all plants discussed should be plotted on the same graphs so that they may be easily compared.

TVA Response to EMCB.179/146

PSD comparison of pressure measurements on the MSLs for Quad Cities Unit 2 at original licensed thermal power (QC), Hope Creek at CLTP (HC), Susquehanna at CLTP (SQ), and BFN Unit 2 at CLTP (BF) are provided in Figures EMCB.179/146-1 through 8.

NON-PROPRIETARY INFORMATION

[[

]]

Figure EMCB.179/146-1: PSD comparison of pressure measurements on MSL A Upper

[[

]]

Figure EMCB.179/146-2: PSD comparison of pressure measurements on MSL A Lower

NON-PROPRIETARY INFORMATION

[[

]]

Figure EMCB.179/146-3: PSD comparison of pressure measurements on MSL B Upper

[[

]]

Figure EMCB.179/146-4: PSD comparison of pressure measurements on MSL B Lower

NON-PROPRIETARY INFORMATION

[[

]]

Figure EMCB.179/146-5: PSD comparison of pressure measurements on MSL C Upper

[[

]]

Figure EMCB.179/146-6: PSD comparison of pressure measurements on MSL C Lower

NON-PROPRIETARY INFORMATION

[[

]]

Figure EMCB.179/146-7: PSD comparison of pressure measurements on MSL D Upper

[[

]]

Figure EMCB.179/146-8: PSD comparison of pressure measurements on MSL D Lower

NON-PROPRIETARY INFORMATION

NRC RAI EMCB.180 (Unit 1 only)

CDI Report 08-06P, *Stress Assessment of Browns Ferry Nuclear Unit 1 Steam Dryer*, Revision 0, states that the minimum alternating stress ratio (SR-a) for the Unit 1 dryer is 1.56. This ratio takes into account the hydrodynamic damping due to perforated plates and the end-to-end uncertainties excluding the [[]] percent bias error associated with the convergence of the finite element displacement results.

The inclusion of the [[]] percent bias error reduces the minimum alternating stress ratio for Unit 1 steam dryer from [[]] This stress ratio will be further reduced to [[]] at the extended power uprate (115 percent of CLTP) provided no acoustic resonance appears during power ascension; otherwise it will be reduced further.

Given the response relies on the following: (a) [[]] (b) use of an ACM that may not include the sources that might be present in the reactor pressure vessel, and (c) [[]]

TVA Response to EMCB.180

Through meetings and discussions with the NRC, TVA understands that the minimum alternating stress margin (SR-a) expectation for the steam dryers is 2.0 at EPU conditions. For BFN, this equates to a minimum SR-a of 2.7 for analyses performed at CLTP conditions. As summarized below, TVA is performing several actions to increase the minimum alternating stress ratios (SR-a) for the BFN steam dryers. These actions were preliminarily discussed with the NRC staff during the April 17, 2008 meeting. The discussion below addresses the specific actions that are being taken on Unit 1; similar, but slightly different, modifications have been identified for Units 2 and 3.

By the March 6, 2008 submittal, TVA submitted the steam dryer stress analysis for Unit 1 which reported a minimum SR-a of 1.56. As discussed at the April 17, 2008 meeting, TVA examined the stress analysis to determine which steam dryer components exhibited a SR-a less than the 2.7 margin expected for CLTP. Fourteen nodes were identified and are listed in Table EMCB.170/138-1 of this submittal. (Ten nodes have been identified on Unit 2.) These fourteen nodes have been divided into four "families" of locations/components for further discussion:

- Tie bar
- Steam dam
- Drain channel
- Hood

These families were examined to determine appropriate courses of action to resolve the high stresses at these locations. For the tie bars and steam dam families, modifications will be performed to reduce the stresses associated with these locations. The tie bars currently installed on the Unit 1 steam dryer (see the response to RAI EMCB.168/136 in this submittal) will be replaced with tie bars constructed with 1 inch x 2 inch solid stock with modified attachment to the dryer banks. A typical drawing of the new tie bar design is provided in Figure EMCB.180-1. Additional support gussets will be added to the steam dams as shown in Figure EMCB.180-2. These changes have been incorporated into the finite element model (FEM) for

NON-PROPRIETARY INFORMATION

the steam dryer stress analysis. (The design of the tie bars and steam dam gussets for Unit 2 has been modified from the Unit 1 design to address Unit 2 specific loads. Additionally, reinforcement of the outer hood top cover will be made for Unit 2.)

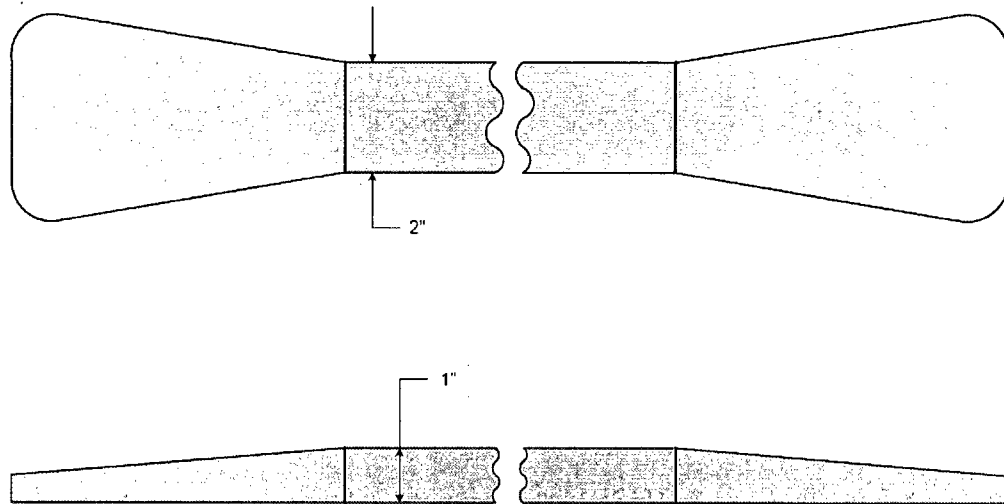


Figure EMCB.180-1: New tie bar design

NON-PROPRIETARY INFORMATION

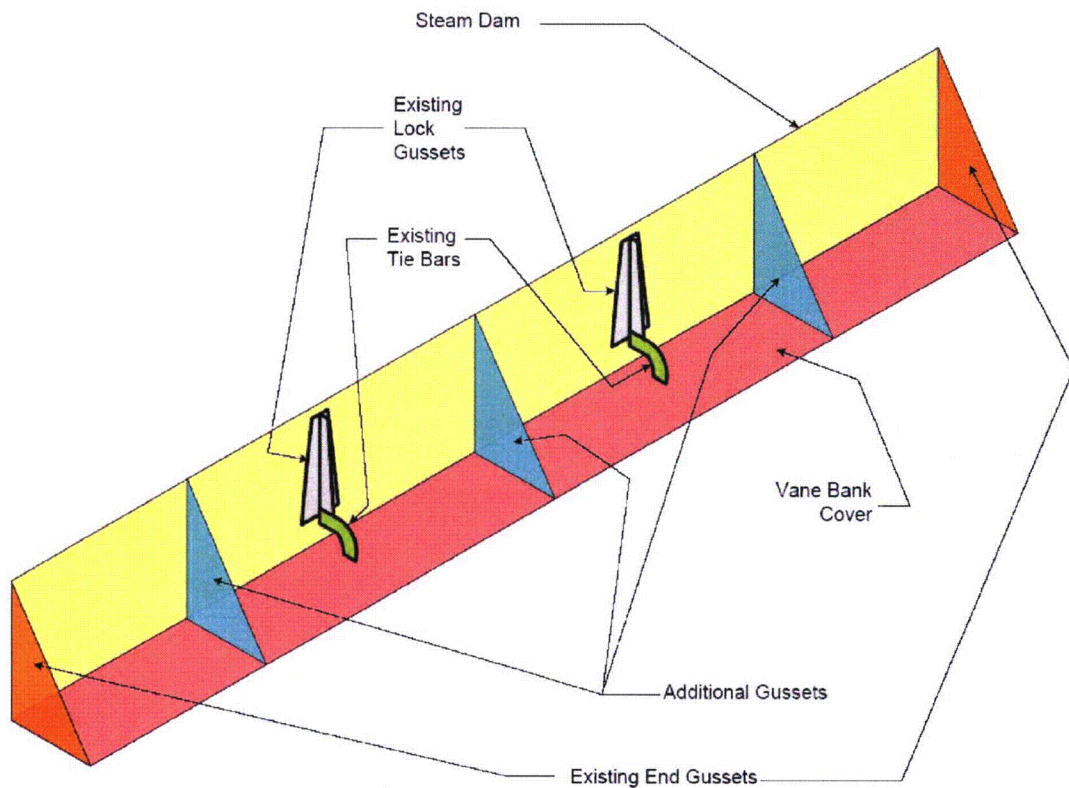


Figure EMCB.180-2: Steam dam gusset modification

For the drain channel and hood families, additional substructure analyses were performed on the affected locations. These analyses are provided in Enclosure 6, Calculation Package 0006982.01, "Shell and Solid Sub-Model Finite Element Stress Comparison." Based on past experience, it has been established that if the connections are modeled using solid elements to represent the weld, the weld can better distribute the stresses in the region of high stress concentration. Coupled with the use of stress linearization approach, the maximum stress intensity computed using the solid model (with the weld modeled) generally eliminates the overprediction of high stresses generally associated with shell elements in regions of high stress concentration. In this approach, the 1.8 weld factor will still be applied. Inspections of the drain channel at the high stress locations will be performed to verify the weld geometry.

The results of these actions have been incorporated into revised stress analyses for the BFN Units 1 and 2 steam dryers. The revised stress analyses include the following changes.

- Incorporated the planned modifications of the tie bars and steam dams (and reinforced outer hood top cover for Unit 2 only) into the finite element model.
- Incorporated the results of the substructure analyses into the steam dryer stress results.
- Added the 3.81 percent bias error discussed in the response to RAI EMCB.178/145 in this submittal.

NON-PROPRIETARY INFORMATION

- Revised the hydrodynamic damping value by 50% as discussed in the response to RAI EMCB.175/142 in this submittal.
- Modified the noise removal technique to limit the amplitude reduction to 3dB as discussed in the response to RAI EMCB.172 in this submittal.
- Utilized a different Unit 1 CLTP MSL strain gage data set in calculating the load on the Unit 1 steam dryer. This change was made to eliminate an anomaly present in the previous data set which was only apparent by a singularity in the stress time histories for the limiting nodes in the Unit 1 steam dryer. The revised Unit 1 load was calculated using a MSL strain gage data set taken during the same timeframe (~ 2 hours) and operating conditions.

The revised steam dryer load reports and stress analyses are provided in Enclosure 2, CDI Report No. 08-15P, "Stress Assessment of Browns Ferry Nuclear Unit 1 Steam Dryer with Tie-Bar Modifications," Enclosure 3, CDI Report No. 08-04P, "Acoustic and Low Frequency Hydrodynamic Loads at CLTP Power Level on Browns Ferry Nuclear Unit 1 Steam Dryer to 250 Hz," Enclosure 4, CDI Report No. 08-16P, "Stress Assessment of Browns Ferry Nuclear Unit 2 Steam Dryer with Tie-Bar Modifications," and Enclosure 5, CDI Report No. 08-05P, "Acoustic and Low Frequency Hydrodynamic Loads at CLTP Power Level on Browns Ferry Nuclear Unit 2 Steam Dryer to 250 Hz." New results based on the above changes indicate a minimum alternating stress ratio with frequency shifts of SR-a = 2.91 for Unit 1 and SR-a = 2.81 for Unit 2.